Theses and Dissertations

May 2021

Fluid Flow and Deformation: Exploring the Relationships Between Fluid Flow, Deformation Mechanisms, Quartz Crystallographic Preferred Orientation Fabric Development, and Kinematics in the Willard Thrust Fault, Utah

Falyn Strey
University of Wisconsin-Milwaukee

Follow this and additional works at: https://dc.uwm.edu/etd

Part of the Geology Commons

FLUID FLOW AND DEFORMATION: EXPLORING THE RELATIONSHIPS

BETWEEN FLUID FLOW, DEFORMATION MECHANISMS, QUARTZ

CRYSTALLOGRAPHIC PREFERRED ORIENTATION FABRIC

DEVELOPMENT, AND KINEMATICS IN THE WILLARD THRUST FAULT,

UTAH

by

Falyn Strey

A Thesis Submitted in

Partial Fulfillment of the

Requirements for the Degree of

Master of Science

in Geosciences

at

The University of Wisconsin-Milwaukee

May 2021

ABSTRACT

FLUID FLOW AND DEFORMATION: EXPLORING THE RELATIONSHIPS
BETWEEN FLUID FLOW, DEFORMATION MECHANISMS, QUARTZ
CRYSTALLOGRAPHIC PREFERRED ORIENTATION FABRIC
DEVELOPMENT, AND KINEMATICS IN THE WILLARD THRUST FAULT,
UTAH

by

Falyn Strey

The University of Wisconsin-Milwaukee, 2021
Under the Supervision of Professor Dyanna Czeck

Thirty-four quartz-rich samples were collected across the Willard thrust fault in Utah to explore the effects that fluid has on faulting. In particular, the relationships between fluid, deformation mechanisms, crystallographic preferred orientation (CPO) fabric development, and kinematic vorticity were investigated.

A petrographic analysis of all 34 samples determined the relative contributions of brittle fracturing, crystal plasticity, and diffusional processes along with their possible relation to fluid interaction. Crystal plasticity dominates throughout most of the field area except where significant contributions from diffusive deformation occurs in rocks with significant mica concentrations and fine grain sizes, especially those located near the fault. The degree of fluid interaction and each deformation mechanism was also compared to each sample's mineralogy, grain size, and fault proximity. Generally, increased fluid interaction enhanced either brittle mechanisms (in coarse grained, quartz rich samples) or diffusive deformation (in fine grained samples). Fault proximity also influenced fluid intensity and deformation mechanisms. The closer the samples were to the fault, the more fluid interaction and diffusion were present,

consistent with earlier work that suggested the fault acted as a channel for syndeformational fluids.

Electron backscatter diffraction (EBSD) was used to further investigate the relationship between fluid intensity and dominant deformation mechanisms, and to also explore relationships between these factors and vorticity, fabric strength, and quartz slip system activation. Sixteen samples were selected for this analysis. Overall, the samples produced weak CPO fabrics, suggesting deformation by crystal plasticity with contributions from diffusion. Because of the weak patterns, a quantitative vorticity analysis was not completed, but a qualitative analysis showed that both pure and simple shear components were present during deformation. Quartz CPO was strongest in samples close to the fault with high quartz concentrations. It also had a weaker, positive correlation to fluid interaction and grain size. Generally, samples closer to the fault displayed pole figure geometries with active slip systems associated with higher temperatures, suggesting that hydrothermal heating may have occurred as fluids were channeled along the fault.

Crystal plasticity was the primary mechanism that allowed rocks to deform on both the footwall and hanging wall. The highest degree of crystal plasticity and diffusive deformation occurred near the fault, as evidenced by the strongest CPO fabrics and microstructures related to diffusional deformation. It is likely that the concentrated diffusional deformation occurred due to the channelized fluid low along the fault, which may have been continuous, cyclical, or sporadic.

Overall, deformation mechanism was controlled by a variety of factors with the presence of fluid being of primary importance. Proximity to the fault (not unrelated to the presence of fluid) and quartz concentrations also played a significant role, and grain size exerted control to a lesser degree.

TABLE OF CONTENTS

LIST OF FIGURES

LIST OF TABLES

ACKNOWLEDGEMENTS

I would first like to thank my advisor, Dyanna Czeck, for her continued support and encouragement. She not only helped from an academic standpoint, through conversation and assistance in field study, but also from a personal standpoint, providing reassurance throughout my thesis. I thank Adolph Yonkee who also assisted in the field study and provided a lot of useful insight on the geology of the Willard fault.

Thanks to Bil Schneider for his assistance with the EBSD portion of this project. I was unable to run the samples personally, but Bil was kind enough to take the time to run them for me. I would also like to thank Zach Michels and Nick Roberts for providing Matlab scripts and helping me understand the program.

x

1. Introduction

Faults can control the location of various geologic hazards, such as earthquakes and landslides, affect surficial landscape and topography, and influence groundwater flow, hydrocarbon migration, and mineral deposition. Accordingly, understanding faults, their associated fluid flow properties, and deformation mechanisms is important. This project aims to provide a deeper understanding of the effect that fluids have on deformation mechanisms, crystallographic preferred orientation (CPO) fabric development, and fault kinematics. Quartz-rich rocks from the Willard thrust fault in Utah, which has a documented relationship between fluid and strain (Yonkee et al., 2013), will be used explore these relationships.

1.1 Fluids in Deformation

The presence of fluids throughout the lithosphere is extensive and can have a myriad of effects on various geological processes. Fluids can influence the nature and occurrence of mineral and hydrocarbon resources and can affect styles of deformation. Fluid's effects on deformation range from micro- to macro-scale, brittle to ductile mechanisms, and mechanical to chemical interactions (Carter et al., 1990). The Willard thrust fault provides an example of a fault that deformed in the presence of fluids. This is indicated by the presence of geochemical alteration, localized veining, and some microstructures like dissolution seams attributed to fluid-assisted deformation (Yonkee, 2005; Barszewski, 2012; Yonkee et al., 2013).

Temperature plays a major role in determining the style of deformation and mechanical and chemical effects created by fluid-rock interactions (Carter et al., 1990; O'Kane et al., 2007). At temperatures less than ~150 °C, mechanical effects dominate by enhancing brittle failure

1

through pressure-induced fracturing (Fischer & Paterson, 1989). At the grain-scale, this is evidenced by microfractures, microveins, and fluid inclusion planes (Onasch, 1990; Lespinasse, 1999; Laubach, 2004). Mechanical fluid-rock interactions are also prevalent at higher temperatures. For example, fluids promote hydrolytic weakening and facilitate grain-boundary migration. These processes drive deformation to be more ductile and increase the role of crystal plasticity (Griggs & Blacic 1965; Griggs, 1967; Paterson, 1989).

The significance of chemical fluid-rock interactions increases at temperatures greater than ~300 °C. At these temperatures, fluids can enhance diffusive mass transfer (Rutter, 1983). Additionally, they can promote metamorphic reactions that can alter the strength of the rock (Carter et al., 1990). Metamorphism associated with the infiltration of fluids along fault zones is typically retrograde metamorphism, or fluid consuming, and produce weaker rocks containing sheet silicate or carbonate minerals. Examples include the serpentinization of olivine and pyroxene in ultramafic rocks and the sericitization of feldspars (Putnis & Austrheim, 2010; Jamtveit et al., 2016)

At moderate temperatures, between ~150 °C and ~300 °C, both brittle and ductile effects can be observed and their processes may interact to enhance deformation (O'Kane et al., 2007). For example, brittle microfracturing reduces grain size, resulting in enhanced diffusive mass transfer, increased mineral reactions, and more potential fluid pathways (Den Brok & Spiers, 1991; Steward et al., 2000).

In addition to temperature, the way fluids affect deformation can also be partially controlled by the fluid composition (Wawrzyniec et al., 1999; O'Kane et al., 2007). For example, the infiltration of highly saline fluids can cause sodic metasomatism and albitization (Oliver et al., 1994). Biotite and chlorite formation can be associated with the infiltration of Mg-rich fluid

(Rossi et al. 2005, 2007). Additionally, compared to pure aqueous fluids, carbonic fluids can increase fluid pressure and promote fracturing and brittle failure (Wawrzyniec et al., 1999).

1.11 Fluid Flow along Faults

Faults can act as conduits, channeling fluid flow along high permeability pathways; as barriers, preventing fluid to cross the fault plane; or as some combination of the two. The function of a fault can vary through space and time due to structural and lithological heterogeneities (Caine et al., 1996). Fluid flow properties can be influenced by fault zone architecture, linked to the relative percentages of fault core and damage zone structures, and permeability structure, related to changes in grain size and fracture permeability (Caine et al., 1996). The enhancement or impediment of fluid flow along a fault can affect secondary hydrocarbon migration, flow in faulted aquifers, and the presence of mineral resources.

There are several models that explain how fluids enter a fault zone at different depths and from different sources. Fault zones can be divided into two regions, transitioning at temperatures around 300 °C (Sibson, 1984). The upper seismogenic zone is characterized by brittle deformation and frictional sliding. Below this, a lower zone exists, dominated by plastic deformation mechanisms (Sibson, 1983, 1984). Fluids entering a fault zone can be meteoric, metamorphic, or magmatic in origin.

In the seismogenic zone, seismic pumping is a common model used to describe fluid flow. In this model, stress increases before an earthquake causing dilatancy and the opening of microcracks. In an episodic manner, fluids infiltrate these cracks and then are drawn out as the cracks heal or close following decreased stress after an earthquake (Sibson et al., 1975; Sibson, 1981). Dilatancy pumping is also an important mechanism for fluid flow near the surface. While seismic pumping is directly related to the earthquake cycle, dilatancy pumping is not. Instead,

the dilation of certain structures, such as fault jogs, occurs due to the accumulation of continual

deformation, leading to non-recoverable dilatancy strains (Etheridge et al., 1984; Knipe &

McCaig, 1994; McCaig et al., 2000).

Seismic pumping is suppressed below the seismogenic zone because crystal plastic creep

relieves and decreases stress (Sibson, 1983; McCaig, 1988). However, McCaig (1988) has

suggested that seismic pumping can occur in the plastic deformation zone under the right

conditions. Following an earthquake, hydraulic gradients could drive fluid across the

brittle/plastic transition if stress and dilatancy cycles are significantly out of phase (McCaig,

1988).

Advection, or infiltration, of fluid is a more common mechanism used to explain fluid

flow below the seismogenic zone (Etheridge et al., 1984). Hydraulic gradients (established from

pressure differentials as reactions seal pores and fractures, increasing pore fluid pressure) are

responsible for the upward migration of the fluid (Etheridge et al., 1984; McCaig & Knipe, 1990;

Cox, 2005). Other mechanisms for fluid flow in the plastic regime include thermal convection

(Etheridge et al., 1984) and the flow from an overpressured meteoric reservoir that has been

tectonically emplaced by underthrusting (Beach & Fyfe, 1972; McCaig, 1988).

1.2 Kinematics and Vorticity

Vorticity is defined as the internal rotation of material lines with respect to the principal

strain axes during deformation (van der Pluijm & Marshak, 2004; Fossen, 2016). Vorticity is

quantified by the kinematic vorticity number, W_k, which measures the relative contributions of

pure and simple shear during steady state, ductile deformation (Means et al., 1980; Means,

1994). W_k is a strain-independent measurement of vorticity and ranges from values of 0,

4

representing pure shear, to 1, representing simple shear (Means et al., 1980). Documenting the spatial distribution of the relative amounts of pure vs. simple shear is important because a significant pure shear component implies significant thinning and extrusion, and greater strain and extrusion rates relative to simple shear (Law et al., 2004).

1.3 CPO

CPOs describe the alignment of crystallographic axes, while dimensional preferred fabrics relate to the alignment of grain shapes (van der Pluijm & Marshak, 2004). Deformation may cause CPO in planar or elongate minerals through a variety of processes; such as mechanical rotation, solution transfer, crystal plastic deformation, and dynamic recrystallization (Passchier & Trouw, 1998). However, in equant grain-shaped minerals, dislocation creep is the most important mechanism for creating a CPO, which is visible through electron backscatter diffraction (EBSD) orientation maps (Passchier & Trouw, 1998). Quartz is the most commonly used mineral in CPO studies (Prior et al., 2009) because of its abundance in the earth's crust and the development of substantial quartz CPO databases (Schmid & Casey, 1986). The dependence of quartz CPO fabric development on crystal plastic deformation by dislocation creep (Taylor, 1938; Lister, 1982; Wenk & Christie, 1991) allows inferences to be drawn on the dominant deformation mechanism based on the strength of the CPO.

Commonly, CPOs are displayed as pole figures by plotting the poles to the lattice planes on a stereonet in the fabric reference frame, relative to foliation and lineation. (Prior et al., 1999). Pole figures can display point, girdle, or random distributions. A random distribution signifies the lack of a CPO; therefore, the role of crystal plasticity in deformation can be interpreted as

5

secondary (Wenk & Christie, 1991). If a CPO fabric is present, the pole figure will display either a point or girdle pattern depending on the active slip system (Passchier & Trouw, 1998).

In quartz, c-axes, the crystallographic axis that runs the length of the crystal and coincides with the single optic axis (Akhavan, 2013), are most often plotted to evaluate CPO. The CPO fabrics that develop correlate to the active slip systems. In quartz, there are three main slip planes, basal, rhomb, and prism (Fig. 1). These planes primarily slip in the <a> direction, but at elevated temperatures, prism slip can also occur in the <c> direction (Schmid & Casey, 1986; Stipp et al., 2002).
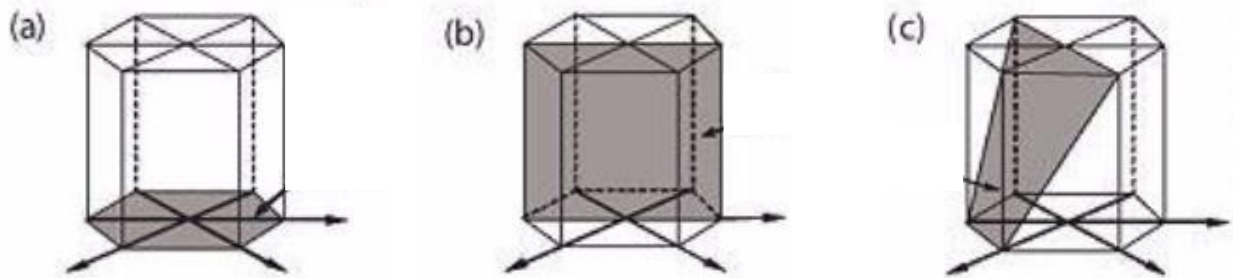
Figure 1. Active slip systems in quartz - basal (a), prism (b), and rhomb (c). Modified from (Burnley, n.d).

Y-axis maxima fabrics result from prism <a> slip. Single girdle fabrics result from combined prism <a> and ± rhomb <a>slip. Type I crossed girdle fabrics result from combined basal <a> and prism <a> slip and type II crossed girdle fabrics result from combined basal <a> and prism <a> slip with increasing constrictional strain (Fig. 2) (Schmid & Casey, 1986; Toy et al., 2008). Stronger CPOs develop from dominant basal <a> slip followed by rhomb <a> and prism [c] slip, and weaker CPOs develop from prism <a> slip (Morales et al., 2014).

It is generally assumed that the primary control of slip system activation in quartz is temperature (Okudaira et al., 1995; Takeshita, 1996). Slip systems activate in the order of basal <a>, ± rhomb <a>, prism <a>, and prism [c] as temperature increases (Hobbs, 1968; Baeta & Ashbee, 1970; Tullis et al., 1973). Stipp et al. (2002) found that a combination of basal <a>, rhomb <a>, and prism <a> slip occurred at

Figure 2. Relationship between active slip systems in quartz and the locations of c-axis peaks on CPO pole figures (Toy et al., 2008). The X/Z reference frame is perpendicular to foliation and parallel to lineation.
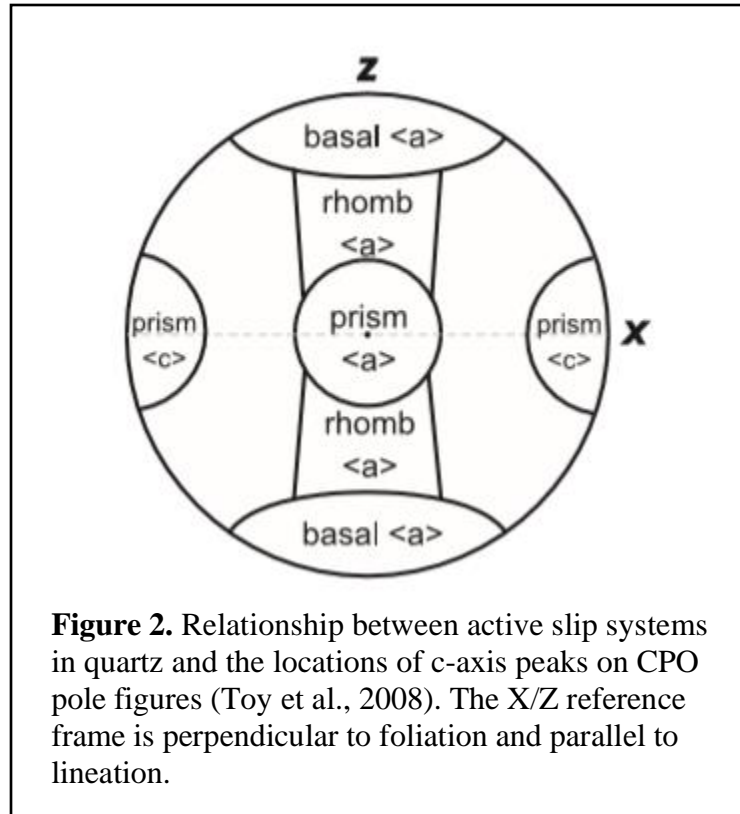
temperatures less than 500 °C. At 500 °C, prism <a> slip was dominant. This correlated to the transition from subgrain rotation to grain boundary migration. At temperatures above 630 °C ±30 °C, prism [c] slip was present (Stipp et al., 2002).

However, Toy et al., (2008) suggest that strain intensity can affect temperature preservation during deformation, making interpretations of CPO fabrics in relation to temperature more complex. CPO fabric development and strength can also be a function of strain magnitude and geometry, the rate of recrystallization, and the presence of other phases (Lister & Hobbs, 1980; Heilbronner & Tullis, 2006; Barth et al., 2010).

CPO patterns are also affected by flow kinematics (Passchier & Trouw, 1998). This relationship can be used to interpret vorticity, the internal rotation of material lines with respect to the principal strain axes during deformation (van der Pluijm & Marshak, 2004; Fossen, 2016),

providing information on the relative contributions of pure and simple shear during steady state, ductile deformation (Means et al., 1980; Means, 1994). When coaxial flow dominates, quartz [c]-axis pole figures show an orthorhombic symmetry, or a crossed girdle pattern (Fig. 3) (Lister & Williams, 1979; Lister & Hobbs, 1980; Law, 1987). Under non-coaxial conditions, pole figures display a monoclinic symmetry, or a single girdle pattern oblique to the shear direction (Fig. 3) (Etchecopar, 1977; Bouchez et al., 1983; Schmid & Casey, 1986; Platt & Behrmann, 1986).

Figure 3. Pole figures of quartz [c]-axes showing a crossed girdle pattern, or orthorhombic symmetry, under coaxial conditions (left) and a single girdle pattern, monoclinic symmetry under increasingly non-coaxial conditions (right). (Hunter et al., 2018).
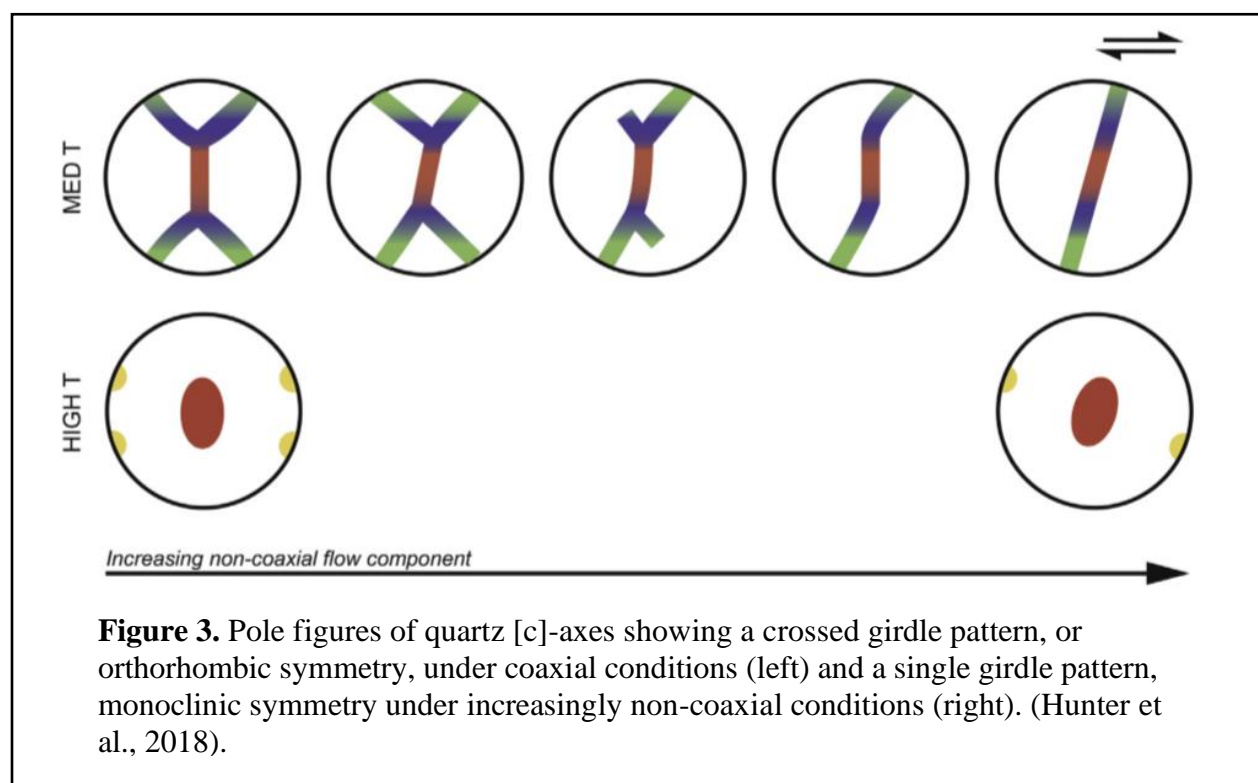
Overall, CPO fabric development and strength are a function of several different factors, including active deformation mechanisms, strain magnitude and geometry, active slip systems and temperature, the rate of crystallization, and the presence of other phases (Barth et al., 2010). This makes CPO fabrics very useful to study, but also complex to interpret. This study exploits the dependence of CPO on active deformation mechanisms to explore the relationships between

fluid presence, deformation mechanisms, and quartz CPO fabric development by systematically relating the results of the CPO analysis to the microstructural study and previous strain quantification analysis (Yonkee et al., 2013).

By using the relationship between CPO and flow kinematics, vorticity and its possible relationship to strain and fluid intensity is also explored. Documenting the spatial distribution of vorticity across the fault plane and across the strain gradient will provide important information on the relative contributions of coaxial vs. noncoaxial deformation components (Means et al., 1980; Means, 1994; Wenk & Christie, 1991; Prior et al., 1999). A significant coaxial component implies significant thinning and extrusion, and greater strain and extrusion rates relative to noncoaxial deformation (Law et al., 2004).

1.4 Research Goals

The main goal of this study is to provide a detailed field example exploring the relationships between fluid, deformation mechanisms, and texture in quartz-rich rocks. Trends in the relative contributions of brittle fracturing, diffusional processes, and crystal plasticity along with their possible relation to fluid interaction are determined.

CPO strength and patterns are analyzed to further explain fluid's role in deformation. In particular, along the Willard fault, all quartz rich rocks show microstructural evidence for crystal plasticity. However, veining and healed microfractures associated with fluid infiltration (Barszewski, 2012; Yonkee et al., 2013) also indicate brittle deformation closer to the fault. It is unknown whether the amount of crystal plasticity increased near the fault, or whether the stronger deformation found there is only due to increased brittle deformation and fluid infiltration, or potentially even a component of enhanced diffusive mass transfer enabled by

9

fluids. Tracking CPO intensity towards the fault can provide information on whether the fluids, in this case, decreased the amount of crystal plasticity by allowing other deformation processes of brittle fracturing and/or diffusive mass transfer to dominate. CPO fabrics are also used to give a relative vorticity estimate, providing information on the relative amounts of coaxial versus noncoaxial deformation components of deformation (kinematic partitioning) within the fault blocks.

2. Geologic Background

2.1 Sevier Orogeny

      The Idaho-Utah-Wyoming (I-U-W) fold and thrust belt, also known as the Sevier orogenic belt, developed during the Sevier orogeny, 140-55 million years ago (Armstrong, 1968). This Late Jurassic/Cretaceous to mid-Paleogene orogenic event occurred in response to the Andean-style subduction of the oceanic Farallon and Kula plates and terrane accretion along the western edge of the North American plate margin (DeCelles, 2004; Yonkee & Weil, 2015). The belt generally trends subparallel to the North American plate margin, NNW to N; however, areas of local to regional curvature exist (Mitra, 1997; Yonkee & Weil, 2015). The Sevier belt is characterized by eastward-directed thrust faults and folds that shortened the region ~150-300 km. and translated strata tens of km. (Royse, 1975; 1993; Price & Mountjoy, 1970; DeCelles & Coogan, 2006). Shortening primarily took place during the Early Cretaceous to Paleogene (Yonkee & Weil, 2015).

      The I-U-W belt is separated into two systems. The western thrust system includes the Willard, Paris, and Meade thrusts, which translate a thicker package of Neoproterozoic to Paleozoic miogeoclinal strata (Coogan, 1992). The eastern thrust system includes the Crawford, Absaroka, Darby-Hogsback, and Prospect thrusts, which carry a thinner package of Paleozoic strata (Coogan, 1992). Synorogenic conglomerates show the age of thrust emplacement, thrust displacement, and duration of motion decreases from west to east (Armstrong & Oriel, 1965; Wiltschko & Dorr, 1983). In particular, slip on the Willard, Paris, and Meade thrusts occurred from ~125-90 million years ago, on the Crawford and Early Absaroka thrusts from ~90-80 million years ago, and the Late Absaroka, Darby-Hogsback, and Prospect thrusts from ~70-50

million years ago (Dorr et al., 1977; Wiltschko & Dorr, 1983; Burtner & Nigrini, 1994; DeCelles, 1994, 2004; Solum & van der Pluijm, 2007; Yonkee & Weil, 2015).

2.2 Willard Thrust Fault

Located in northern Utah, the Willard thrust fault is the westernmost and oldest fault in the I-U-W belt (Crittenden, 1972). The Willard thrust fault is responsible for translating a 10-15 km thick package of rocks ~50 km towards the ESE (Yonkee, 1997). It has a stair-step geometry comprised of two repeating ramps and flats (Yonkee, 2005; Yonkee et al., 2019). A western ramp cuts through Neoproterozoic to Early Cambrian quartzite, followed by a central flat in middle Cambrian shale, an eastern ramp through Cambrian to Jurassic carbonate-rich strata, and an eastern flat in Jurassic evaporites (Yonkee & Weil, 2015; Yonkee et al., 2019) (Fig. 4). Imbricate thrusts and large-scale fault-bend and fault-propagation folds are also present in the Willard thrust sheet (Yonkee, 2005; Yonkee et al., 2019).

Generally, deformation and metamorphism within the Willard thrust sheet increases westward and downward, demonstrated by the increasing intensity of cleavage, veins, and minor faults and folds (Crittenden, 1972; Yonkee, 2005). Mineralogy and fluid inclusion studies show the Willard thrust sheet underwent greenschist-facies metamorphism with peak temperatures of 350-400 °C at depths of 12-15 km. (Yonkee et al., 1989). The footwall reached peak temperatures of 300-350 °C from its burial and warming beneath the hanging wall. Temperatures were highest in the western part of the footwall where burial was the deepest (Yonkee et al., 2003).
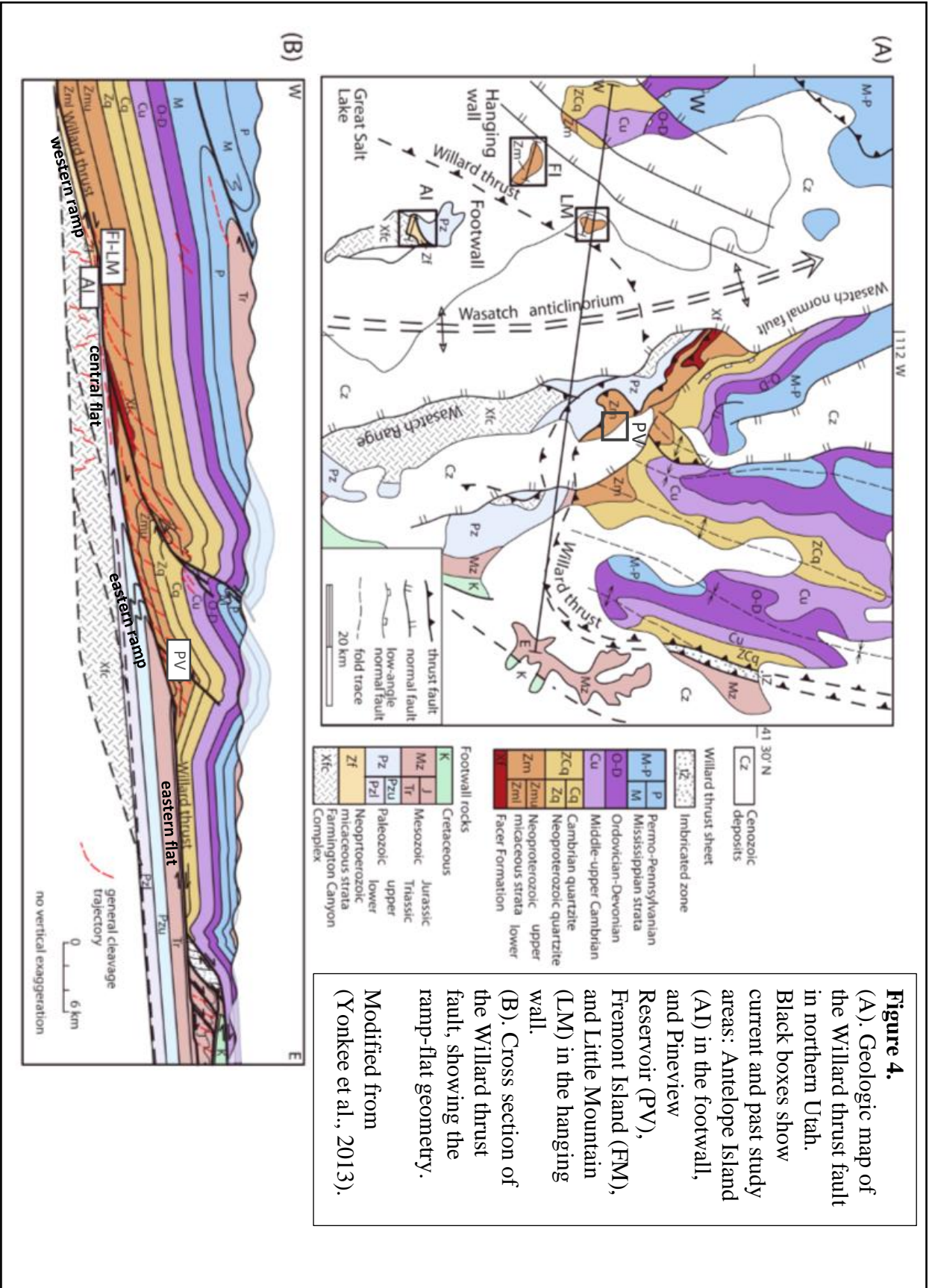
Figure 4. (A). Geologic map of the Willard thrust fault in northern Utah. Black boxes show current and past study areas: Antelope Island (AI) in the footwall, and Pineview Reservoir (PV), Fremont Island (FM), and Little Mountain (LM) in the hanging wall. (B). Cross section of the Willard thrust fault, showing the ramp-flat geometry.

Modified from (Yonkee et al., 2013).

The Willard is characterized by sub-simple shear, with hanging wall strain patterns most closely reflecting a combined kinematic model that includes thrust-parallel shear and thrust-perpendicular (vertical) thinning with volume loss and minor thrust-parallel extension and discrete slip (Yonkee, 2005). Yonkee et al. (2013) show that deformation intensity is higher in the footwall compared to the hanging wall. In the footwall, XZ strain ratios range from ~2-8, compared to values of ~1.5-4 in the hanging wall (Yonkee et al., 2013).

Microtextural, mineralogical, chemical, fluid inclusion, and strain intensity studies provide evidence for fluid-rock interaction during deformation in the Willard (Yonkee et al., 2003, 2013). General downward (up-temperature) fluid flow occurred in the hanging wall, as evidenced by patchy calcite alteration and undersaturated fluids with respect to quartz. In the footwall, fluids being nearly saturated with respect to quartz signifies general upward (down-temperature) fluid flow (Yonkee et al., 2013). Detailed major element geochemical evidence of alteration patterns demonstrate that syn-deformational fluid regimes were separate on each side of the Willard fault (Yonkee et al., 2013). However, apparent fluid flow into the footwall along imbricate faults and deformed veins that cut across the fault zone indicate that the Willard fault acted as a conduit for fault parallel flow in addition to acting as a barrier to cross-fault flow (Yonkee et al., 2013).

2.3 Local Geology and Rock Units

Several rock units were selected for this study to encompass both sides of the fault and provide quartz-rich samples. Rock units deemed most appropriate for this study include the Neoproterozoic Mineral Fork Formation diamictites and the overlying Cambrian Tintic quartzite located on Antelope Island in the footwall and the Neoproterozoic Perry Canyon Formation graywackes and associated metasedimentary rocks in the hanging wall (Fig. 5). The Mineral Fork and Perry Canyon formations are considered to be correlative units on opposite sides of the fault (Yonkee, 2005). Note that all rock units are metamorphosed, but rock names are used without the prefix "meta" throughout for ease and consistency with regional nomenclature (for example, "diamictite" instead of "metadiamictite").

2.31 Mineral Fork Formation

Clasts comprise 20-60% of the Mineral Fork

Figure 5. Simplified stratigraphic column showing units in the Willard thrust fault. Units used in this study include: Zf-Neoproterozoic strata (Mineral Fork diamictite) and Pz-Paleozoic (Tintic quartzite) from the footwall and Zm-Neoproterozoic micaceous strata (Perry Canyon diamictite). (Yonkee et al., 2013).

diamictite and range in size, from smaller cobbles to 2-meter diameter boulders; in shape, from rounded to angular to commonly flattened and deformed; and in composition, from gneiss to granite to quartzite (Yonkee, 2000). Clasts sit within a micaceous, gritty matrix that consists of variable amounts of sand-sized quartz and feldspar (Yonkee, 2000). Detrital zircons pinpoint the provenance of the diamictite as primarily basement rocks of the Farmington Canyon Complex
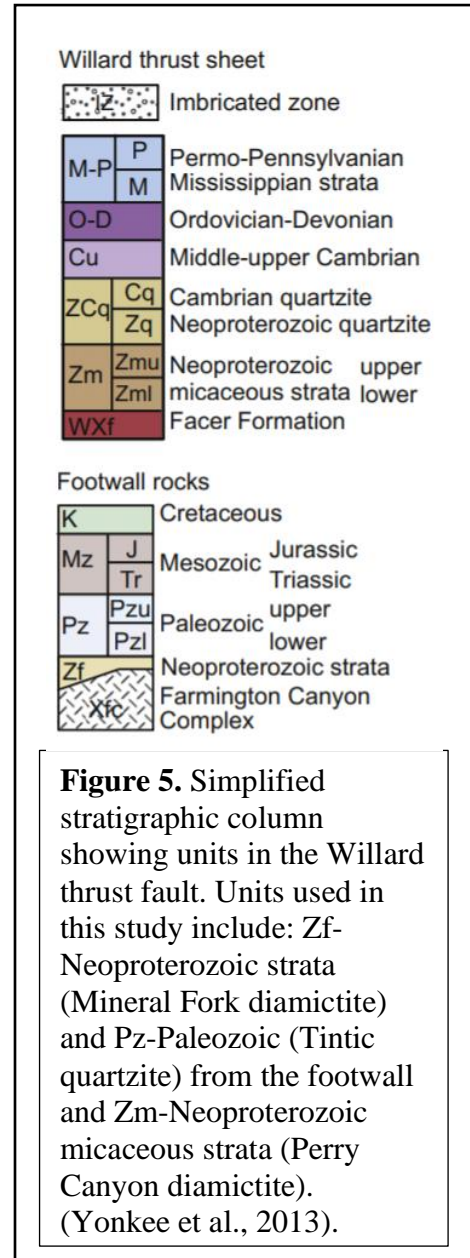
and a lesser contribution from the Wyoming Province, Archean rocks located in Central Wyoming (Yonkee et al., 2013).

Strain, microstructural, and geochemical analyses on this unit document a relationship between strain accumulation and fluid-rock interaction within the footwall exposed on Antelope Island (Yonkee et al., 2013). A strain gradient, characterized by increasing strain toward the WNW (Fig. 6), is accompanied by increased fluid toward the WNW, evidenced by veining and chemical alteration patterns, such as Mg enrichment and Na and Ca depletion in granite clasts (Yonkee et al., 2013). In particular, XZ strain ratios on Antelope Island increase from ~2 to 8 from the east toward the west (Yonkee et al., 2013). The deformation gradient is therefore understood to be related to increased softening from the fluid flow; however, higher temperatures and stresses could also be a factor (Yonkee et al., 2013).

Figure 6. Cross section of Antelope Island with XZ strain/shape fabric ellipses displaying increased strain toward the WNW within the Mineral Fork diamictite (Yonkee et al.,
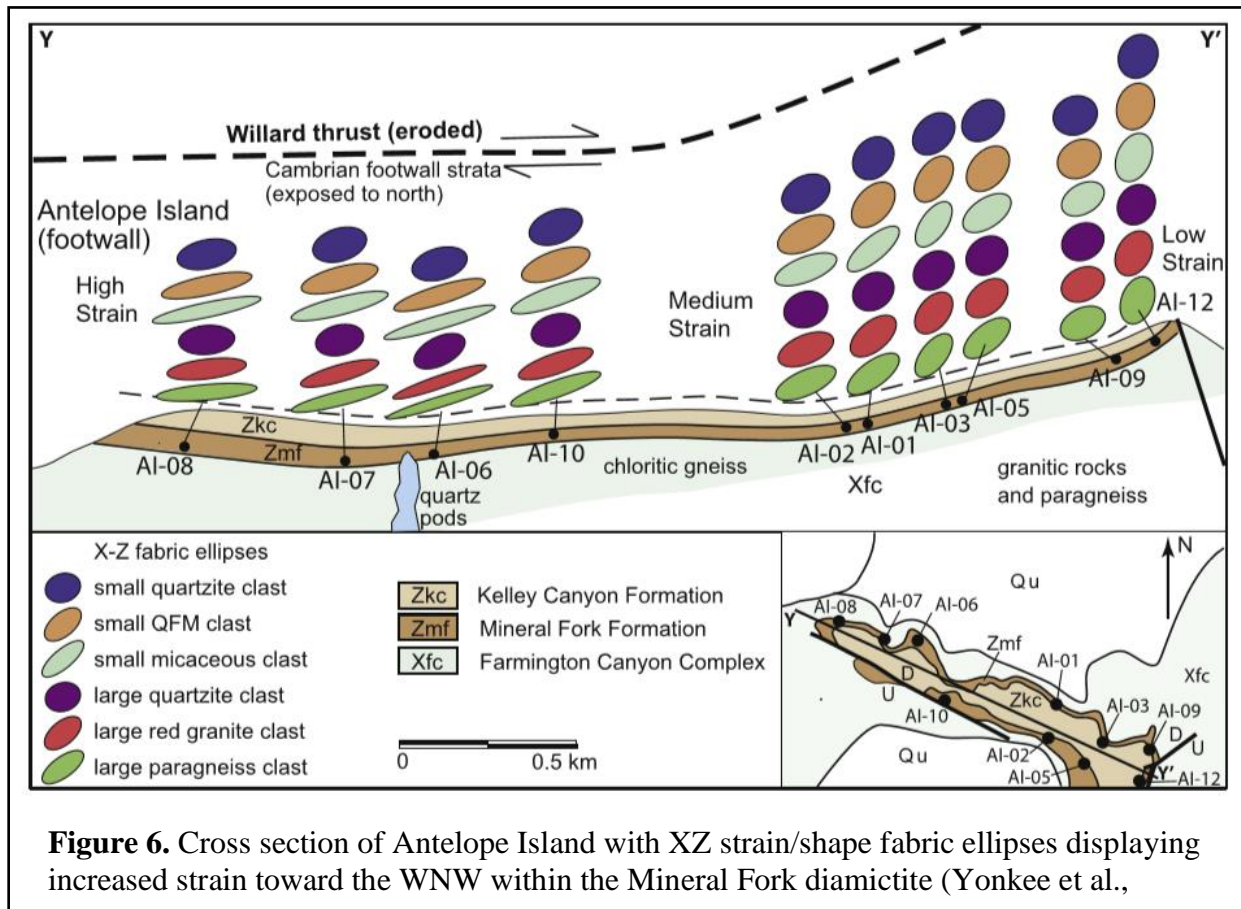
2.32 Cambrian Tintic Quartzite

      On Antelope Island, a lower dolomite member and upper slate member of the Kelly Canyon Formation directly overlie the Mineral Fork diamictite (Yonkee, 2000). Above this, lies the Cambrian Tintic Quartzite. This unit consists of fine- to coarse-grained quartzite, ranging from quartz rich to micaceous, with quartz-pebble conglomerate interbeds (Yonkee, 2000). In northern Antelope Island, it is deformed by eastward-leaning folds and contains stretched pebbles and cobbles (Crittenden, 1972). The Cambrian Tintic Quartzite has no geochemical data to relate to fluid flow, but was an important unit in providing evidence for thrusting related to the Willard (Crittenden, 1972).

2.33 Perry Canyon Formation

      The Neoproterozoic Perry Canyon Formation consists of diamictite- and volcanic-bearing strata (Balgord et al., 2013). There are seven informal members that comprise the formation: (1) arkosic grit at the base; (2) quartzite and grit; (3) pebbly slate with dropstones; (4) slate with interbedded quartzite; (5) mafic volcanic and intrusive rocks; (6) diamictite; and (7) graywacke with rare carbonate layers at the top (Balgord et al., 2013). This formation unconformably overlies the Facer Formation, which is recognized as the source rock for the diamictite member (Balgord et al., 2013).

      Strain analyses have also been conducted on four of the seven informal members of the Perry Canyon Formation (Yonkee, 2005; Yonkee et al., 2013). Hanging wall diamictite samples from Fremont Island and Little Mountain show an overall lesser deformation intensity compared to the footwall, but display a similar trend of increasing strain and evidence for greater fluid flow toward the WNW (Fig. 7) (Yonkee et al., 2013). A difference in alteration patterns between the Mineral Fork diamictite in the footwall and the Perry Canyon diamictite in the hanging wall

indicates a variation in fluid composition, temperature, and fluid flow (Yonkee et al., 2013).

Compartmentalized fluids signify that the fault acted as a barrier to cross-fault flow (Yonkee et al., 2013). Strain patterns in the slate, graywacke, quartzite, and diamictite members from Fremont Island and the Pineview area also document a relationship of increasing strain intensity with decreasing distance from the thrust, and increasing mica content (Yonkee, 2005).

Figure 7. Cross section of Fremont Island and Little Mountain with XZ strain/shape fabric ellipses displaying increased strain toward the WNW within the Perry Canyon diamictite (Yonkee et al., 2013)
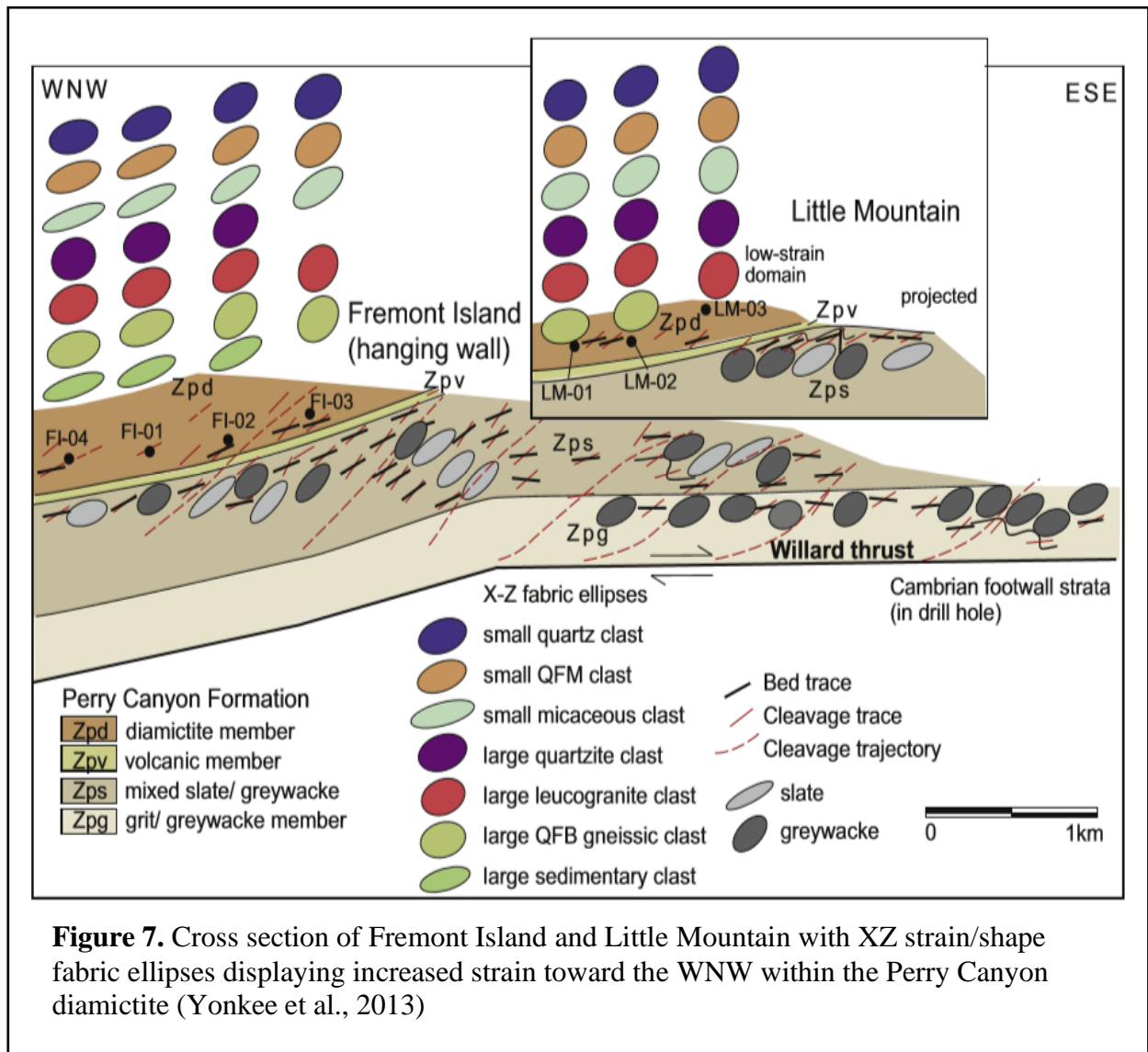
3. Methods

3.1 Field Study

Thirty-four oriented quartz-rich samples were collected throughout the footwall (Antelope Island) and hanging wall (Pineview Reservoir) of the Willard thrust fault. These two locations were chosen because of their proximity to the fault and good exposure of the targeted quartz-rich units. Sampled outcrops were selected from the units based on their relatively high quartz content and range of apparent strain levels. A structural analysis was performed at each sampled outcrop, measuring foliation and lineation when visible, and recording any small-scale structures, such as folds and shear zones. Samples within outcrops were selected based on their distance from veins, large pebbles/clasts, and localized shear zones to minimize local structural effects on the observed fabrics. Collected samples display a variance in strain intensity, lithology, and proximity to the fault.

Figure 8. Diagram showing how an outcrop's distance from the fault was determined.
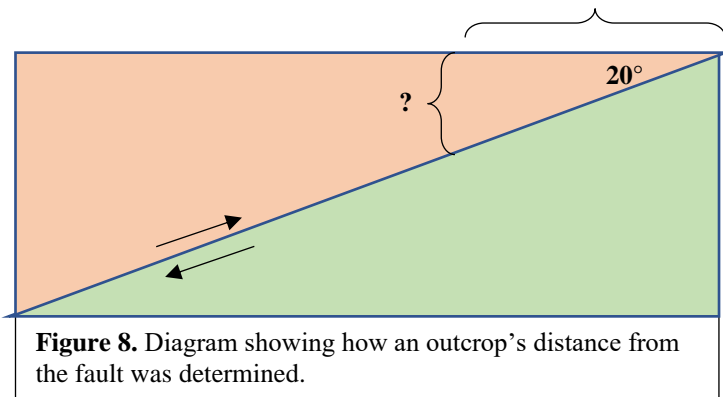
Each sampled outcrop's distance to the fault was determined using trigonometry, using the horizontal distance of the outcrop to the fault and a dip of 20 degrees for the thrust (Fig. 8).

All samples were cut into thin sections along the XZ plane, parallel to lineation and perpendicular to foliation. When present, the fabrics observed on each sample were used to determine the XZ plane. The XZ plane for samples lacking a visible lineation and/or foliation

19

was determined by field measurements at the outcrop scale. Billets were cut with their long side parallel to lineation on the XZ plane. Small saw cuts were made on the down dip side of the billet for orientation. Thin sections were processed by Wagner Petrographic.

3.2 Petrographic Analysis

All 34 thin sections were studied using a petrographic microscope for qualitative microstructural analysis. Previous microstructural analyses on Perry Canyon diamictite from the hanging wall and Mineral Fork diamictite from the footwall provide evidence for brittle deformation, crystal plasticity, and diffusive mass transfer (Barszewski, 2012). Barszewski's (2012) research provided a framework for expected microstructural features in this study.

In this study, the following microstructures were examined: intergranular fractures, intragranular fractures, fractal geometries, microveins, microboudins, plagioclase lamellae, mica foliation, quartz undulose extinction, quartz lamellae, ribbon quartz, quartz necklaces, quartz sugary texture, quartz subgrain formation, triple junctions, selvage seams, stylolitic/sutured grain boundaries, strain shadows, feldspar alteration/sericitization, and fluid inclusion planes.

The presence and qualitative abundance (low, moderate, or high) of each microstructure were tracked across each sample. This qualitative ranking system was determined by visual observations.

Microstructures were grouped by their associated deformation mechanism and relation to the presence of fluid during deformation (Table 1). The relative abundance of each deformation mechanism and fluid-interaction (low, moderate, or high) was determined for each sample based on the combined relative frequencies of each individual microstructure within the category.

Brittle deformation microstructures	Crystal plastic deformation microstructures	Diffusive mass transfer deformation microstructures	Fluid-related microstructures
Intergranular fractures Intragranular fractures Fractal geometries Microboudins Microveins	Plagioclase lamellae Mica foliation Quartz undulose extinction Quartz lamellae Ribbon quartz Quartz necklaces Quartz sugary texture Quartz subgrain formation Triple junctions	Selvage seams Stylolitic/sutured grain boundaries Strain shadows	Feldspar alteration/sericitization Fluid inclusion planes Strain shadows Selvage seams Microveins

Table 1. List of examined microstructures, grouped by their associated deformation mechanism and relation to fluid interaction.

Average grain size for each sample was determined by dividing the length of a measured transect across a thin section by the number of grains within that transect. Values were checked for accuracy by measuring randomly selected individual grains.

3.3 EBSD

Sixteen samples were selected for EBSD analysis (Table 2). Samples were chosen to represent the ranges in lithology, strain intensity, and proximity to the fault in both the hanging wall and footwall. Data were acquired by Bil Schneider at the University of Wisconsin – Madison Department of Geosciences, using a Hitachi S3400 variable pressure scanning electron microscope, with an accelerating voltage of 30 kV.

All computations were calculated from the raw EBSD data using the open source MTEX toolbox for Matlab (Hielscher & Schaeben, 2008). Quartz CPOs are displayed as one point per grain pole figures, which were created using a script from Zach Michels. Pole figures are plotted on equal area lower hemisphere projections in the fabric reference frame, relative to foliation and lineation. The strength of the CPO was measured using the M-index, which measures fabric strength based on the distribution of uncorrelated misorientation angles (Skemer et al., 2005). An example script for calculating the M-index is provided in Mainprice et al. (2014). Additionally, pole figures are contoured according to increments of multiples of uniform distribution (m.u.d.), which serves as a supplementary proxy for the intensity of a fabric (a m.u.d. significantly greater than 1 indicates the presence of a fabric) (Bland et al., 2011).

The degree of coaxial vs. noncoaxial contributions to strain (vorticity) was estimated by the symmetry, S, of the CPO girdles, which describes the proportional difference in intensity between the trailing edge girdle and the leading edge girdle in the same hemisphere (Hunter et al., 2018). An S of 1 relates to orthorhombic symmetry (coaxial deformation) and an S of 0 relates to monoclinic symmetry (non-coaxial deformation) (Hunter et al., 2018). S was calculated using the script provided by Hunter et al. (2018).

	Formation	Lithology Details	Sample
Footwall	Mineral Fork	Medium strain diamictite quartzite interlayer	AI1901A
			AI1901B
			AI1901C
			AI1901D
		High strain diamictite quartzite interlayer	AI1902A
			AI1902B
			AI1903A
			AI1903B
	Tintic	Quartzite (pink/green)	AI1904A
		Quartzite (clast)	AI1904B
		Quartzite (green)	AI1904C
		Quartzite (pink)	**AI1904D**
		Quartzite (pink/green)	AI1905A
		Quartzite (clast)	**AI1905B**
		Quartzite (pink)	AI1905C
		Quartzite (green)	**AI1905D**
		Quartzite (green)	**AI1906A**
		Quartzite (pink)	**AI1906B**
		Quartzite (clast)	AI1906C
		Quartzite (pink)	**AI1907A**
		Quartzite (clast)	**AI1907B**
		Quartzite (green)	**AI1907C**
		Quartzite (pink/green)	AI1907D
		Quartzite (clast)	AI1907E
Hanging Wall	Perry Canyon	Graywacke (massive)	PV1901A
			PV1901B
			PV1901C
			PV1901D
		Graywacke (thinly bedded)	**PV1901E**
			PV1901F
			PV1901G
		Graywacke (shaly)	**PV1901H**
			PV1901I
		Graywacke (thinly bedded)	**PV1902A**

Table 2. A list of collected samples. Samples selected for EBSD analysis are bolded and highlighted in green.

4. Field Study

4.1 Results

Twenty-four samples were collected from the footwall on Antelope Island (Fig. 9). Eight of these samples are from interbedded quartzite layers in diamictite from the Mineral Fork Formation, collected from three different locations (Fig. 10). Two to four samples were collected from each location and, when possible, represented the range of grain size (fine-grained to gritty) and quartz concentration (micaceous to quartzitic) at each location. Samples from AI1901 have low to medium strain and range in grain size and quartz concentration. Samples from AI1902, have high strain and a finer quartzitic grain size. Samples from AI1903 have high strain and are more micaceous (Table 3).

The remaining sixteen footwall samples were taken from the Tintic Quartzite at four different locations: AI1904, AI1905, and AI1906, and AI1907 (Fig. 12). Three to five samples were taken from each location, representing each of the three variations of quartzite present: (1) a very fine-grained, green, and mica-rich quartzite; (2) a fine to medium-grained, pink quartzite; and (3) a clast rich, pebbly quartzite. A large decameter-scale, gentle open fold is present near sample locations AI1904 and AI1905 (Table 3).

Ten samples were collected from two locations in the hanging wall near the Pineview Reservoir in Ogden Valley. All samples are quartzitic graywackes from the Perry Canyon Formation (Fig. 13). Nine samples were taken from the first location, PV1901. This location has three phases of graywacke, which are (from east to west,): (1) massive graywacke with veins, (2) thinly bedded graywacke, and (3) shaly, micaceous graywacke with thinner beds. Only one sample was collected from the second location farther east, PV1902. This sample is a gritty quartzite, most similar to the middle, thinly bedded unit from PV1901 (Table 3).
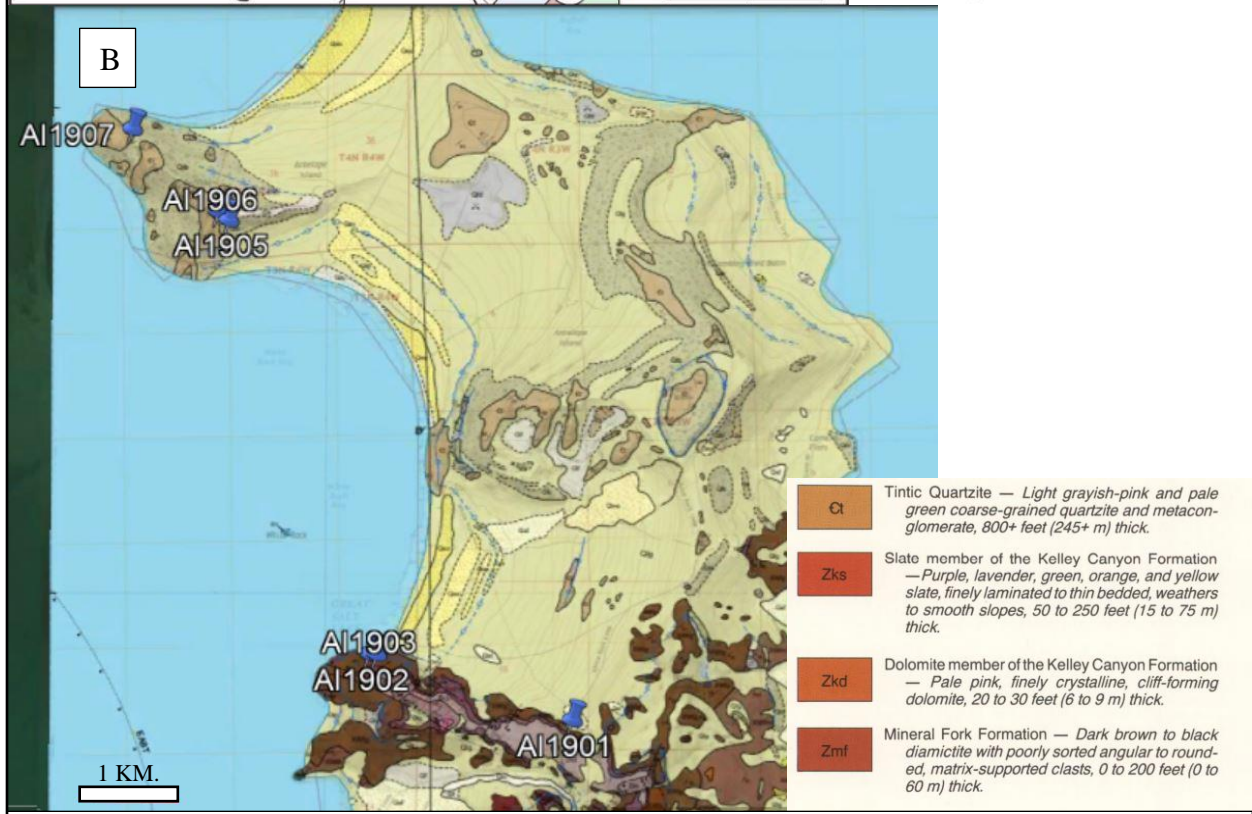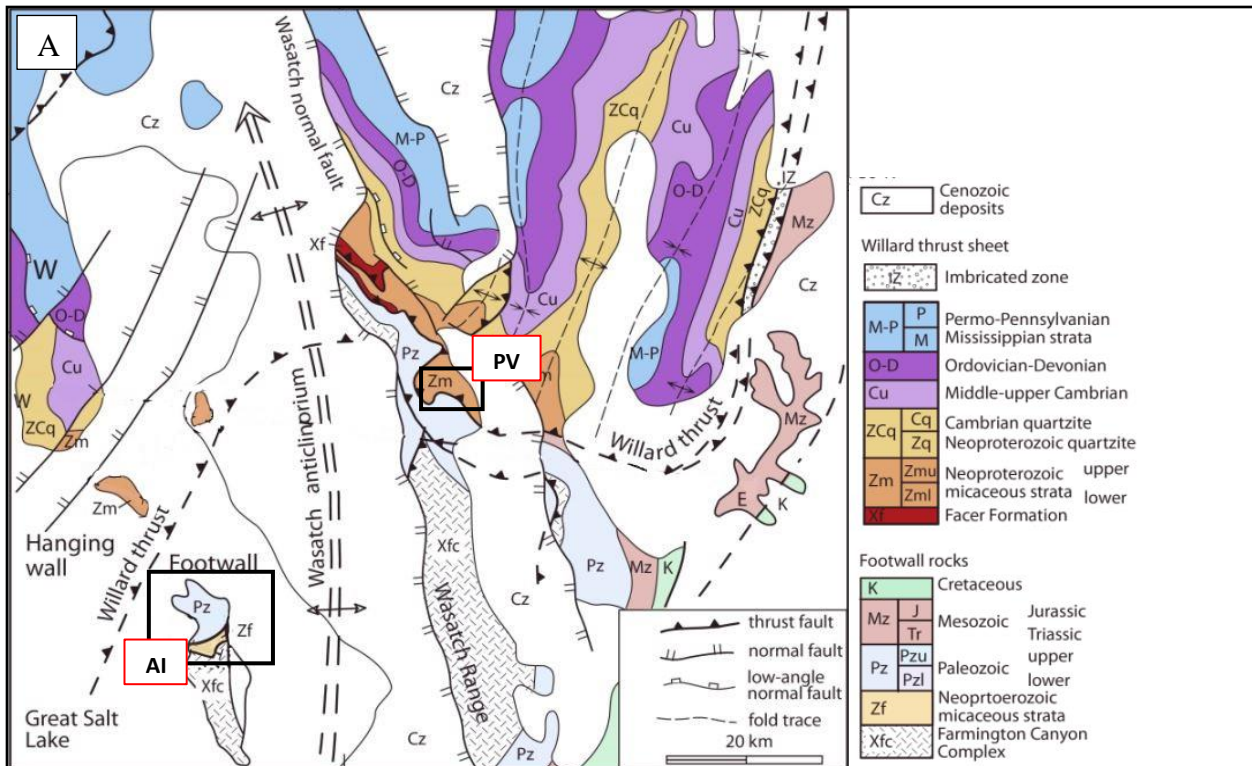
Figure 9. A.) Map of the Willard thrust fault in Utah. Sampling locations AI (Antelope Island) and PV (Pineview Reservoir are labeled. Modified from (Yonkee et al., 2013). Box on north side of AI indicated location of inset map B. B.) Map of sampling locations on Antelope Island. AI1901, 02, and 03 are in Zmf. AI1904, 05, 06, and 07 are in Єt. Modified from (Doelling et al., 1990).

Figure 10. Images of Mineral Fork diamictite at outcrop scale (A and B) and hand-sample scale (C and D).

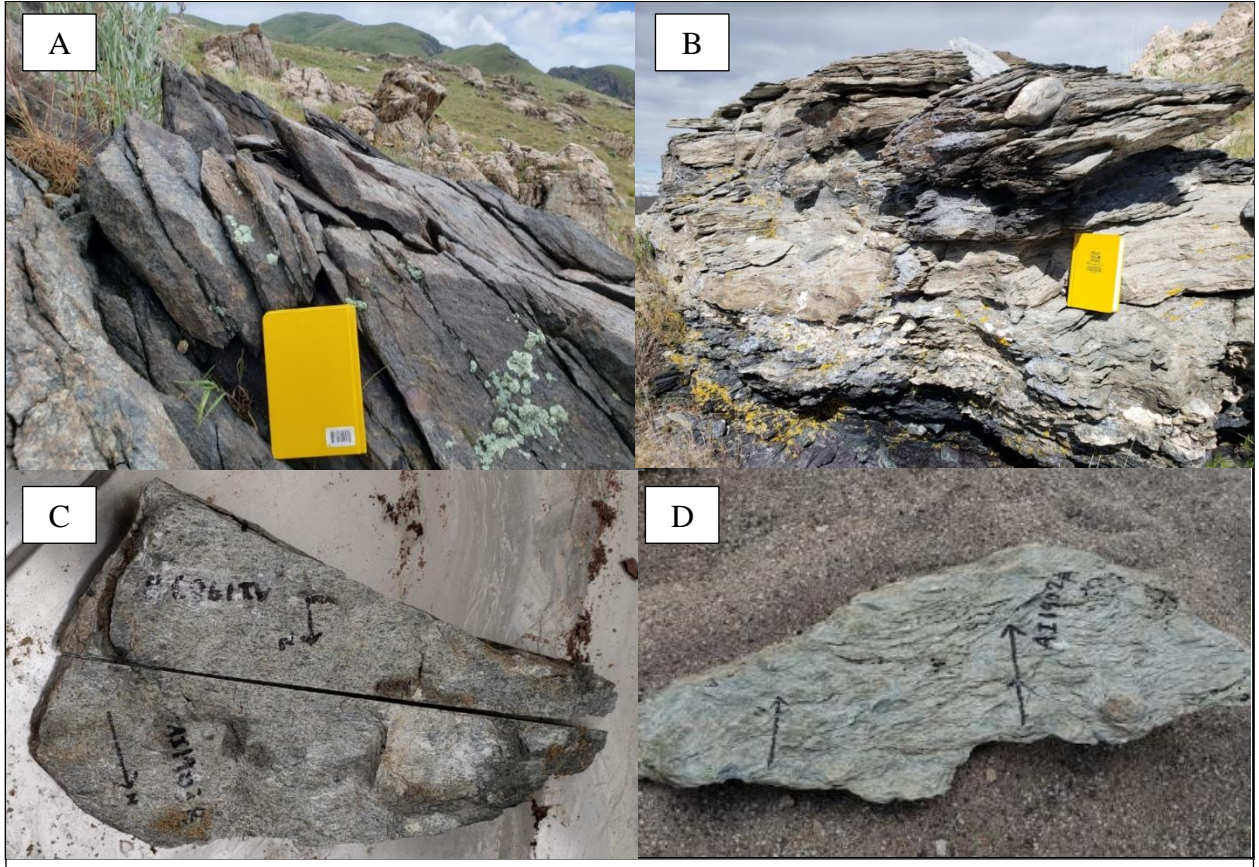| Samples	Lithology Details	Distance to Fault (m.)	GPS Location	Fabric Orientation	Notable Structures
AI1901A	Mineral Fork diamictite quartzite, gritty, medium strain	3263	40°59'12.71"N 112°13'19.25"W	Foliation: 008/49W 002/63W 348/50W 352/55 W Lineation: 51 → 270 x → 275	Small fold below sample AI1901D
AI1901B					
AI1901C	Mineral Fork diamictite quartzite, fine-grained, medium strain				
AI1901D					
AI1902A	Mineral Fork diamictite interlayer, fine-grained, high strain	2435	40°59'34.59"N 112°14'47.35"W	Foliation: 250/35NNW 251/33NNW 268/37N 240/18NW Lineation: 20 → 292 x → 288	
AI1902B					
AI1903A	Mineral Fork diamictite micaceous interlayer, fine-grained, high strain	2426	40°59'34.42"N 112°14'44.04"W	Foliation: 255/21NW 220/12NW 204/12NWW Lineation: 15 → 305 x → 294	
AI1903B					
AI1904A	Tintic quartzite, pink/green, medium-grained	1625	41° 1'58.22"N 112°15'48.78"W	Foliation: 200/49NWW 215/30NW 220/70NW 227/53NW 235/30NW	Southeast limb of large, gentle open fold. Small-scale shear zones are present.
AI1904B	Tintic quartzite conglomerate, clast rich				
AI1904C	Tintic quartzite, green, fine-grained				
AI1904D	Tintic quartzite, pink, fine- to medium-grained				
AI1905A	Tintic quartzite, pink/green, medium-grained	1606	41° 1'58.54"N 112°15'49.09"W	Foliation: 031/32NW 056/65NW 063/69NNW 050/58NW	Northwest limb of large, gentle open fold. Small-scale shear zones are present.
AI1905B	Tintic quartzite conglomerate, clast rich				
AI1905C	Tintic quartzite, pink, fine- to medium-grained				
AI1905D	Tintic quartzite, green, fine-grained				

Sample	Lithology	Proximity to fault	Location	Fabric orientations	Notable structures
AI1906A	Tintic quartzite, green, fine-grained	1561	41° 2'1.32"N 112°15'53.75"W	Foliation: 210/52NW 220/50NW 226/43NW 210/60NW Lineation: x → 095	Farther northwest on limb of large, gentle open fold
AI1906B	Tintic quartzite, pink, fine- to medium-grained				
AI1906C	Tintic quartzite conglomerate, clast rich				
AI1907A	Tintic quartzite, pink, fine- to medium-grained	1115	41° 2'28.97"N 112°16'31.34"W	Foliation: 246/37NW 246/34 NW 241/38NW 258/44NNW 248/58NW	AI1907D and AI1907E are from southeast limb of gentle synform
AI1907B	Tintic quartzite conglomerate, clast rich				
AI1907C	Tintic quartzite, green, fine-grained				
AI1907D	Tintic quartzite, pink/green, medium-grained				
AI1907E	Tintic quartzite conglomerate, clast rich				
PV1901A	Perry Canyon graywacke, massive	100	41°15'31.80"N 111°50'5.13"W	Lineation: 27 → 073	
PV1901B					
PV1901C					
PV1901D					
PV1901E	Perry Canyon graywacke, thinly bedded				
PV1901F					
PV1901G					
PV1901H	Perry Canyon graywacke, micaceous, shaly				
PV1901I					
PV1902A	Perry Canyon graywacke, thinly bedded, gritty	400	41°15'47.25"N 111°49'33.65"W		

Table 3. Describes lithology, proximity to fault, fabric orientations, and notable structures as observed in the field. Lineations are written as plunge → trend. "*x*" represents an unknown plunge. Samples that are bolded and shaded are footwall samples. Samples with no bolding or shading are from the hanging wall.
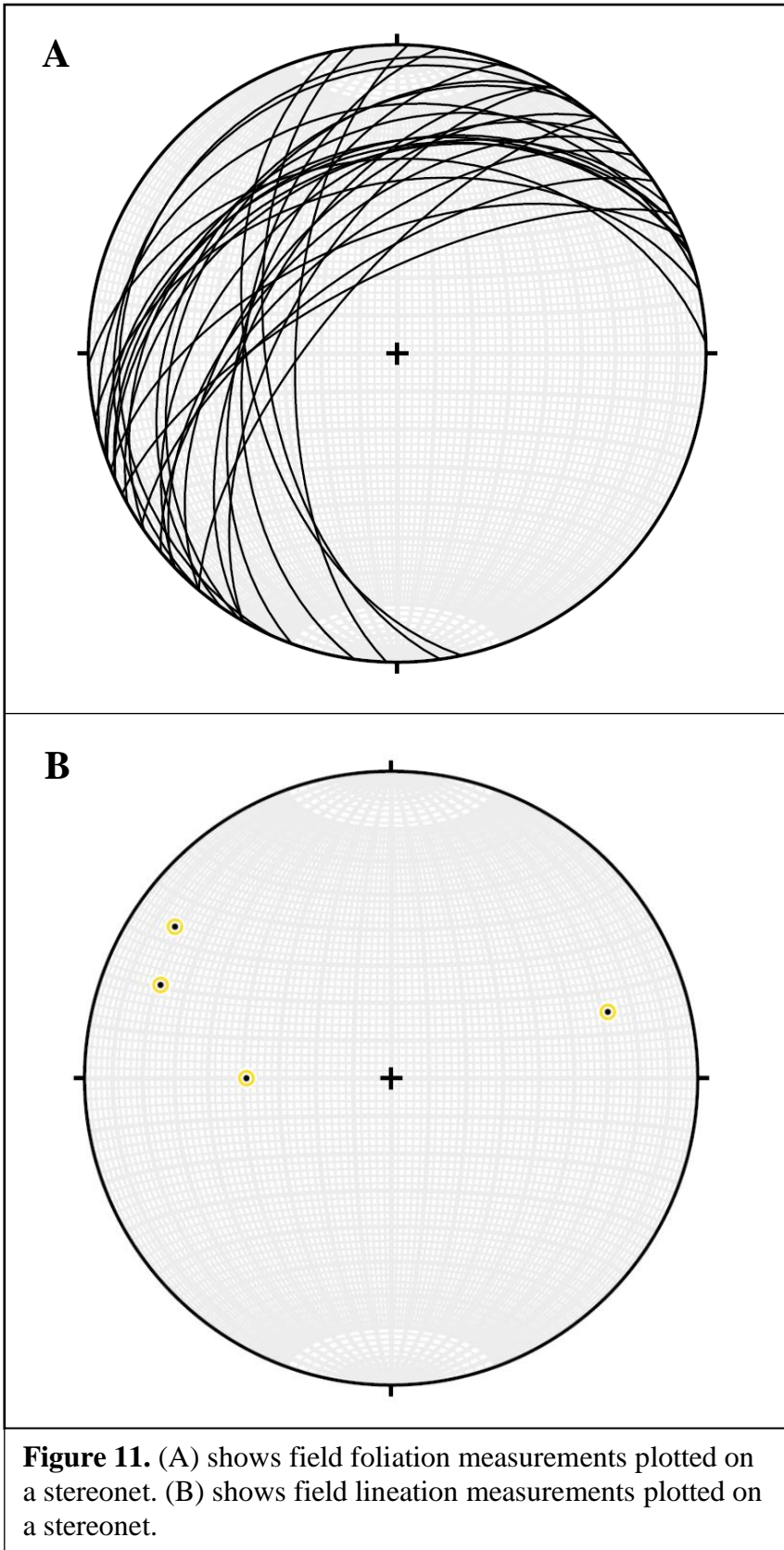
Figure 11. (A) shows field foliation measurements plotted on a stereonet. (B) shows field lineation measurements plotted on a stereonet.
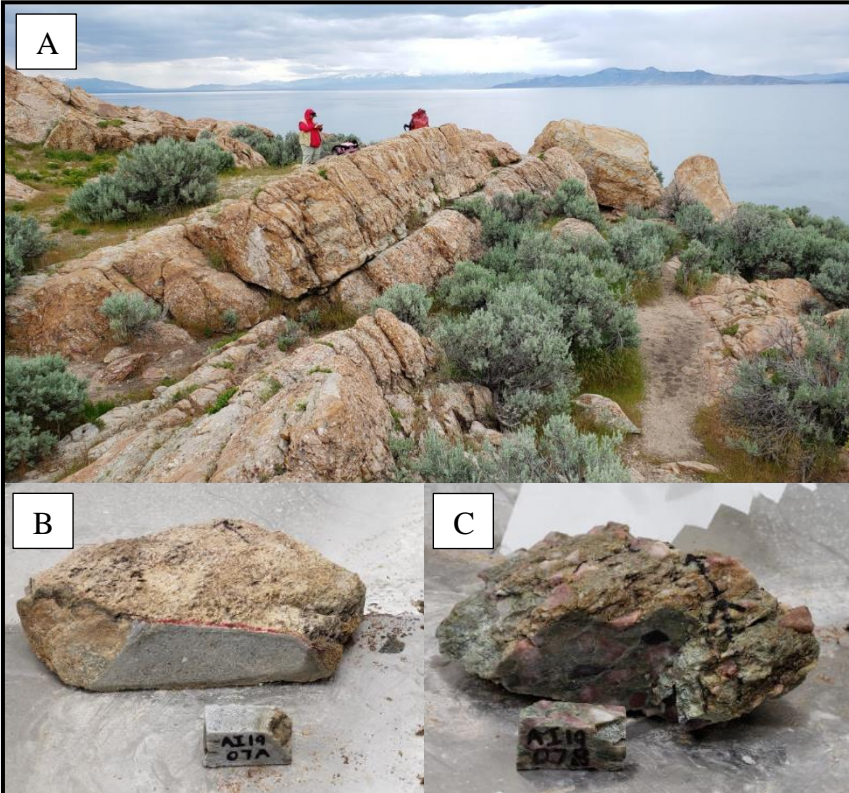
Figure 12. Images of Tintic Quartzite at outcrop scale (A) and hand-sample scale (B and C).

Figure 13. Images of Perry Canyon graywacke at outcrop scale (A) and hand-sample scale (B).

5. Petrographic Analysis

<u>5.1 Results</u>

General observations on the mineralogy, grain size, and fabrics were made across all 34 samples (Table 4). All samples contain various proportions of quartz and mica. Muscovite and slightly lesser amounts of biotite are the predominant types of mica present in the samples. Some samples also contain feldspars and opaque minerals (likely magnetite or hematite). Most samples are primarily comprised of quartz, except for the high strain diamictite samples.

In the high strain diamictite samples (AI1902A,B; AI1903A,B), mica and quartz comprise the majority of the sample. Mica is more abundant than quartz, representing 55-64% of the mineralogy, while quartz represents 34-45%. Unidentifiable opaque minerals (likely magnetite or hematite) are also present in these samples at very low abundances ($\leq 2\%$).

Medium strain diamictite samples (AI1901A,B,C,D) have a larger amount of quartz compared to the high strain samples. Quartz values range from 65-69% and mica values range from 28-30%. Minor amounts of opaque minerals are also present in the medium strain samples (1-5%).

Quartz dominates the Tintic quartzite samples (AI1904A,B,C,D; AI1905A,B,C,D; AI1906A,B,C; AI1907A,B,C,D,E). On average, quartz makes up 85% of the sample, while mica makes up 13%. Generally, more quartz is present in the samples classified as "clast" and "pink" and less quartz is present in the "green" and "green/pink" samples. Minor amounts (1-2%) of plagioclase and K-feldspar are present in most of the Tintic quartzite samples.

Perry Canyon graywacke samples from location PV1901 have the highest quartz content of all samples, averaging 88%. Mica (8%) and opaque minerals ($\leq$ 5%) are present in minor amounts within these samples. In comparison, Perry Canyon graywacke from PV1902 has less quartz (71%) and more mica (22%), opaques (6%), and feldspars (1%).

Perry Canyon graywacke samples have the smallest grain size, averaging 0.14 mm. The shaly graywacke samples, have the smallest grain size (0.1 mm), while the massive and thinly bedded samples are slightly larger (0.15 mm). The sample from site PV1902 has the largest grain size of the Perry Canyon graywackes (0.2 mm). Mineral Fork diamictite samples have the next largest grain size, with high strain samples averaging 0.2 mm and medium strain samples averaging 0.25 mm. Tintic quartzite samples have the largest grain size. Green, micaceous samples range in size from 0.25 to 0.3 mm, with an average size of 0.275 mm; matrix grains from clast-rich samples range from 0.25 to 0.3 mm, averaging 0.28 mm; pink/green samples range in size from 0.25 to 0.35 mm, averaging 0.3 mm; and pink samples range from 0.3 to 0.35 mm, with an average size of 0.325 mm.

Foliation defined by mica is present in most samples. Out of all the samples, the high strain Mineral Fork diamictites have the strongest fabric. This is followed by the shaly, micaceous Perry Canyon graywacke samples (PV1901H,I). All other Perry Canyon graywacke samples from PV1901 also have micaceous foliation, but the fabric is generally weaker. Ten of the sixteen Tintic quartzite samples also have weak mica foliation. Clast-rich samples and samples from site AI1907 have the strongest fabrics, while samples from site AI1904 have the weakest fabrics.

Sample	Location	Lithology	Minerals Present	Grain Size (mm)	Fabric
AI1901A	Footwall	Mineral Fork Medium Strain Diamictite	Quartz > Mica > Opaque	0.25	
AI1901B	Footwall	Mineral Fork Medium Strain Diamictite	Quartz > Mica > Opaque	0.25	
AI1901C	Footwall	Mineral Fork Medium Strain Diamictite	Quartz > Mica > Opaque	0.25	
AI1901D	Footwall	Mineral Fork Medium Strain Diamictite	Quartz > Mica > Opaque	0.25	
AI1902A	Footwall	Mineral Fork High Strain Diamictite	Mica > Quartz > Opaque	0.2	Strong
AI1902B	Footwall	Mineral Fork High Strain Diamictite	Mica > Quartz > Opaque	0.2	Strong
AI1903A	Footwall	Mineral Fork High Strain Diamictite	Mica > Quartz > Opaque	0.2	Strong
AI1903B	Footwall	Mineral Fork High Strain Diamictite	Mica > Quartz > Opaque	0.2	Strong
AI1904A	Footwall	Tintic Quartzite (pink/green)	Quartz >> Mica > Feldspar	0.25	
AI1904B	Footwall	Tintic Quartzite (clast rich)	Quartz >> Mica > Feldspar	0.3	Weak
AI1904C	Footwall	Tintic Quartzite (green micaceous)	Quartz >> Mica > Feldspar	0.25	
AI1904D	Footwall	Tintic Quartzite (pink)	Quartz >> Mica	0.35	
AI1905A	Footwall	Tintic Quartzite (pink/green)	Quartz >> Mica > Feldspar	0.35	Weak-moderate
AI1905B	Footwall	Tintic Quartzite (clast rich)	Quartz >> Mica > Feldspar	0.25	Weak
AI1905C	Footwall	Tintic Quartzite (pink)	Quartz >> Mica > Feldspar	0.3	Weak
AI1905D	Footwall	Tintic Quartzite (green micaceous)	Quartz >> Mica > Feldspar	0.35	
AI1906A	Footwall	Tintic Quartzite (green micaceous)	Quartz >> Mica > Feldspar > Opaque	0.3	Weak
AI1906B	Footwall	Tintic Quartzite (pink)	Quartz >> Mica > Feldspar	0.3	Weak
AI1906C	Footwall	Tintic Quartzite (clast rich)	Quartz >> Mica	0.3	
AI1907A	Footwall	Tintic Quartzite (pink)	Quartz >> Mica > Feldspar	0.3	Weak-moderate
AI1907B	Footwall	Tintic Quartzite (clast rich)	Quartz >> Mica > Feldspar	0.25	Moderate
AI1907C	Footwall	Tintic Quartzite (green micaceous)	Quartz >> Mica > Feldspar	0.25	
AI1907D	Footwall	Tintic Quartzite (pink/green)	Quartz >> Mica > Feldspar > Opaque	0.3	Weak-moderate
AI1907E	Footwall	Tintic Quartzite (clast rich)	Quartz >> Mica	0.3	Moderate
PV1901A	Hanging Wall	Perry Canyon Graywacke	Quartz >> Mica	0.1	Moderate
PV1901B	Hanging Wall	Perry Canyon Graywacke	Quartz >> Mica > Opaque	0.15	Weak
PV1901C	Hanging Wall	Perry Canyon Graywacke	Quartz >> Mica > Opaque	0.15	Weak
PV1901D	Hanging Wall	Perry Canyon Graywacke	Quartz >> Mica > Opaque	0.15	Weak
PV1901E	Hanging Wall	Perry Canyon Graywacke	Quartz >> Mica > Opaque	0.15	Weak
PV1901F	Hanging Wall	Perry Canyon Graywacke	Quartz >> Mica > Opaque	0.15	Weak
PV1901G	Hanging Wall	Perry Canyon Graywacke	Quartz >> Mica > Opaque	0.15	Weak
PV1901H	Hanging Wall	Perry Canyon Graywacke	Quartz >> Mica > Opaque	0.1	Strong
PV1901I	Hanging Wall	Perry Canyon Graywacke	Quartz >> Mica > Opaque	0.1	Strong
PV1902A	Hanging Wall	Perry Canyon Graywacke	Quartz >> Mica > Opaque > Feldspar	0.2	

Table 4. Summary table includes mineralogy, grain size (diameter), and fabric strength for each sample.

Microstructures were studied in further detail. A variety of microstructures were observed within the samples, ranging in occurrence and intensity. Table 5 contains the frequency of the examined microstructures across all samples. Other microstructures, such as quartz necklaces, quartz sugary texture, and fractal geometries were also looked for, but were not observed in any sample and are therefore not included in the table. All thin sections had microstructures related to crystal plasticity. All samples except PV1901H showed evidence of brittle deformation. Most samples also had evidence of diffusion as well. The most common microstructure present was quartz undulose extinction, while the least common microstructures were triple junctions, ribbon quartz, and sutured grain boundaries. The occurrence of individual microstructures is discussed in detail by lithology in the subsections below.

Figures 14-17 show the relative abundance of brittle deformation, crystal plastic deformation, diffusive deformation, and fluid interaction for each lithology based on each sample's combined frequencies of individual microstructures within each deformation category. Generally, the massive graywacke samples from the Perry Canyon formation have the highest frequency of brittle microstructures, ranging from moderate to moderate-high. The Tintic quartzite samples have the next highest frequency, ranging from low-moderate to moderate-high. The Mineral Fork diamictite samples and the remaining Perry Canyon samples have a low frequency of brittle microstructures (Fig. 14).

Crystal plastic deformation microstructures are most present in Tintic quartzite from the sampling locations AI1904 and AI1905 and from the medium strain Mineral Fork diamictite samples. Both are classified as moderate-high to high frequency. The Tintic quartzite samples from AI1906 and AI1907, along with the Perry Canyon graywacke samples all have a moderate

frequency of crystal plastic deformation. High strain Mineral Fork diamictite samples display the least amount of microstructures relating to crystal plastic deformation (Fig. 15).

Microstructures related to diffusion are most common in the high strain Mineral Fork diamictite and the Perry Canyon graywacke from site PV1901. Tintic quartzite samples, medium strain Mineral Fork diamictite samples, and Perry Canyon graywacke from PV1902 have relatively little evidence for deformation by diffusion (Fig. 16).

Microstructures related to fluid interaction during deformation include some in the diffusion category (selvage seams and strain shadows), brittle category (microveins), and otherwise noncategorized (alteration/sericitization of feldspar and fluid inclusion planes). They are most prevalent in Tintic quartzite with frequencies ranging from moderate to high. This is closely followed by the massive and thinly bedded Perry Canyon graywackes from PV1901. The Mineral Fork diamictite, dirty/shaly Perry Canyon graywacke, and PV1902 Perry Canyon graywacke samples have the least evidence for fluid interaction (Fig. 17).

Table 5 columns grouped under: **Brittle Deformation**, **Crystal-Plasticity**, **Diffusive Deformation**, **Fluid Interaction**

Location and Lithology	Sample	Intergranular fracture	Intragranular Fractures	Microveins	Plagioclase Lamellae	Mica Foliation	Quartz Undulose Extinction	Quartz Lamellae	Ribbon Quartz (elongated quartz)	Quartz Subgrain Formation	Triple Junctions	Selvage Seams	Stylolitic/ Sutured Grain Boundaries	Strain Shadows	Alteration/ Sericitization in Feldspar	Fluid Inclusion Planes
Footwall Med. Strain Diamictite	AI1901A		X	X			XX	X		XXXXX		X		X		X
	AI1901B		X	X			XXX	X		XXXX				P		P
	AI1901C		X	X			XXX			XXX						P
	AI1901D		X	X			XXX			XXX	P					
Footwall High Strain Diamictite	AI1902A		X	X		XXXXX	XX			XX		XX	X	X		
	AI1902B		X	X		XXXXX	X	X				XXXX	X			
	AI1903A		X	X		XXXXX	XX			X		XX		XXXX		
	AI1903B		X	X		XXXXX	XX					XX		XXXX		
Footwall Tintic Quartzite	AI1904A	X	X	X	XXX		XXXXX	XXX		X					X	X
	AI1904B		XX	X	XX	X	XXX	X		X		X			X	XX
	AI1904C	X	XXX	XXX	XX		XXXX	XX		XX					XXX	X
	AI1904D	X	XX	XX	X		XXXX	XXXXX							XX	X
	AI1905A		XX	XX	X	XX	XXXX	XXXX		X				XX	X	XX
	AI1905B	X	XX	XX	X	X	XXXX	X		X				XX	P	P
	AI1905C	X	XX	X	X	X	XXXXX	XX		X				XXX	P	XX
	AI1905D		XX	X	X		XXXX	XXX		X					XXX	XXX
	AI1906A		X	X	X	X	XXXXX					XXX		XXX		X
	AI1906B		X	X	XX	X	XXXX	X		X					XX	X
	AI1906C	XXX	XXX	XXXX	X		XXXX	X							XX	XX
	AI1907A	X	XX	X	X	XX	XXXXX			X				X	XX	XX
	AI1907B		X	X	X	XXX	XXX			X				XX	XXX	XX
	AI1907C		X	X	X		XXX	X		XX					XXX	XX
	AI1907D		X	X	X	XX	XXXX	X		X				X	X	XX
	AI1907E		XX			XXX	XXXXX	X						X	XX	XX
Hanging Wall Perry Canyon Graywacke	PV1901A	XX		XXXX		XXX	XXXXX			X		XXXX		XXXX		P
	PV1901B	XXX		XXX		X	XXXXX	XX	X	X		XXX		XXX		XX
	PV1901C	X	X	XX		X	XXXXX	XXX				XXXX		XX		P
	PV1901D	X	X	XX		X	XXXXX	X	X	X		XXX		XX		
	PV1901E	X		X		X	XXXXX	X				XXX		XX		
	PV1901F	X	X	X		X	XXXXX	X				XXX		XXX		
	PV1901G		X			X	XXXXX	X				XXXX		XXX		
	PV1901H					XXXX	XXXX	X		X		XXXXX		XXXXX		
	PV1901I		X			XXXX	XXXXX	X		X		XXXXX		XXXXX		
	PV1902A		X		X		XXXX	X		X					XX	

Table 5. Contains the frequency of the examined microstructures for all samples. The following abbreviations are used to describe the frequency of present microstructures: present (P), low (X), low to moderate (XX), moderate (XXX), moderate to high (XXXX), and high (XXXXX).
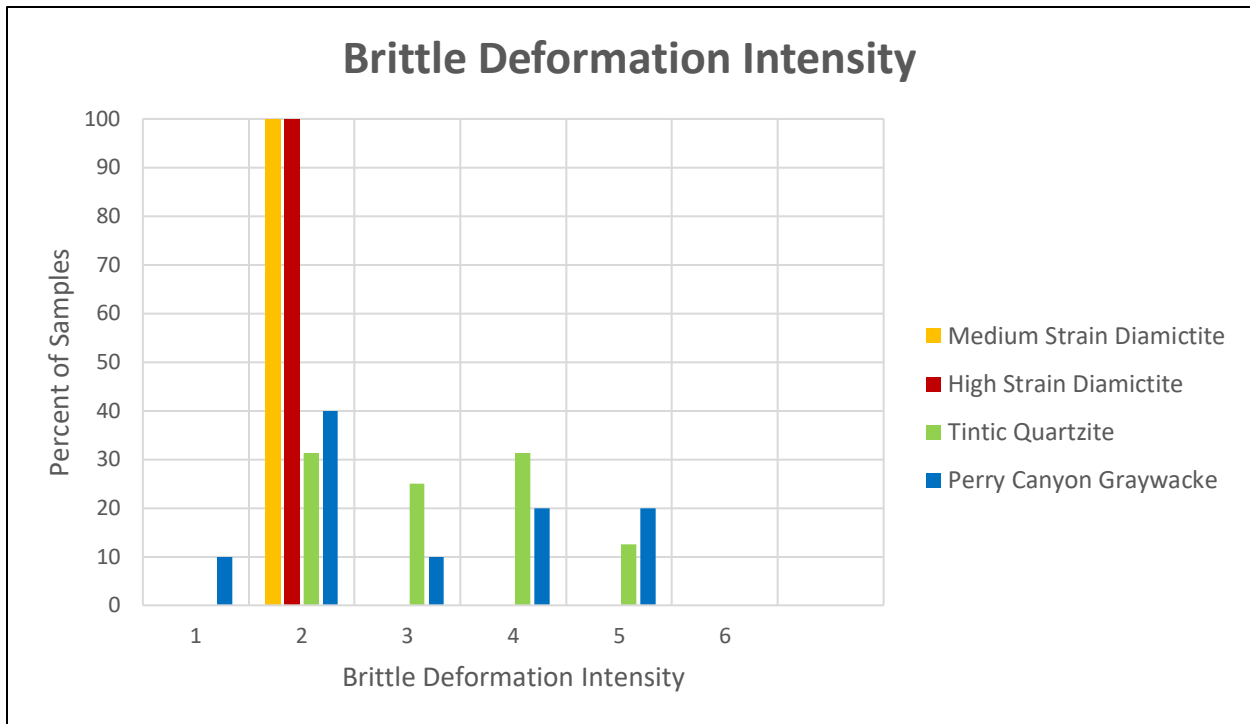
Figure 14. Graphs shows the frequency of microstructures related to brittle deformation for each lithology. Values for intensities are: 1 (very low), 2 (low), 3 (low-moderate), 4 (moderate), 5 (moderate-high), and 6 (high).
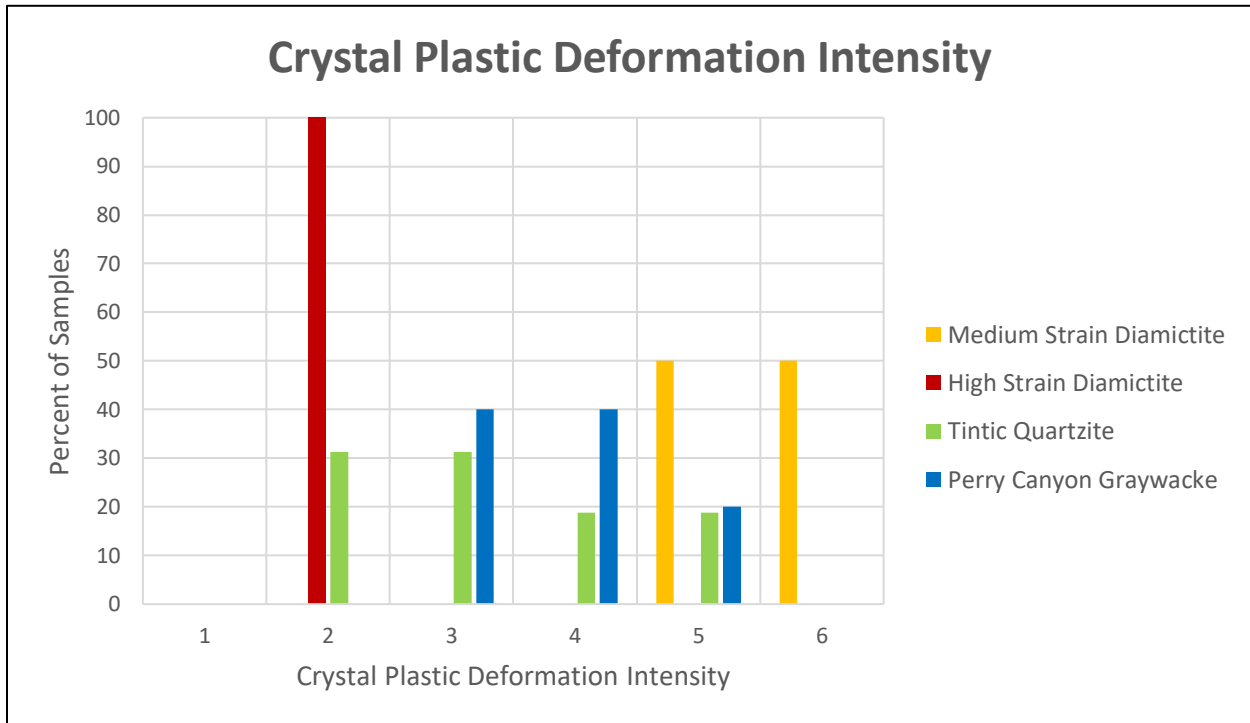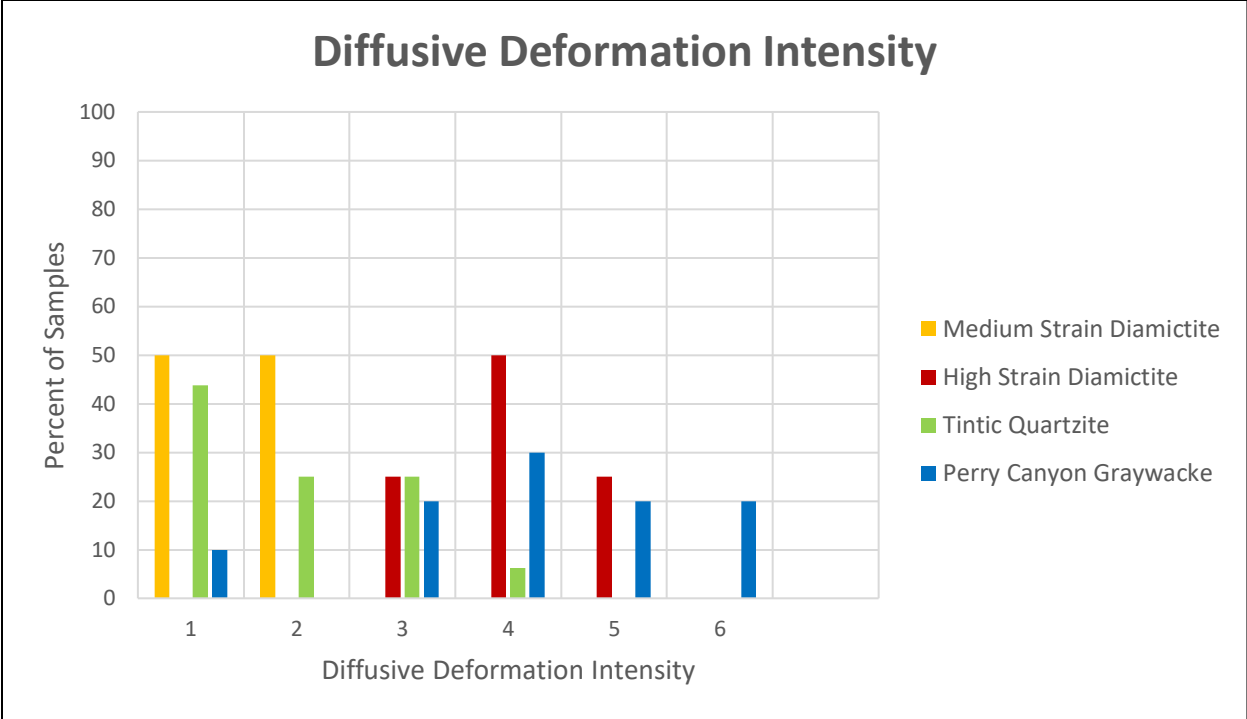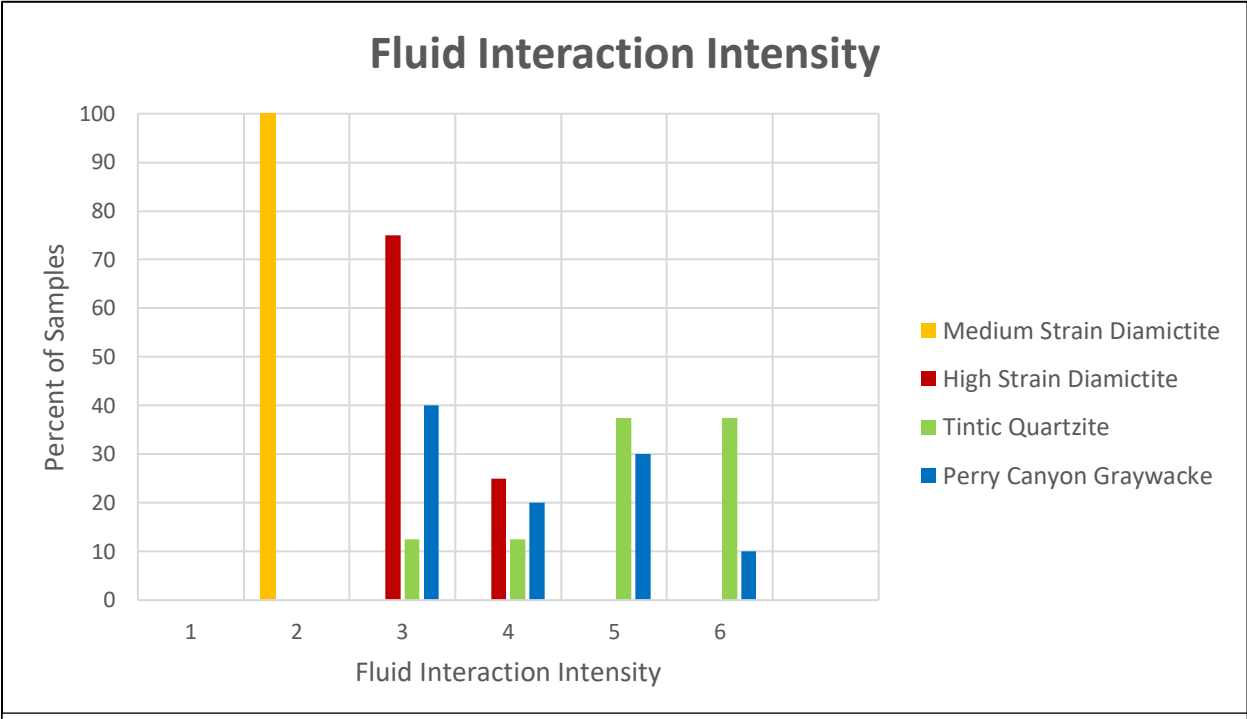

Figure 15. Graph shows the frequency of microstructures related to crystal plastic deformation for each lithology. Values for intensities are: 1 (very low), 2 (low), 3 (low-moderate), 4 (moderate), 5 (moderate-high), and 6 (high).

Figure 16. Graph shows the frequency of microstructures related to diffusive deformation for each lithology. Values for intensities are: 1 (very low), 2 (low), 3 (low-moderate), 4 (moderate), 5 (moderate-high), and 6 (high).

Figure 17. Graph shows the frequency of microstructures related to fluid interaction for each lithology. Values for intensities are: 1 (very low), 2 (low), 3 (low-moderate), 4 (moderate), 5 (moderate-high), and 6 (high).

5.111 Mineral Fork Diamictite

In general, all diamictite samples, regardless of strain, have very few microstructures indicating brittle deformation and a low to moderate quantity of microstructures suggesting fluid interaction. The intensity of crystal plastic and diffusive microstructures varies with strain. Medium strain samples are dominated by crystal plastic microstructures while high strain samples are dominated by diffusive microstructures.

5.1111 Medium Strain Samples

The four medium strain diamictite samples (AI1901A, B, C, D) are dominated by crystal plastic microstructures as indicated by the most prevalent microstructure, quartz undulose extinction observed in moderate abundance. AI1901A and B also have some rare quartz lamellae. Quartz subgrain formation is likely the primary recovery mechanism, and the frequency of subgrains ranges from moderate to high, which is more than any other Willard sample. AI1901D also has a very low frequency of quartz triple junctions, indicating that dynamic recrystallization was a secondary recovery mechanism (Fig. 18).

Low quantities of brittle microstructures, intragranular fractures and microveins, are observed in all samples, but are not abundant. Diffusive microstructures are rare. Sample AI1901A has rare top-to-the-east strain shadows and selvage seams, but the other three medium strain samples have no indication of deformation by diffusion (Fig. 18).

These samples all have a low to low-moderate amount of fluid-related microstructures. Fluid inclusion planes are present in three samples at a low frequency. The low frequency of selvage seams in AI1901A and the low frequency of microfractures and microveins in all four samples is also indicative of fluid-interaction (Fig. 18).
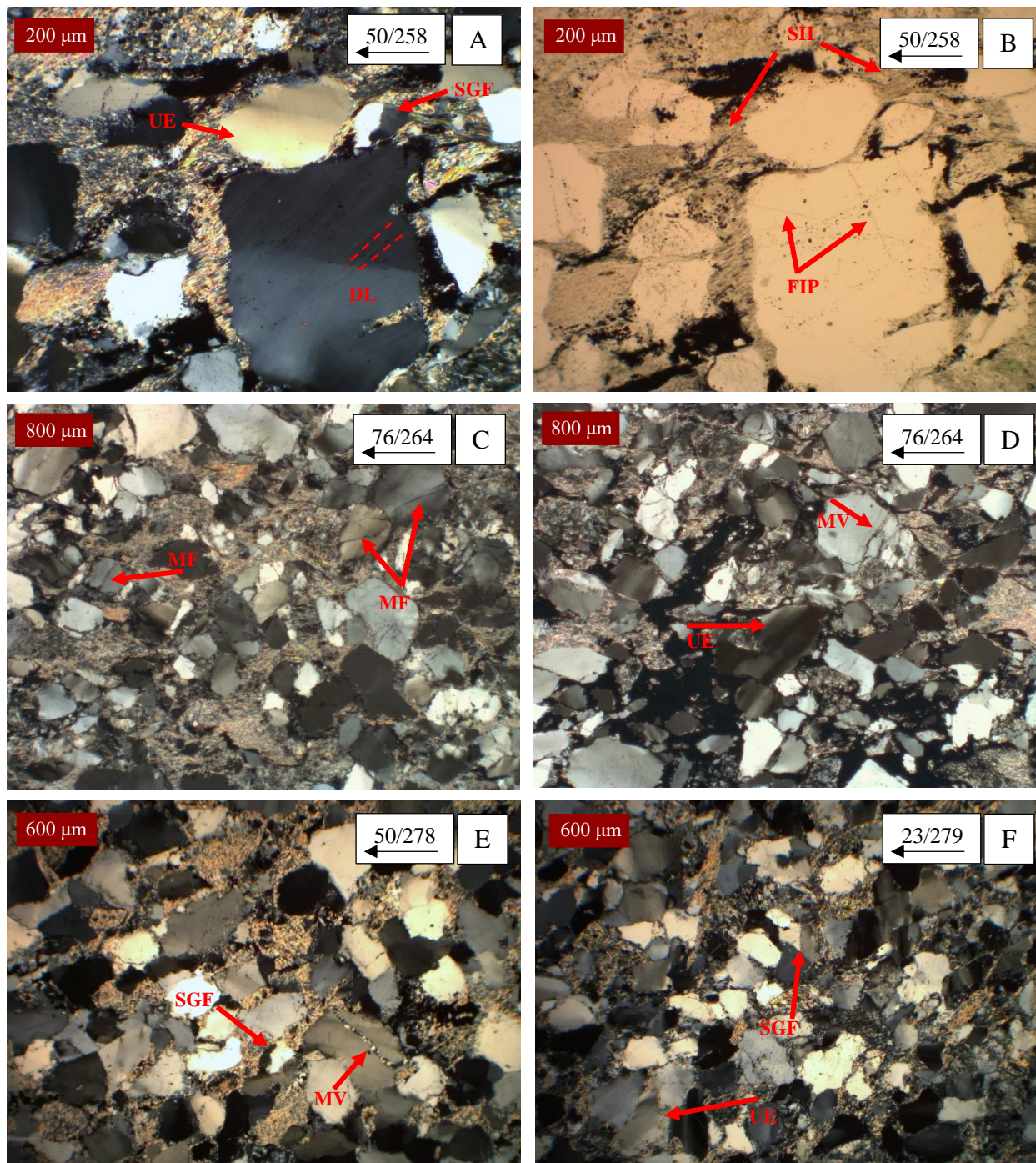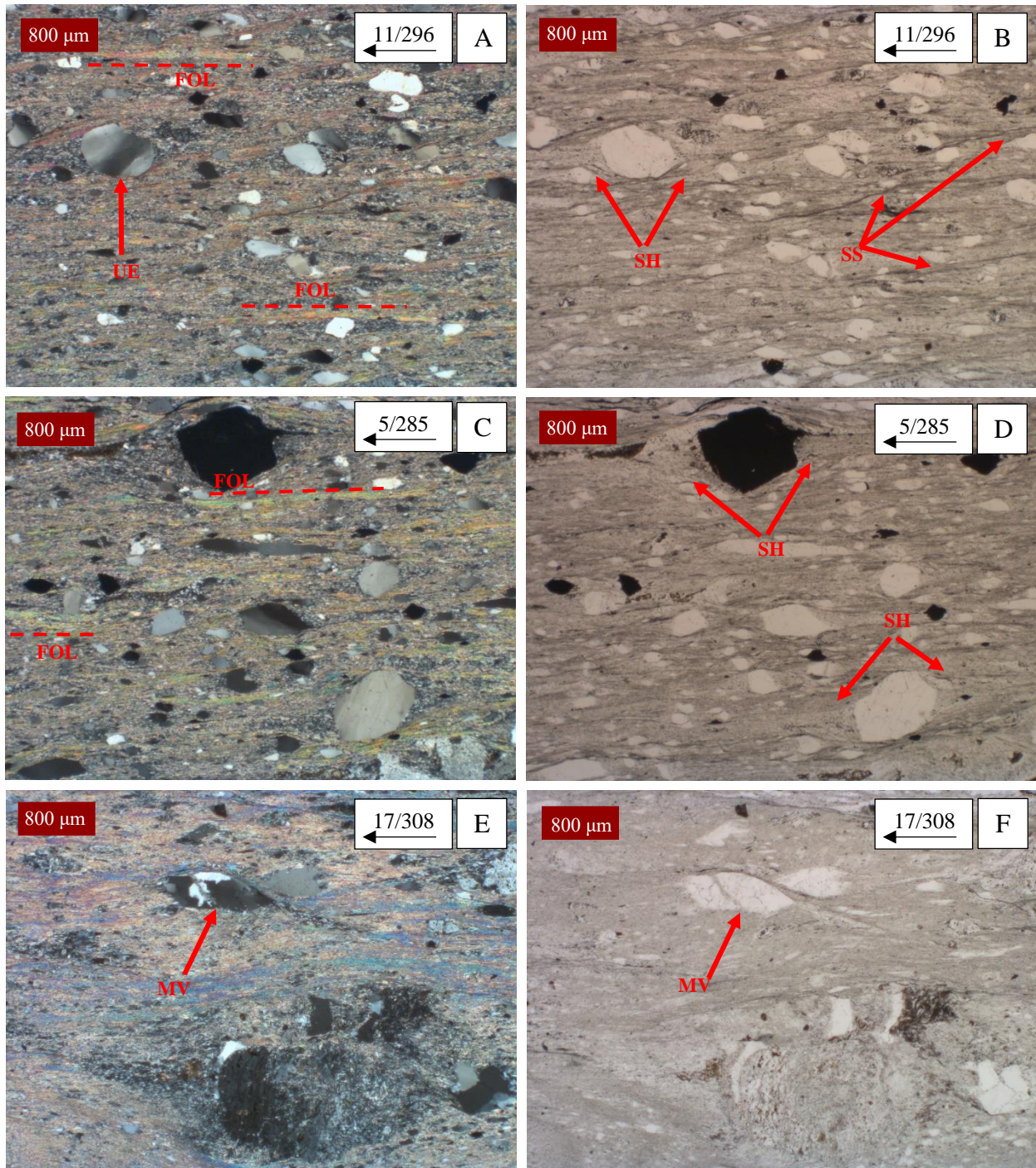
Figure 18. Photomicrographs of microstructures in medium strain diamictite samples (XZ planes with orientation of X directions indicated) showing **(A)** undulose extinction (UE), subgrain formation (SGF), and deformation lamellae (DF) in quartz grains from AI1901A, **(B)** fluid inclusion planes (FIP) and a strain shadow (SH) in quartz grains from AI1901A, **(C)** microfractures (MF) in quartz grains from AI1901B, **(D)** undulose extinction (UE) and a microvein (MV) in quartz grains from AI1901B, **(E)** subgrain formation (SGF) and a microvein (MV) in quartz grains from AI1901C, and **(F)** undulose extinction (UE) and subgrain formation (SGF) in quartz grains from AI1901D.

The four high strain diamictite samples, AI1902A/B and AI1903A/B, are dominated by the presence of diffusion-related microstructures. Both AI1903 samples have low-moderate selvage seams and moderate-high asymmetric (top-to-the-east) and symmetric strain shadows. AI1902A has low-moderate selvage seams and low asymmetric (top-to-the-east) strain shadows, while AI1902B has moderate-high selvage seams and moderate asymmetric (top-to-the-east) and symmetric strain shadows. Both AI1902 samples also have a low frequency of sutured grain boundaries (Fig. 19).

Dislocation-related microstructures are secondary. All four samples have a high frequency of mica foliation and quartz undulose extinction is generally low-moderate. Only sample AI1902B shows minor quartz lamellae. AI1903A and AI1902A have a low frequency of the recovery mechanism quartz subgrain formation. Brittle microstructures are minor. All four samples have low intragranular fractures and microveins (Fig. 19).

Generally, the high strain samples have a low-moderate amount of fluid-associated microstructures related to the low abundance of microfractures and microveins and the generally low-moderate abundance of selvage seams (Fig. 19).

Figure 19. Photomicrographs of microstructures in high strain diamictite samples (XZ planes with orientation of X directions indicated) showing **(A)** undulose extinction (UE) in a quartz grain and mica foliation (FOL) from AI1903B, **(B)** a strain shadow (SH) in a quartz grain and selvage seams (SS) from AI1903B, **(C)** mica foliation (FOL) from AI1903A, **(D)** strrain shadows (SH) in magnetite and quartz grains from AI1903A, **(E)** microvein (MV) in a quartz grain from AI1902A, **(F)** microvein (MV) in a quartz grain from AI1902A. A, B, and E are in XPL. B, D, and F are in PPL.

5.112 Tintic Quartzite

All Tintic quartzite samples have similar microstructural characteristics. Microstructures related to deformation by crystal plasticity dominate; brittle microstructures have a prominent, but secondary role; and diffusive microstructures are minor.

While crystal plasticity dominates in all samples, the degree of crystal plasticity varies. For example, samples from AI1904/05 have slightly more crystal plastic microstructures than AI1906/07. This is evidenced by generally moderate quartz lamellae and low to low-moderate plagioclase lamellae in the AI1904/05 samples compared to a generally low abundance of quartz lamellae and low plagioclase lamellae in samples from AI1906/07. There is also more quartz subgrain formation in the samples from AI1904/05 (low frequency) compared to those from AI1906/07 (very low frequency) (Fig. 20).

Samples from AI1904/05 also have slightly more brittle deformation microstructures than AI1906/07. This is evidenced by a higher abundance of microfractures and microveins in each sample. For example, AI1904/05 samples only have three samples that do not have intergranular microfractures and six of the AI1906/07 samples do not have intergranular microfractures. Similarly, AI1904/05 samples are characterized by low-moderate intragranular fractures and microveins and AI1906/07 samples are characterized by low intragranular fractures and microveins (Fig. 20).

Samples from AI1904/05 have slightly fewer microstructures related to deformation by diffusion compared to AI1906/07. No samples had selvage seams, except for AI1904B, which had a low frequency, and AI1906A, which had a moderate frequency. Strain shadows are only

present in three of eight AI1904/05 samples at a generally low frequency. Meanwhile, symmetric strain shadows are present in five of eight AI1906/07 samples at a generally low to low-moderate frequency (Fig. 20). All Tintic samples have a moderate frequency of microstructures related to fluid-interaction. Generally, there is a low-moderate frequency of fluid inclusion planes, alteration/sericitization of feldspar, and microfractures, as well as a low frequency of microveins (Fig. 20).
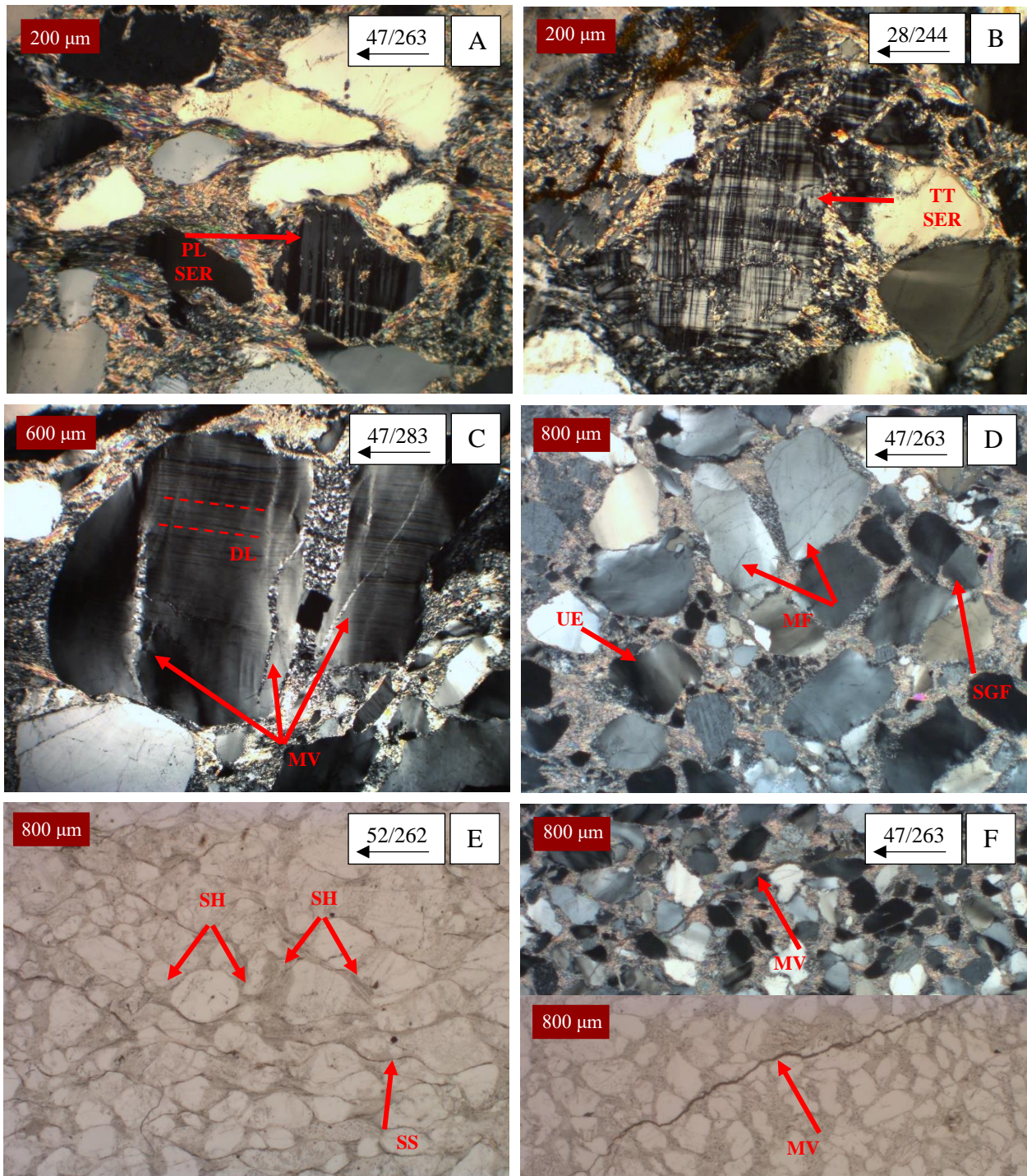
Figure 20. Photomicrographs of microstructures in Tintic quartzite samples (XZ planes with orientation of X directions indicated) showing **(A)** plagioclase lamellae (PL) and sericitization (SER) from AI1904C, **(B)** tartan twinning (TT) and sericitization (SER) from AI1906C, **(C)** deformation lamellae (DL) and microveins (MV) in quartz from AI1905A, **(D)** undulose extinction (UE), microfractures (MF), and subgrain formation (SGF) in quartz grains from AI1904C, **(E)** strain shadows (SH) in quartz grains and selvage seams (SS) from AI1906A, and **(F)** an intergranular microvein (MV) in AI1904C. A, B, C, and D are in XPL. E is in PPL. F shows both XPL and PPL.

45

5.113 Perry Canyon Graywacke

Samples from the Perry Canyon graywacke are generally dominated by either diffusion or crystal plasticity with lesser amounts of brittle deformation; however, a fair amount of variation exists in the amounts of each deformation style and quantity of interpreted fluid-interaction across the different varieties of graywacke.

5.1131 Massive and Thinly Bedded Graywacke

The massive (PV1901A-D) and thinly bedded (PV1901E-G) samples are dominated by both diffusive and crystal plastic microstructures. All samples are characterized by having generally moderate to moderate-high frequency of selvage seams and moderate frequency of symmetric strain shadows. All samples also have numerous (high frequency) quartz grains with undulose extinction and generally low degrees of mica foliation. The massive samples have slightly more quartz lamellae (low-moderate) compared to the thinly bedded samples (low). The massive samples also show a higher frequency of recovery mechanisms, with a low amount of quartz subgrain formation compared to no quartz subgrain formation in the thinly bedded samples. (Fig. 21).

In both the massive and thinly bedded samples, brittle microstructures are secondary; however, they are more prevalent in the massive samples. On average, the massive samples have low-moderate intergranular fractures, low intragranular fractures, and moderate microveins. In comparison, the thinly bedded samples have low intergranular fractures, intragranular fractures, and microveins. Very low quantities of microboudins are present in PV1901E and G (Fig. 21).

There is more evidence for fluid interaction in the massive samples. As mentioned above, there is a higher frequency of microfractures and microveins in the massive samples.

Additionally, PV1901A-C have a low frequency of fluid inclusion planes, while no thinly bedded samples do. Overall, the massive Perry Canyon graywackes have moderate evidence for fluid-interaction and the thinly bedded Perry Canyon graywackes have low-moderate evidence for fluid-interaction (Fig. 21).
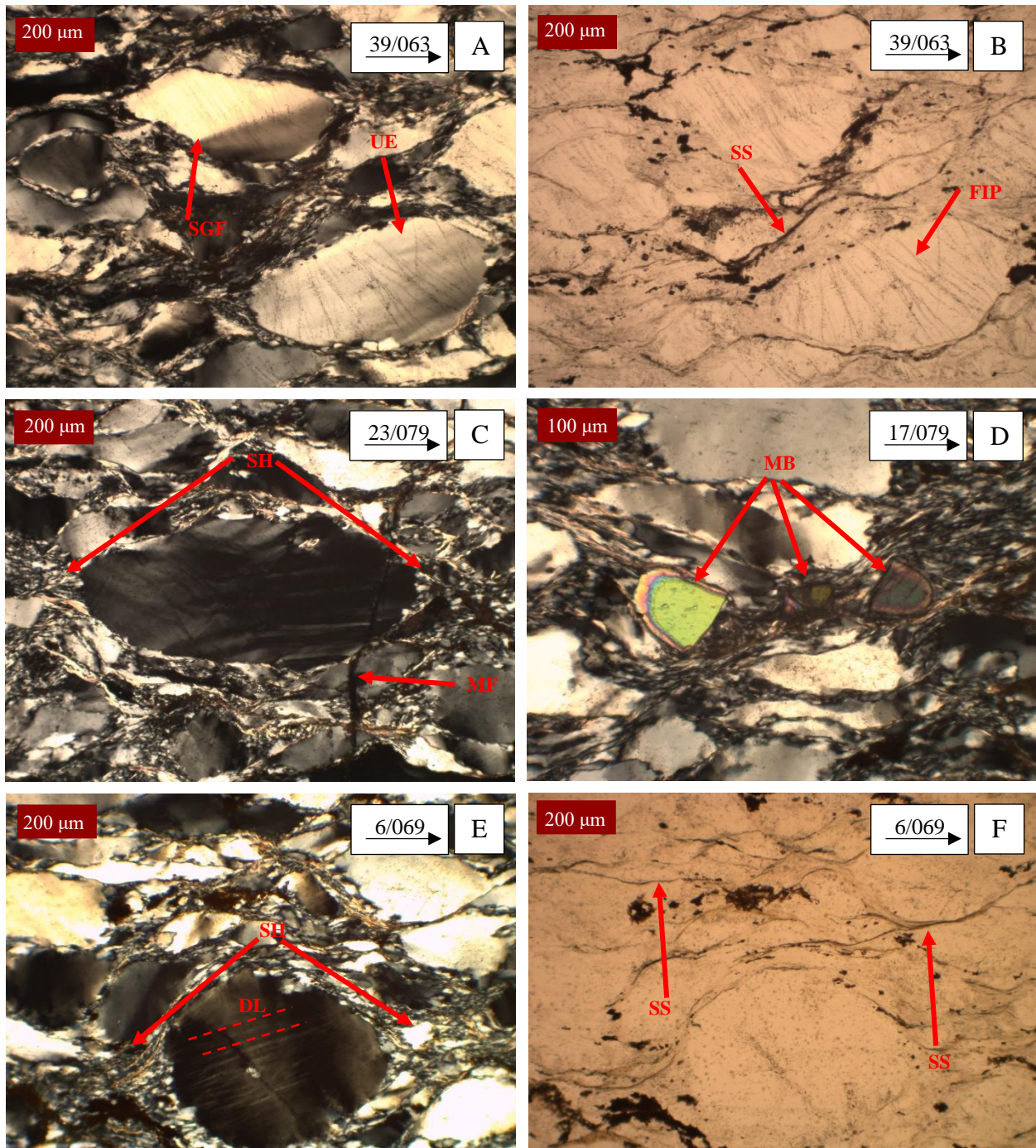
Figure 21. Photomicrographs of microstructures in massive and thinly bedded Perry Canyon graywacke samples (XZ planes with orientation of X directions indicated) showing **(A)** subgrain formation (SGF) and undulose extinction (UE) in quartz grains from PV1901B, **(B)** fluid inclusion planes (FIP) in quartz and selvage seams from PV1901B, **(C)** a strain shadow (SH) and microfracture (MF) from PV1901D, **(D)** a microboudined (MB) zircon from PV19901E, **(E)** a strain shadow (SH) and deformation lamellae (DL) from PV1901G, and **(F)** selvage seams from PV1901G. A, C, D, and E are in XPL. B and F are in PPL.

5.1132 Micaceous, Shaly Graywacke

The dirty/shaly samples, PV1901H and PV1901I, have a very high frequency of microstructures related to diffusion. Both samples have a high frequency of symmetric strain shadows and selvage seams. Deformation by crystal plasticity has a significant, but lesser role. Both samples have low abundances of quartz lamellae and moderate-high mica foliation. PV1901H has moderate-high amounts of quartz undulose extinction and PV1901I has high amounts of quartz undulose extinction. Both samples also have a low frequency of quartz subgrain formation. Microstructures related to brittle deformation are largely absent. Only PV1901H has very low microboudins and PV1901I has low intragranular fractures (Fig. 22).

The frequency of microstructures related to fluid-interaction is very low. The only microstructures present are selvage seams in both samples and the low microfractures in PV1901I.

5.1133 Site PV1902 Graywacke

PV1902A is the only Perry Canyon sample from the second sampling location. This sample is dominated by microstructures related to crystal plasticity. It has a low abundance of quartz lamellae, quartz subgrain formation, and plagioclase lamellae, and a moderate-high abundance of quartz undulose extinction. Evidence for brittle deformation is low, with only a low frequency of intragranular microfractures present. There are no microstructures related to diffusion. The frequency of microstructures related to fluid-interaction is also low. There is low-moderate alteration/sericitization in feldspar and a small number of microfractures (Fig. 22E,F).
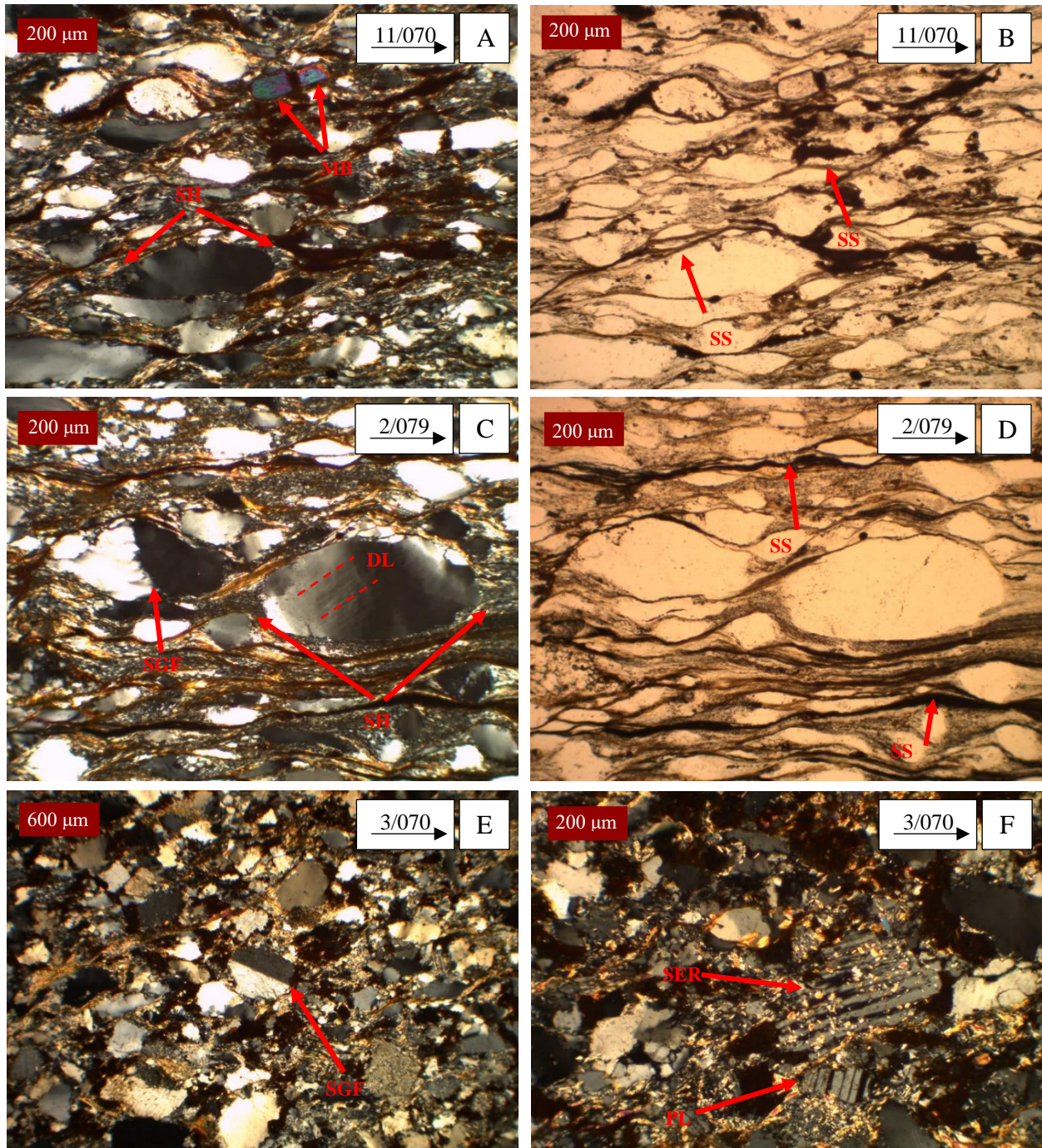
Figure 22. Photomicrographs of microstructures in site PV1901 dirty/shaly samples and site PV1902A Perry Canyon graywacke samples (XZ planes with orientation of X directions indicated) showing **(A)** a strain shadow (SH) in a quartz grain and a microboudined (MB) zircon from PV1901H, **(B)** selvage seams from PV1901H, **(C)** a strain shadow (SH), deformation lamellae (DL) and subgrain formation (SGF) in quartz grains from PV1901I, **(D)** selvage seams from PV1901I, **(E)** quartz subgrain formation (SGF) from PV1902A, and **(F)** plagioclase lamellae (PL) and sericitization (SER) from PV1902A. A, C, E, and F are in XPL. B and D are PPL.

50

5.2 Discussion

One of the main goals of this study is to compare the intensity of fluid interaction in each sample to the respective dominant deformation mechanism. However, this comparison is not entirely straightforward as there are many other variables to consider as well, including grain size, mineralogy, and proximity to the fault. Below, the relationships between each of these variables is explored.

5.21 Dominant Deformation Mechanism

Each sample can be characterized by its intensity of brittle, crystal plastic, and diffusive deformation. All samples are dominated by crystal plasticity (footwall samples of medium strained diamictite and Tintic quartzite) or a combination of crystal plasticity and diffusive deformation (footwall samples of high strained diamictite and hanging wall graywacke, which has relatively low strain). The first relationship to explore is between these mechanisms, determining whether the intensity of each deformation mechanism is related to the intensity of the other deformation mechanisms (Fig. 23). The brittle and diffusive deformation mechanisms are negatively correlated, as are crystal plastic and diffusive deformation mechanisms. The intensity of brittle and crystal plastic deformation appear to be unrelated

5.211 Deformation Mechanism vs. Fluid Interaction

Fluid interaction was gauged by the quantities of microstructures directly related to fluid (fluid inclusion planes and sericitization). Diffusion-related microstructures (solution seams and strain shadows) were also included because they are most likely to form if a fluid phase is present. Microstructures such as microfractures were not included because they can form with or without the presence of fluid.

There is a positive correlation between the intensity of fluid interaction and the intensity of both brittle deformation and diffusion. However, there is no relationship between fluid interaction and the intensity of crystal plasticity in each sample (Fig. 24). Further examination reveals that whether fluids enhance diffusion or brittle deformation is at least partly influenced by grain size (Fig. 25). Samples that have high brittle deformation generally have larger grain sizes, while samples that have high intensities of diffusion are finer-grained samples.

To summarize, crystal plasticity occurs with or without the presence of fluid. When fluid enters the system, in smaller grain size samples, the dominant deformation mechanism switches to diffusion or becomes a combination of crystal plasticity and diffusion. In larger-grained samples, the dominant deformation mechanism remains crystal plasticity, but intermittent embrittlement is present. This embrittlement is likely due to increased fluid pressure.

5.212 Deformation Mechanism vs. Grain Size

Grain size and crystal plasticity and diffusion appear to be related. Grain size and crystal plastic deformation are positively correlated, while. grain size and deformation by diffusion are negatively correlated. There appears to be no relationship between brittle deformation and grain size (Fig. 26).

5.213 Deformation Mechanism vs. Mineralogy

The intensities of each deformation mechanism are all weakly related to the mineralogy of each sample. Quartz content is directly related to the intensity of brittle deformation and crystal plasticity in the samples. The percentage of quartz and the intensity of diffusion are negatively correlated (Fig. 27).

5.214 Deformation Mechanism vs. Proximity to Fault

Several relationships are observed between the dominant deformation mechanisms present in the footwall samples and their respective distance to the fault. The hanging wall samples could not be analyzed in this way because the only samples available were all relatively close together so their distances from the fault were similar. No relationship was observed between brittle deformation and proximity to the fault for Mineral Fork diamictite samples; however, in the Tintic quartzite increased amounts of brittle deformation was found in samples further from the fault. Similarly, increased distance from the fault is related to increased amounts of crystal plasticity in both the Mineral Fork and Tintic samples. Contrarily, increased distance from the fault is related to decreased deformation by diffusion in the Mineral Fork and Tintic samples (Fig. 28). In summary, samples that are closer to the fault have more diffusion and samples that are further from the fault have more crystal plasticity and brittle deformation.

5.22 Fluid Interaction vs. Grain Size, Mineralogy, and Proximity to Fault

Fluid interaction is most strongly related to fault proximity. As the distance to the fault increases, fluid intensity decreases (Fig. 29).

Fluid intensity and quartz concentration have a more complex relationship. Within each individual rock type, increasing quartz is weakly related to less fluid interaction. However, when comparing across all samples, there is a weak positive correlation (Fig. 29).

Finally, no correlation is observed between fluid intensity and grain size (Fig. 29).

5.23 Overall Summary

It appears that the amount of fluid interaction present in a sample is most closely related to its proximity to the fault. The closer to the fault a sample is, the more fluid interaction there will be. The effects that fluid has on deformation is closely related to grain size. Fluid drives diffusion

in samples with a smaller grain size and enhances brittle deformation in larger grain size samples. However, fluid is not the only factor that effects dominant deformation mechanisms. There are also relationships between deformation mechanisms and quartz content, fault proximity, and, to a lesser extent, grain size.

Fig. 23
Graphs show the intensity of microstruct-ures related to brittle deformation compared to diffusive deformation, crystal plastic deformation compared to diffusive deformation, and brittle deformation compared to crystal plastic deformation. Values for intensities are: 1 (very low), 2 (low), 3 (low-moderate), 4 (moderate), 5 (moderate-high), and 6 (high).

55
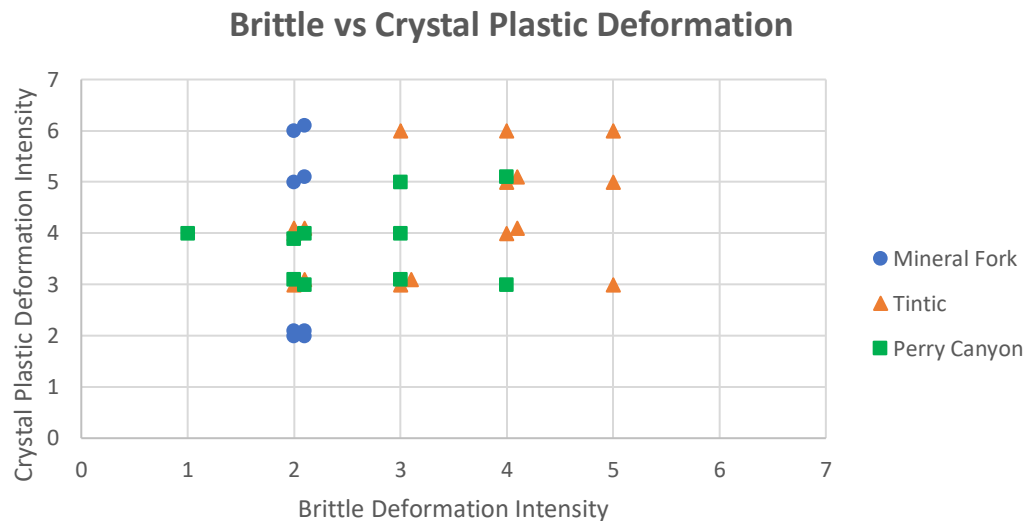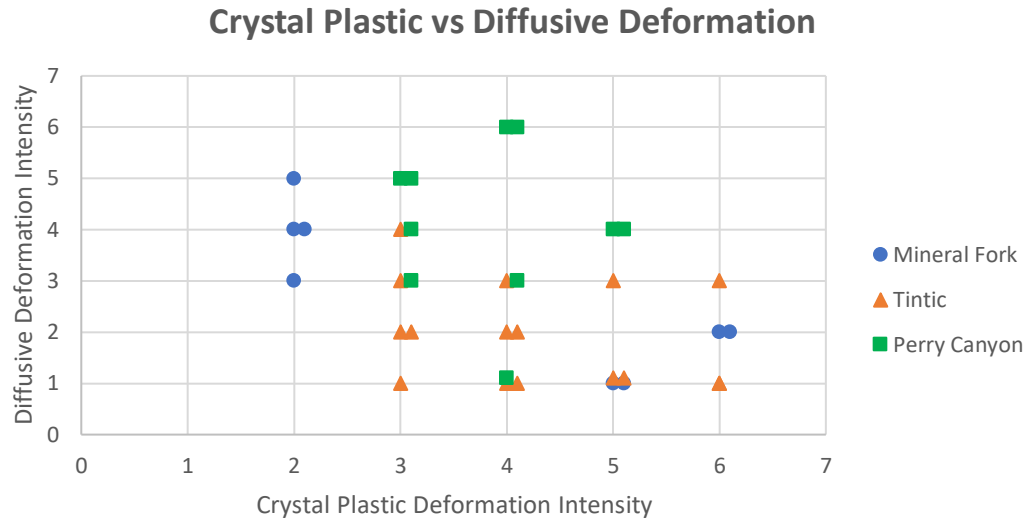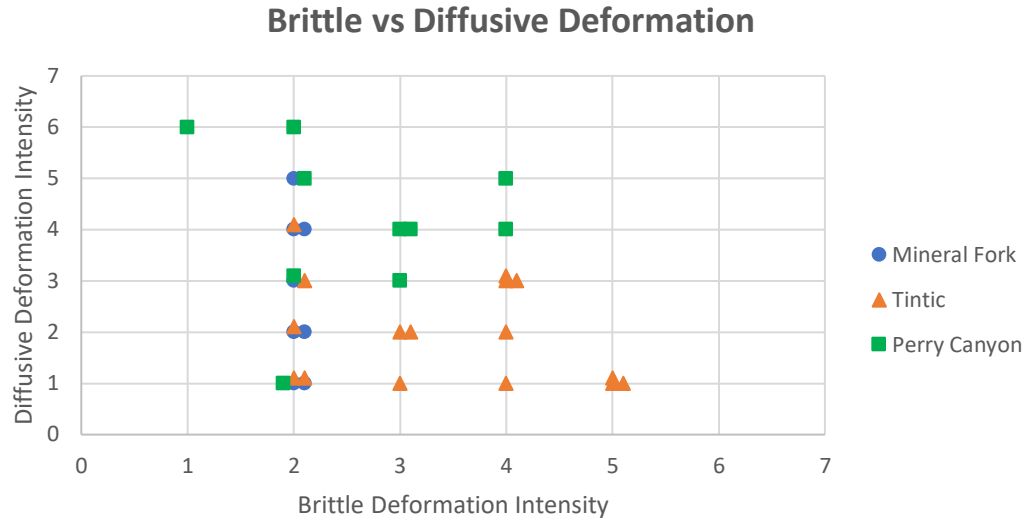
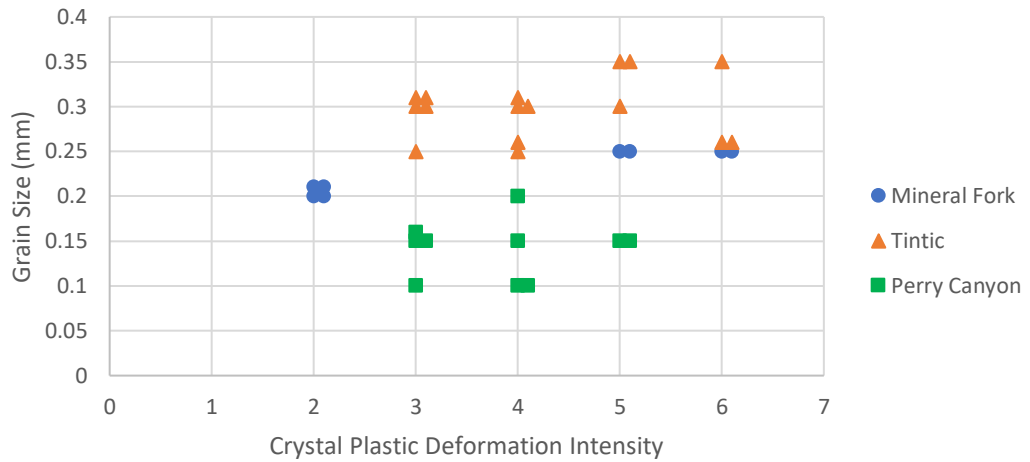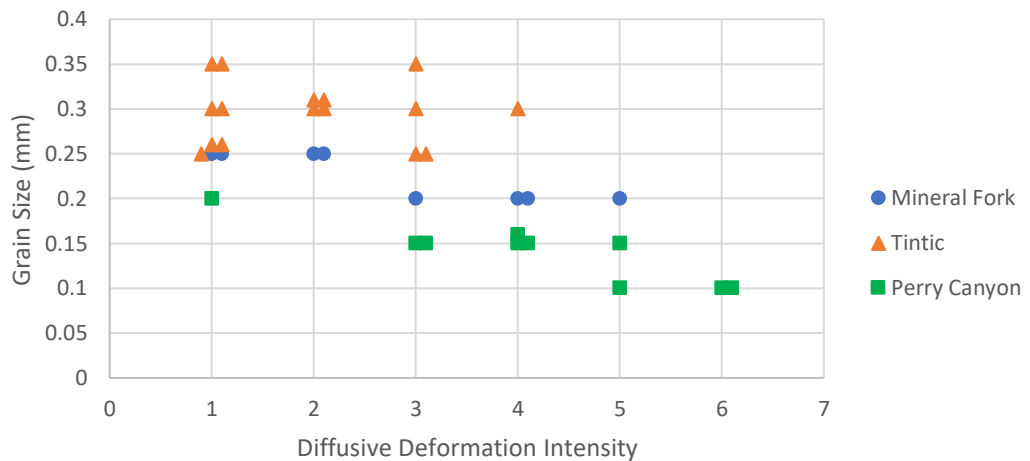**Fig. 24** Graphs show the intensity of fluid interaction compared to the intensity of microstructures related to brittle, crystal plastic, and diffusive deformation. Values for intensities are: 1 (very low), 2 (low), 3 (low-moderate), 4 (moderate), 5 (moderate-high), and 6 (high).

56
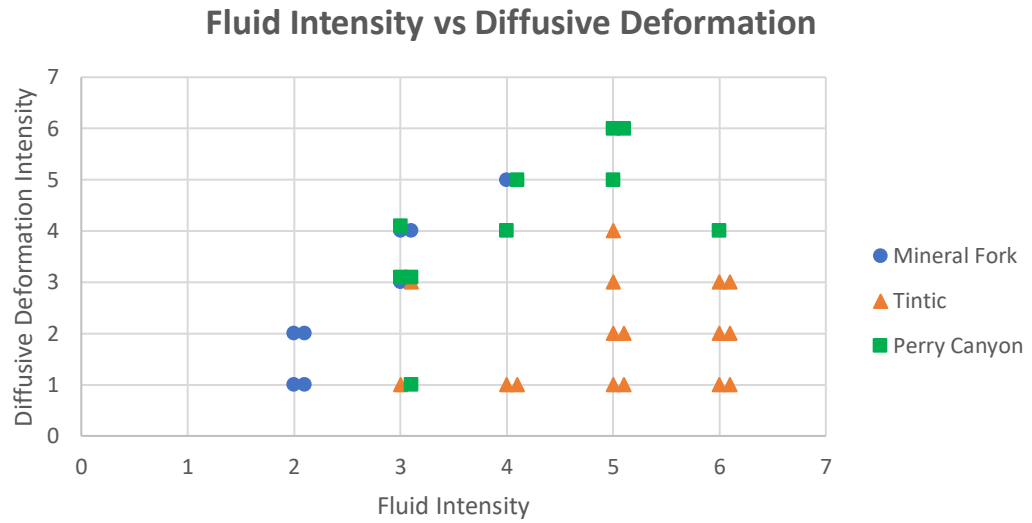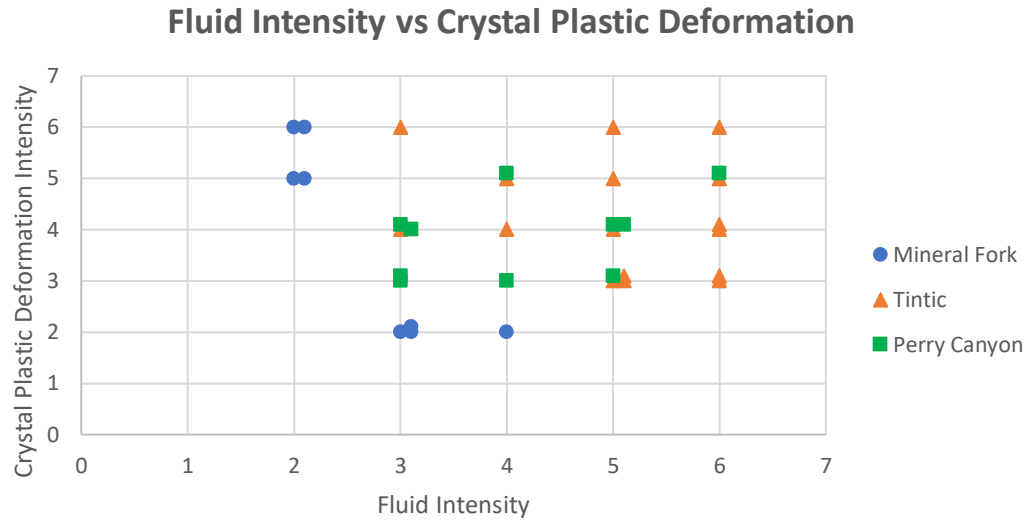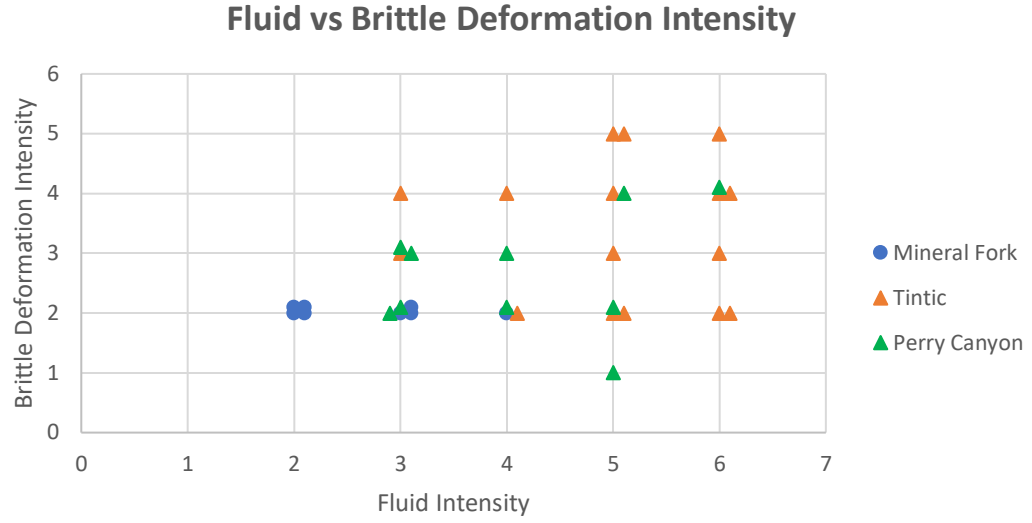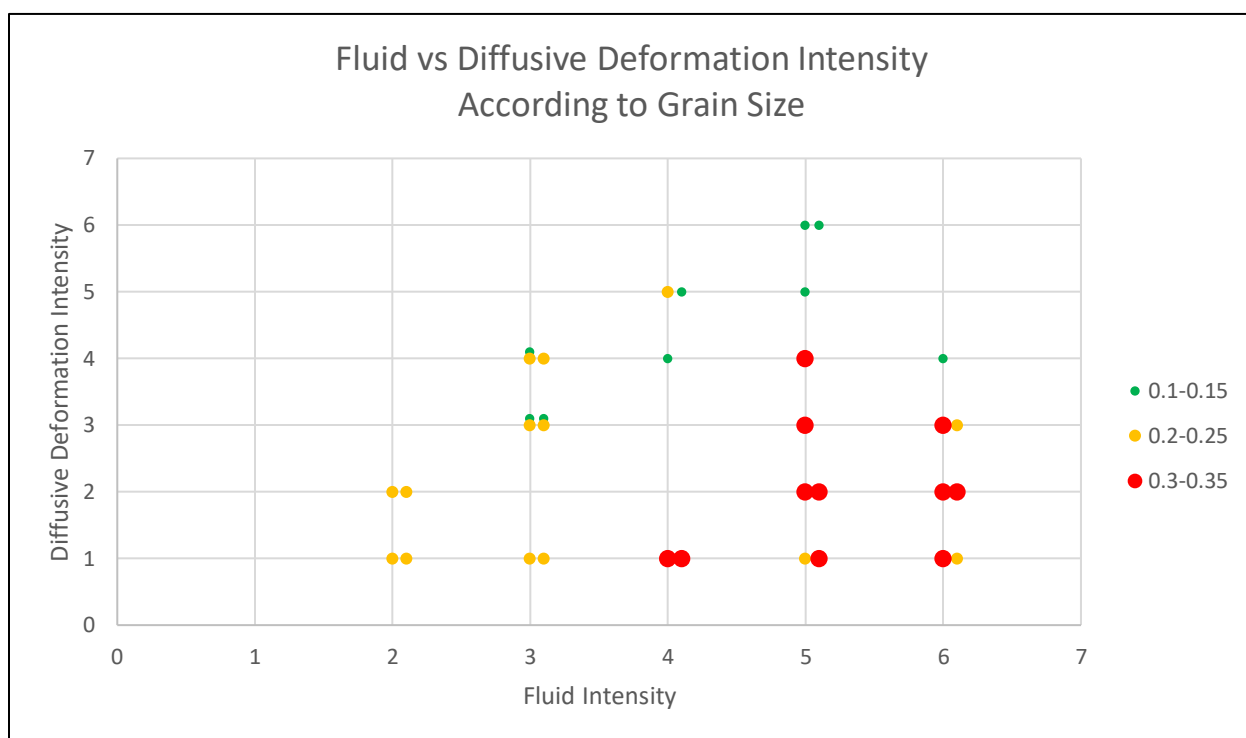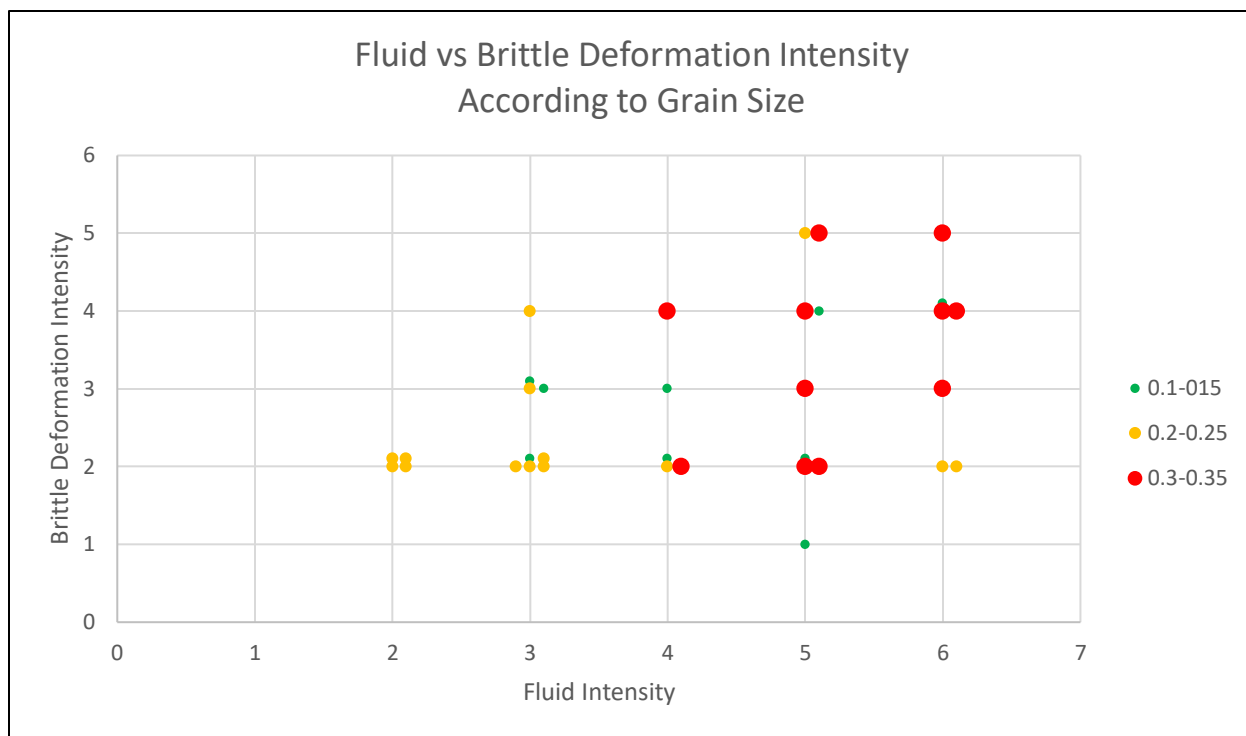
Figure 25. Graphs show the intensity of fluid interaction compared to the intensity of microstructures related to brittle and diffusive deformation. Points are displayed according to their grain size. Values for intensities are: 1 (very low), 2 (low), 3 (low-moderate), 4 (moderate), 5 (moderate-high), and 6 (high).

57

Fig. 26
Graphs show the grain size of each sample compared to the intensity of microstructures related to brittle, crystal plastic, and diffusive deformation. Values for intensities are: 1 (very low), 2 (low), 3 (low-moderate), 4 (moderate), 5 (moderate-high), and 6 (high).
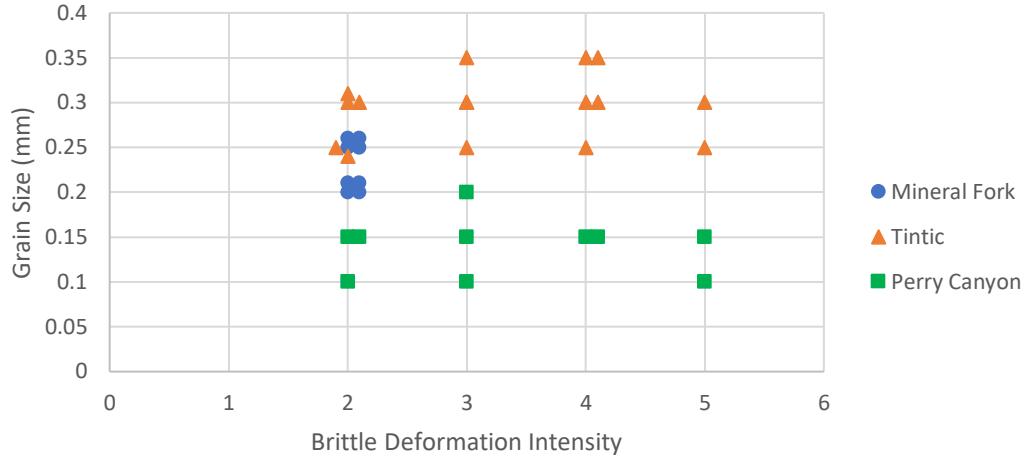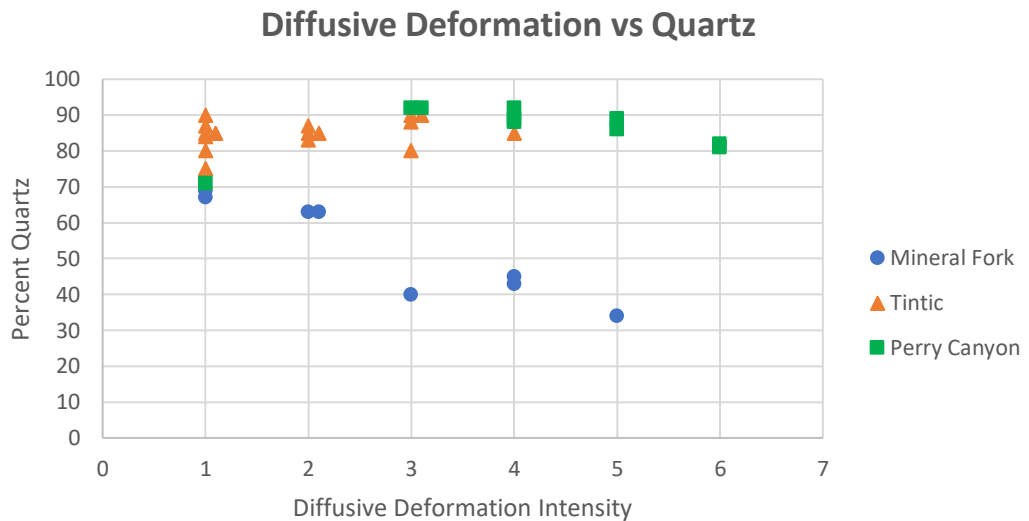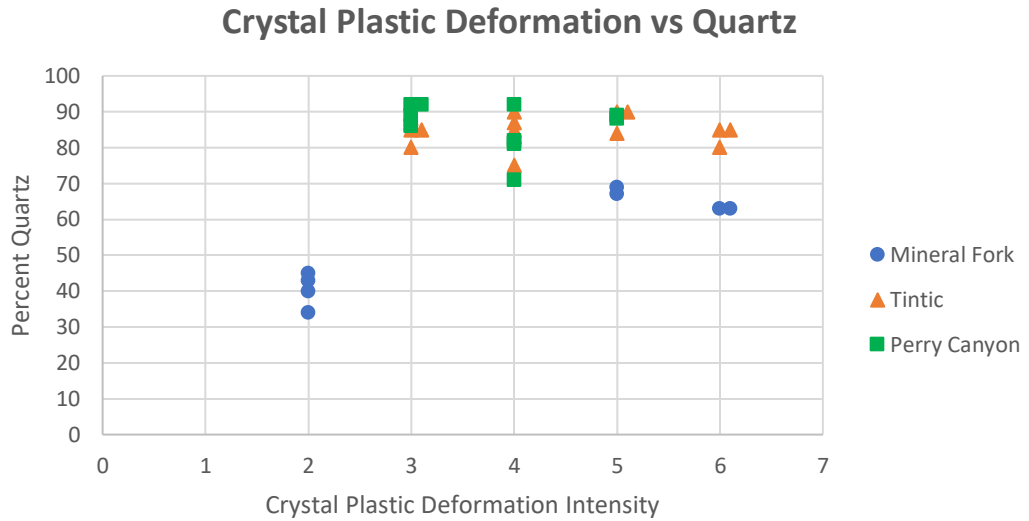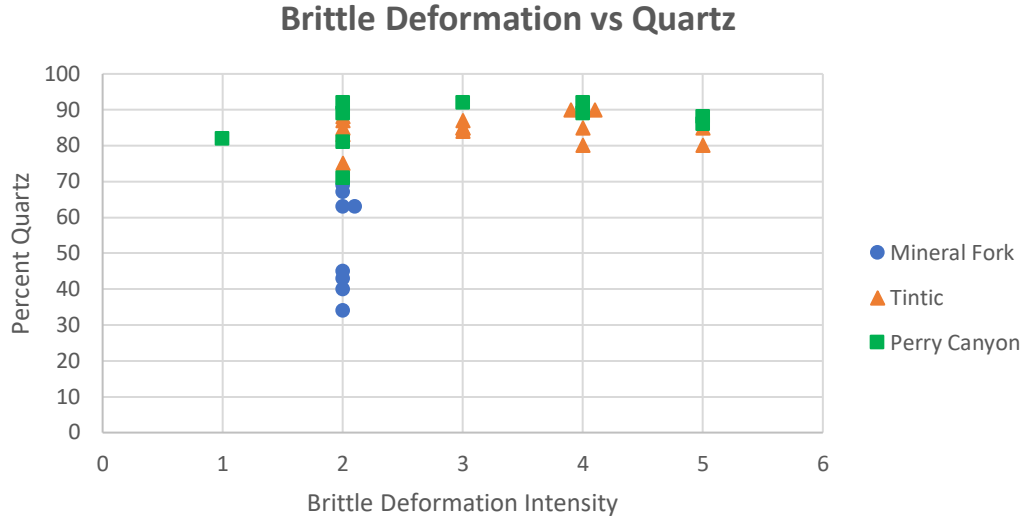
Fig. 27
Graphs show the percent of quartz in each sample compared to the intensity of microstructures related to brittle, crystal plastic, and diffusive deformation. Values for intensities are: 1 (very low), 2 (low), 3 (low-moderate), 4 (moderate), 5 (moderate-high), and 6 (high).

59

Fig. 28
Graphs show
the intensity
of
microstruct-
ures related
to brittle,
crystal
plastic, and
diffusive
deformation
compared to
the distance
of samples to
the fault –
FW
(footwall),
MF (Mineral
Fork
diamictite), T
(Tintic
quartzite).
Values for
intensities
are: 1 (very
low), 2 (low),
3 (low-
moderate), 4
(moderate), 5
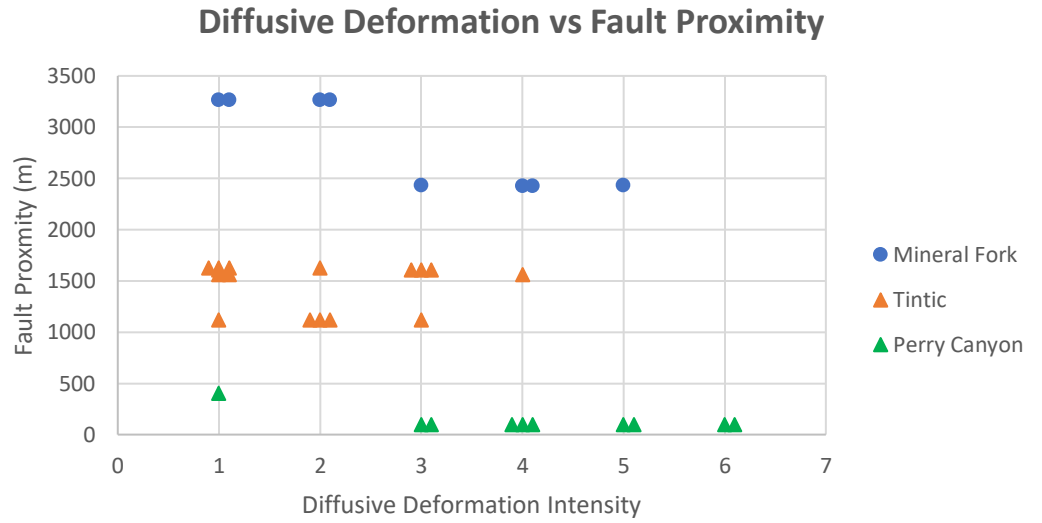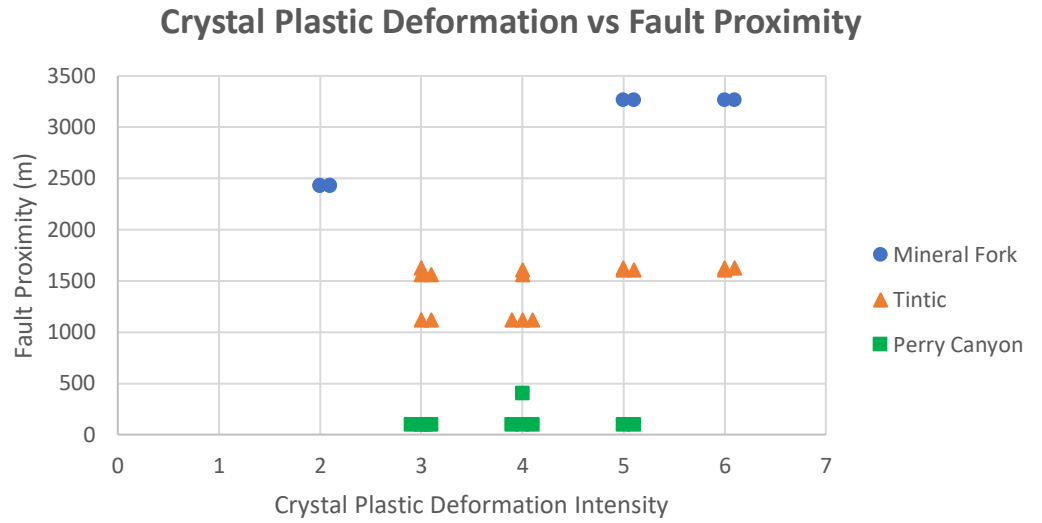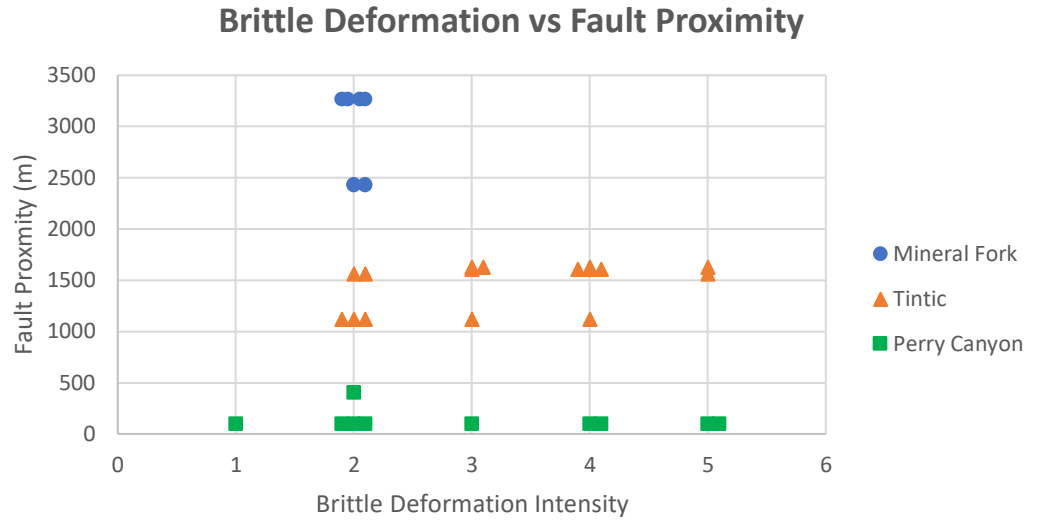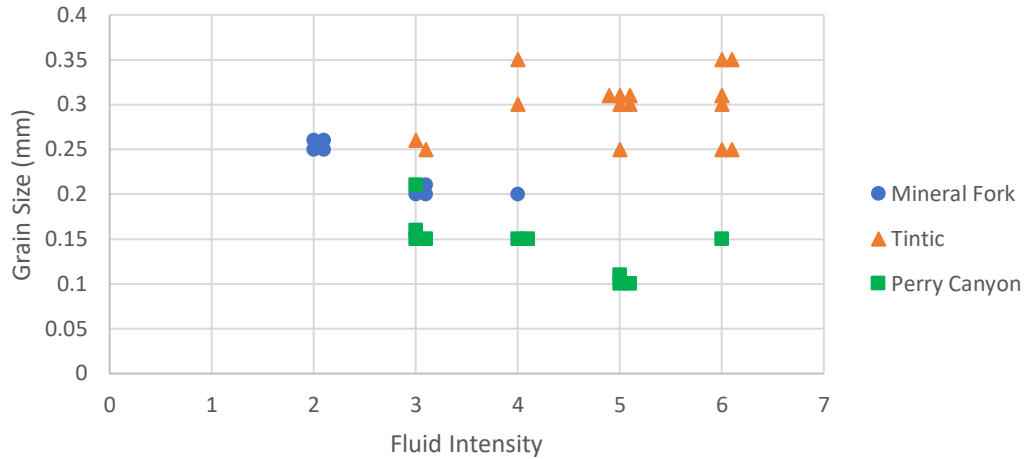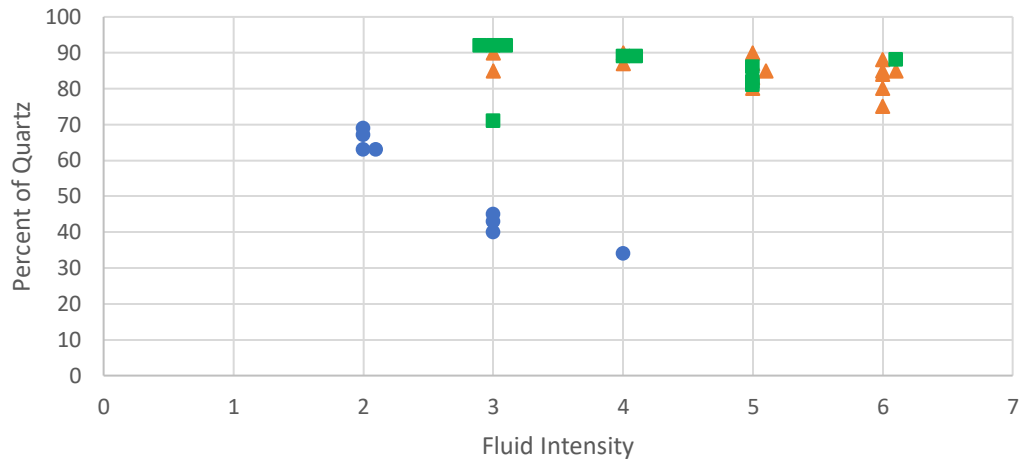(moderate-
high), and 6
(high).

60

Fig. 29
Graphs show
the intensity
of fluid
interaction
compared to
grain size,
the percent of
quartz, and
the distance
of samples to
the fault –
FW
(footwall),
MF (Mineral
Fork
diamictite), T
(Tintic
quartzite) in
each sample.
Values for
intensities
are: 1 (very
low), 2 (low),
3 (low-
moderate), 4
(moderate), 5
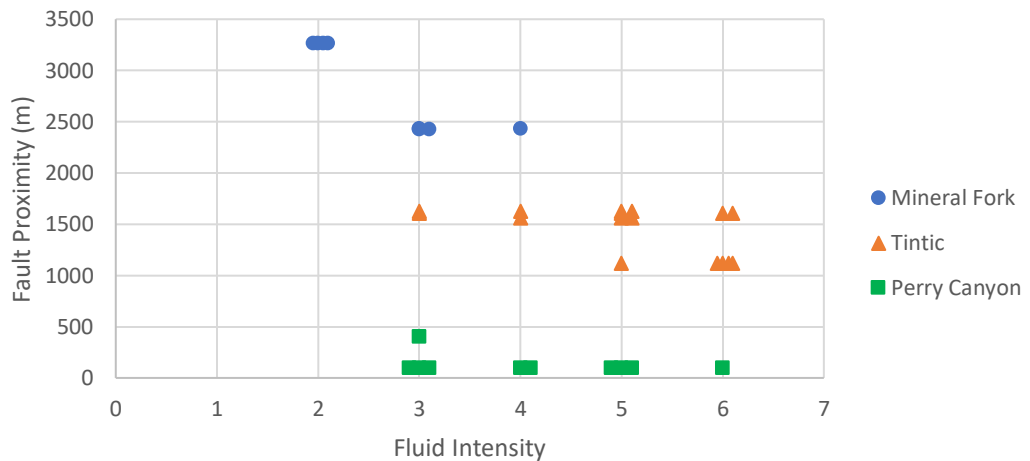(moderate-
high), and 6
(high).p

6. EBSD Analysis

6.1 Results

The indexed quartz phase fraction, or hit rate, in the samples ranged from 23.36% to 60.19%, with an average hit rate of 39.98% (Fig. 30). These values are considered adequate for quartz CPO analysis because they are comparable to other EBSD studies (Fazio et al., 2017; Orlandini & Mahan, 2020) and because phase maps for each sample, which show the area of EBSD acquisition and provide a visual representation of the hit rate and general grain size (Fig. 30), look reasonably similar to the thin sections. Lower indexed samples can be attributed to a poor polish, a high concentration of hard-to-detect phases such as micas, or a combination of these two factors. Given that most of these samples are quartzites, and therefore have a very high quartz content, poor polishing is likely responsible for the relatively low hit rates. Additional polishing resulted in improved hit rates in subsequent runs, though still not as high as in previous studies. High mica concentrations also contributed to low indexing in certain samples. For example, AI1902B has the lowest hit rate of 23.36%. This high strain diamictite sample is also one of the most mica-rich samples based on petrographic observations. The number of grains in each sample used to create the one point per grain CPO pole figures ranged from 2,368 to 8,328, with an average number of 4,523 (Table 6).
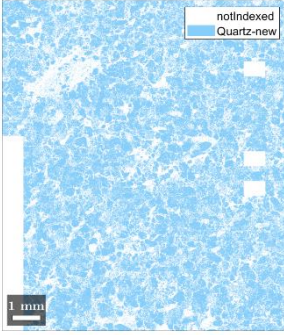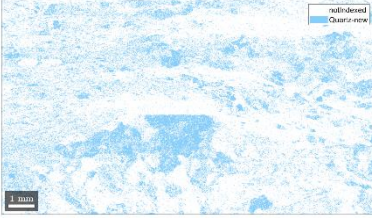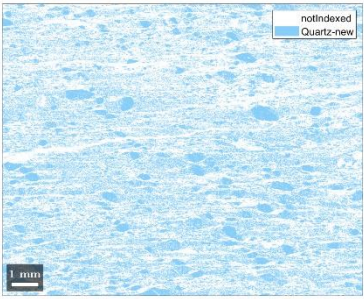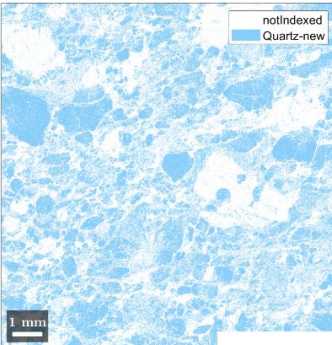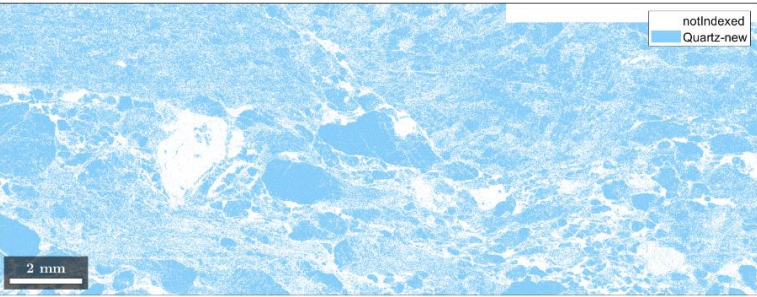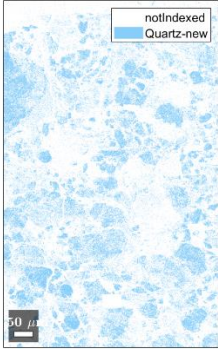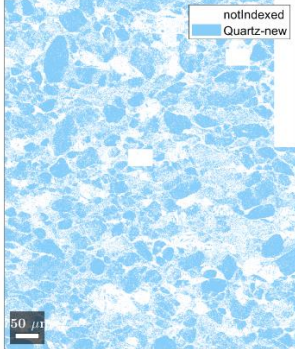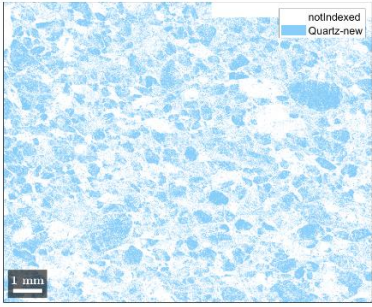
AI1901C HR: **60.19** Antelope Island Mineral Fork Diamictite	**AI1902B** HR: **23.36** Antelope Island Mineral Fork Diamictite	**AI1903B** HR: **40.12** Antelope Island Mineral Fork Diamictite

AI1904D HR: 43.25 Antelope Island Tintic Quartzite	**AI1905B** HR: 58.57 Antelope Island Tintic Quartzite

AI1905D HR: 23.73 Antelope Island Tintic Quartzite	**AI1906A** HR: 52.92 Antelope Island Tintic Quartzite	**AI1906B** HR: 37.98 Antelope Island Tintic Quartzite

Figure 30. Phase maps for the 16 EBSD samples. Sample names and hit rates (HR) are provided above each map. Quartz is represented by blue and non-indexed areas are white.
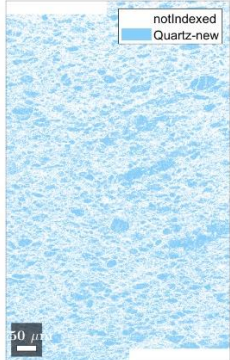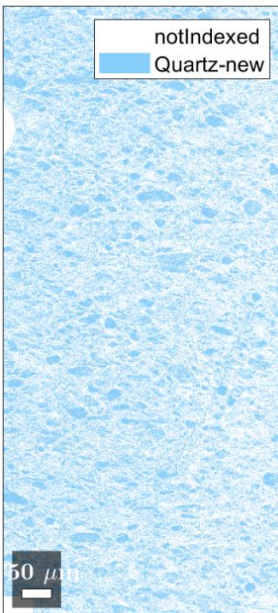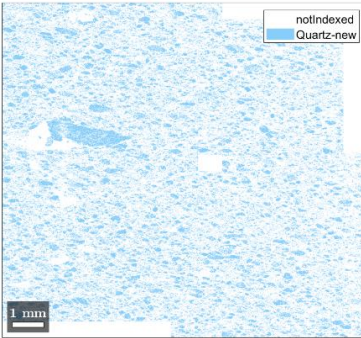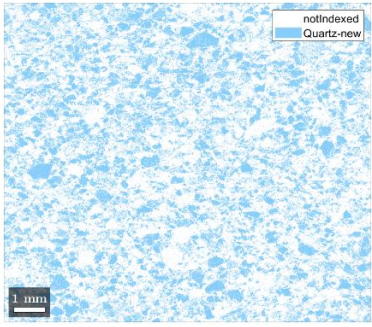
AI1907A HR: 27.93 Antelope Island Tintic Quartzite	AI1907B HR: 37.63 Antelope Island Tintic Quartzite	AI1907C HR: 44.04 Antelope Island Tintic Quartzite
PV1901B HR: 41.51 Pineview Reservoir Perry Canyon Quartzite	PV1901D HR: 43.12 Pineview Reservoir Perry Canyon Quartzite	PV1901E HR: 42.79 Pineview Reservoir Perry Canyon Quartzite
PV1901H HR: 26.85 Pineview Reservoir Perry Canyon Quartzite	PV1902A HR: 35.73 Pineview Reservoir Perry Canyon Quartzite	

Figure 30. Phase maps for the 16 EBSD samples. Sample names and hit rates (HR) are provided above each map. Quartz is represented by blue and non-indexed areas are white.

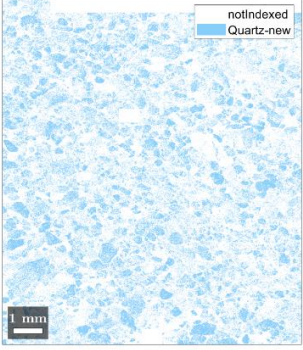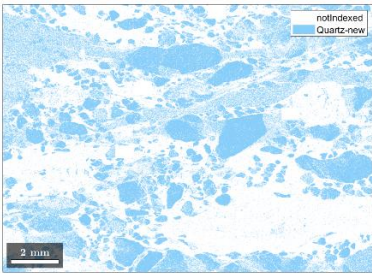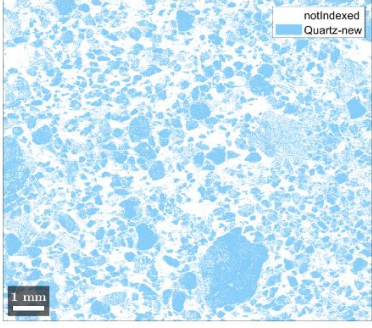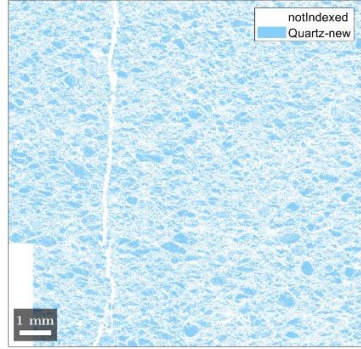| Sample	Indexed Points	Grains
AI1901C	89318	7816
AI1902B	77518	2368
AI1903B	20947	4087
AI1904D	77734	3883
AI1905B	17400	8328
AI1905D	37923	2722
AI1906A	82047	3058
AI1906B	64798	3960
AI1907A	49506	3354
AI1907B	107895	3748
AI1907C	63696	4322
PV1901B	109560	5473
PV1901D	103495	5806
PV1901E	146573	4487
PV1901H	89654	4069
PV1902A	93208	4892

Table 6. Includes the values of indexed points and the number of grains derived from the indexed points that were used to create the pole figures for each sample.

6.11 Pole Figure Geometry

Most samples show weak lattice preferred orientations with multiples of uniform distribution (m.u.d.) no higher than 2.5 (Fig. 31). Most samples are best classified as single girdles; however, many are very weakly defined (AI1901C, AI1904D, AI1905B, AI1906A, AI1906B, PV1901D, PV1901E, and PV1902A). Single point geometries are the next most frequent pole figure geometry among the samples (AI1902B, AI1903B, AI1905D, AI1907A, AI1907B, and AI1907C). Cross girdles are the least common geometry. There are only two samples (PV1901B and PV1901H) that could be classified as cross girdles; however, it is difficult to distinguish whether these samples are single girdles or cross girdles (Fig. 31). As suggested by Toy et al. (2008), these samples could represent a transitional type between single and crossed girdles.
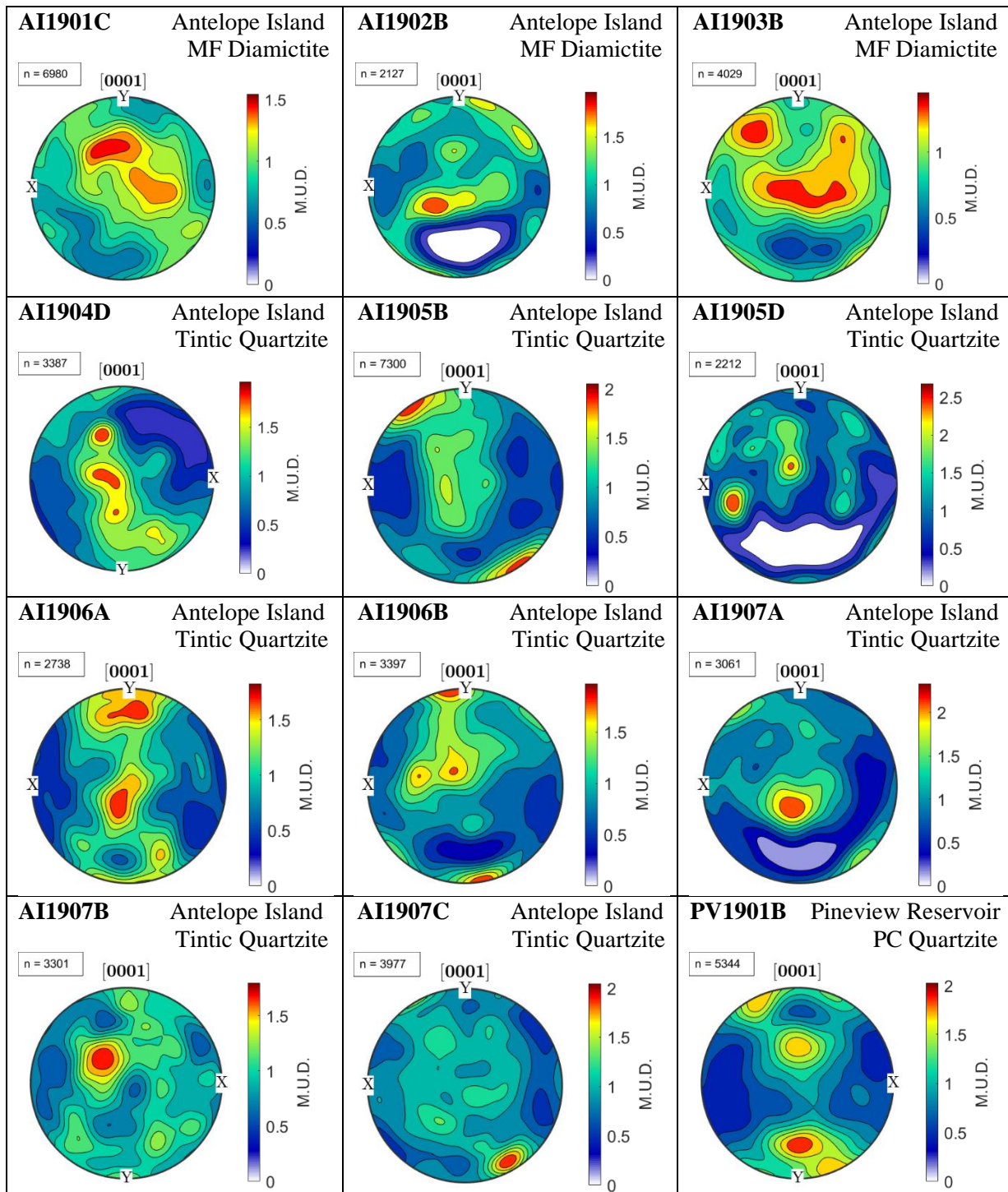
Figure 31. Pole figures displaying quartz CPO fabrics. Quartz pole figures are shown on lower hemisphere stereoplots in the finite strain X:Z reference frame. The east side of the X-axis is on the right. M.U.D = multiples of uniform density. n = number of orientations.
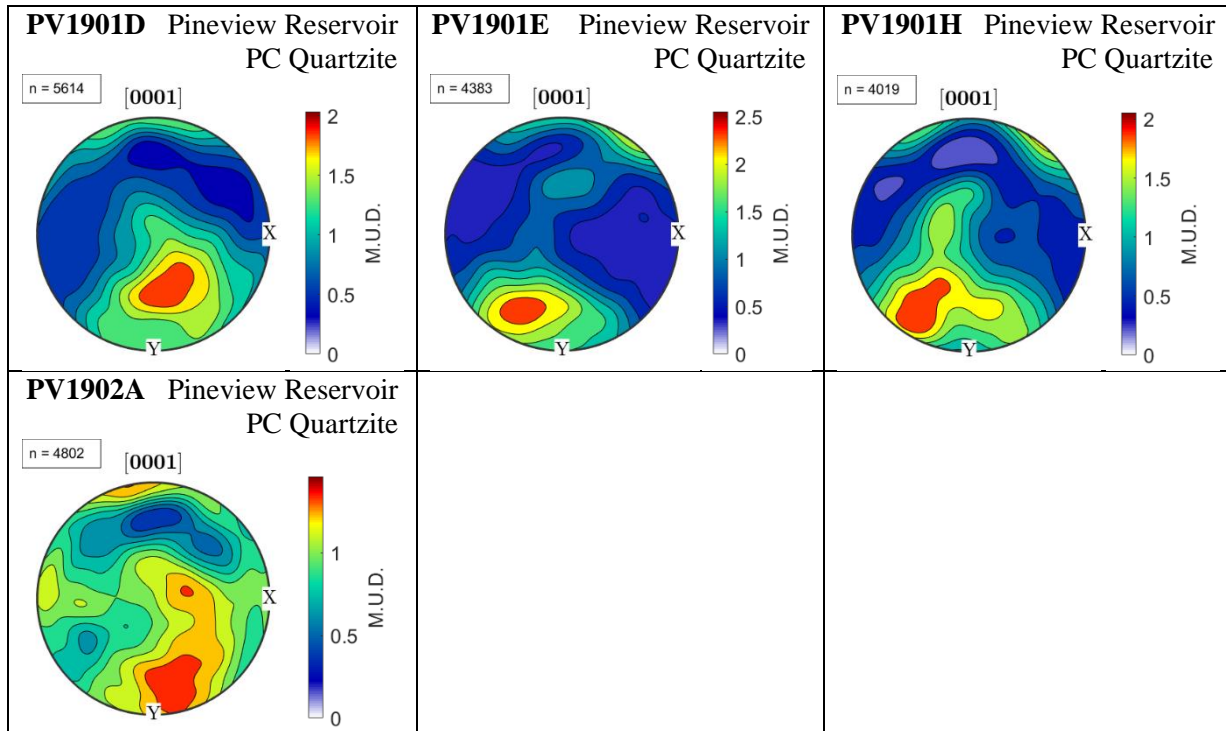
Figure 31. Pole figures displaying quartz CPO fabrics. Quartz pole figures are shown on lower hemisphere stereoplots in the finite strain X:Z reference frame. The east side of the X-axis is on the right. M.U.D = multiples of uniform density. n = number of orientations.

6.12 *CPO Strength*

M-index values for the samples are low, but not abnormal for low strain samples from other shear zones (Orlandini & Mahan, 2020; Singleton et al., 2020; Starnes et al., 2020; Watanuki et al., 2020). An M-index value of zero is equivalent to a completely random fabric, a value of one represents a single crystal fabric, and values around 0.45 are considered very strong (Skemer et al., 2005). Values for these samples range from 0.0092 to 0.0876, with an average of 0.0335 and a median of 0.0326 (Table 7). These values correspond to generally weak CPO fabrics.

Sample	M-Index
AI1901C	0.0116
AI1902B	0.0252
AI1903B	0.0092
AI1904D	0.0413
AI1905B	0.0221
AI1905D	0.0388
AI1906A	0.0402
AI1906B	0.0316
AI1907A	0.0353
AI1907B	0.0336
AI1907C	0.0112
PV1901B	0.0257
PV1901D	0.0615
PV1901E	0.0876
PV1901H	0.0429
PV1902A	0.0187

Table 7. Includes sample names and their corresponding M-index values.

6.2 Discussion

6.21 *Symmetry/Vorticity*

If pole figures display a strong pattern that fit a girdle, then the MTEX script used to determine symmetry (a proxy for vorticity) will produce four values that relate to the position, orientation, and intensity of girdle maxima (Hunter et al., 2018). These samples' low M-index values represent relatively weak fabrics. Additionally, visual observations of the pole figures

show that few samples loosely match a girdle pattern (AI904D, AI1905B, AI1906A, PV1901B, PV1901E, and AI1906B). When each sample was run through the script, no significant maxima were defined. Therefore, a quantitative vorticity analysis was not possible due to the weakness of the CPOs. A qualitative vorticity analysis related to the CPO geometries is discussed below.

6.22 Pole Figure Geometry

The geometries of the pole figures do not appear to have a strong relationship with lithology, however a weak relationship is observed with location. All hanging wall samples most closely fit a girdle geometry. However, in the footwall, samples are split evenly between single girdle and point geometries. Within each rock type in the footwall, single girdle geometries are more common in the samples farther away from the fault, while single point geometries are more common with samples closer to the fault. This is similar to findings from Toy et al. (2008). This is likely attributable to the fact that the single point geometries are primarily related to prism <a> slip, which is linked to deformation at higher temperatures, ~500 °C (Hobbs, 1968; Baeta & Ashbee, 1970; Tullis et al., 1973; Stipp et al., 2002).

Lithologically, Tintic quartzite samples are evenly split between single girdle and point geometries, with samples closer to the fault more closely fitting a point geometry and those farther away from the fault more closely fitting single girdle geometries. Both high strain diamictite samples (closer to the fault) are classified as point geometries and the one medium strain diamictite sample (further from the fault) has a single girdle geometry. All Perry Canyon graywacke samples have girdle geometries.

Vorticity can be qualitatively interpreted from girdle pole figure geometries. Girdles that are symmetric about the y-axis are related to coaxial deformation (pure shear), while pole figures

69

that are asymmetric about the y-axis are related to noncoaxial deformation (simple shear). Additionally, the sense of shear can by interpreted by the rotation of the girdle (Schmid & Casey, 1986; Law et al., 1990). The samples that have a strong enough girdle pattern for this analysis are AI1904D, AI1905B, AI1906A, and AI1906B in the footwall and PV1901B, PV1901E, PV1901H, and PV1902A in the hanging wall. For the footwall samples, samples AI1906A and AI1906B are symmetric girdles, indicating a large pure shear component, and AI1904D and AI1905B are asymmetric girdles, indicating simple shear. Both asymmetric girdles indicate top to the west simple shear, which is contradictory to what is expected based on the regional geology. It is possible that local deformation is influencing the fabric, as both samples are located on a minor fold. In the hanging wall, PV1901B, PV1901H, and PV1902A are symmetric girdles, indicating pure shear deformation, and PV1901E is asymmetric, indicating top to the east simple shear. This direction is consistent with the regional geology and patterns of mesoscopic structures (Yonkee, 2005). The pure shear component is also consistent with Yonkee's (2005) kinematic model of sub-simple shear. Overall, there does not appear to be a pattern between vorticity and rock type, location, or strain magnitude.

6.23 CPO Strength

There are a few factors that are related to the CPO strength (Fig. 32 and 33). The strongest relationships are between CPO strength and quartz content and proximity to fault. Higher M-index values, related to a stronger fabric, occur in samples that have more quartz and that are closer to the fault. Previous research along the Willard fault shows that all quartz-rich rocks have microstructural evidence for crystal plasticity. This is confirmed by the petrographic analysis done in this study. However, it was unknown whether the amount of crystal plasticity increased near the fault, or whether the stronger deformation found there was due to increased

brittle deformation and fluid infiltration, or potentially even a component of enhanced diffusive mass transfer enabled by fluids (Barszewski, 2012; Yonkee et al., 2013). The stronger CPO intensities towards the fault suggest that the fluids, in this case, increased the amount of crystal plasticity. Microstructural evidence indicates that diffusion also increased towards the fault in rocks with finer grain sizes and more mica. However, instead of replacing the crystal plasticity, diffusion added to the deformation, resulting in higher strain near the fault. It is possible that these two mechanisms were occurring simultaneously, but also possible that they dominated at different times depending on the availability of fluids.

Weaker, positive correlations also exist between CPO strength and fluid interaction and grain size. It is possible that samples with a smaller grain size have weaker CPOs because of increased diffusion in finer-grained samples.
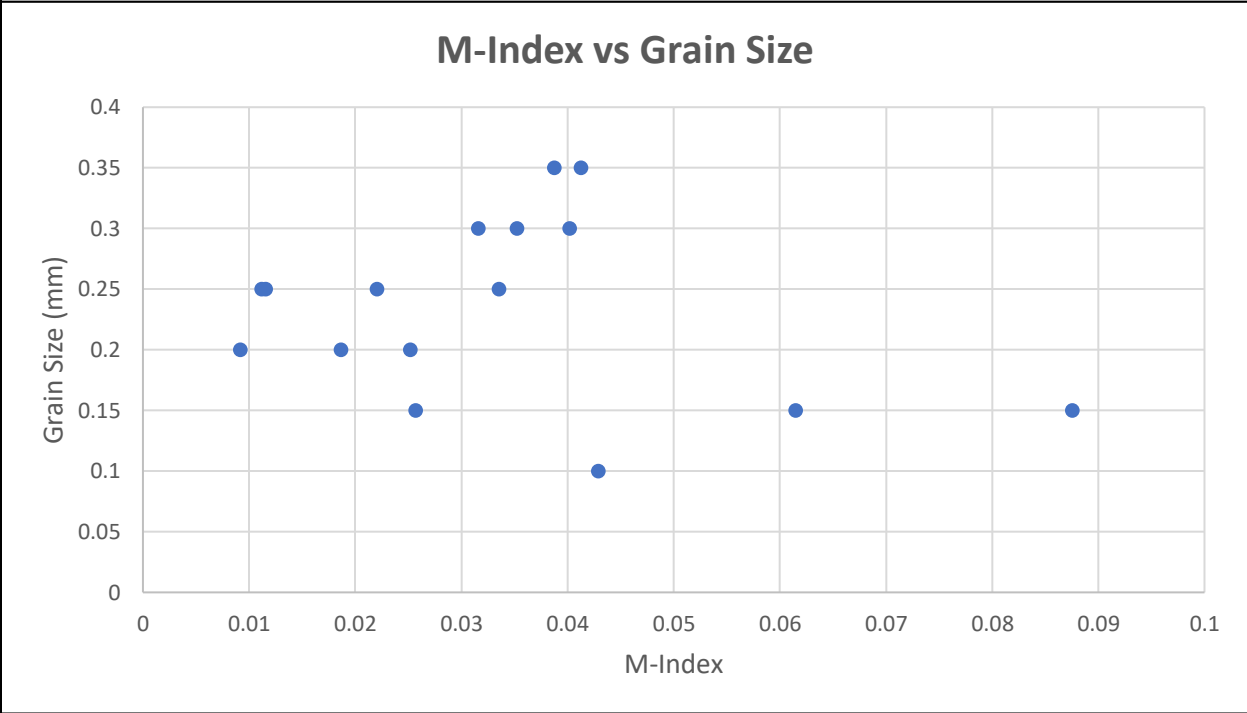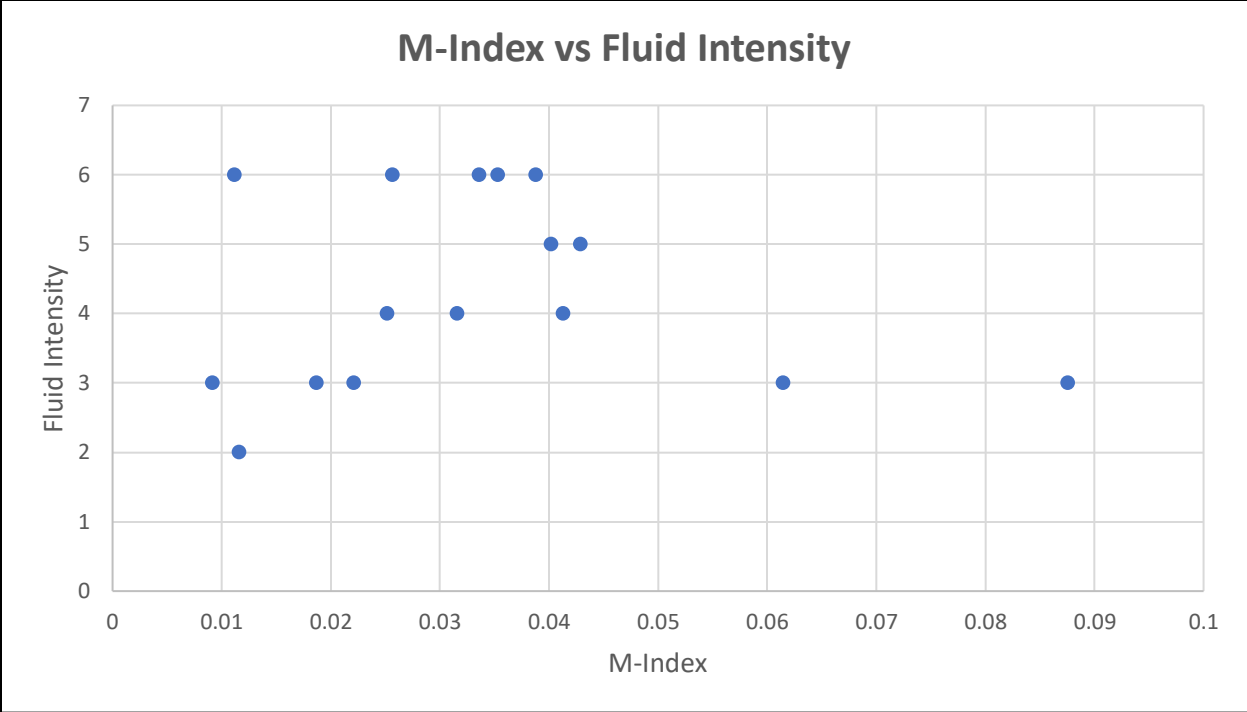
Figure 32. Graphs show the relationship between M-index values and fluid intensity and grain size.
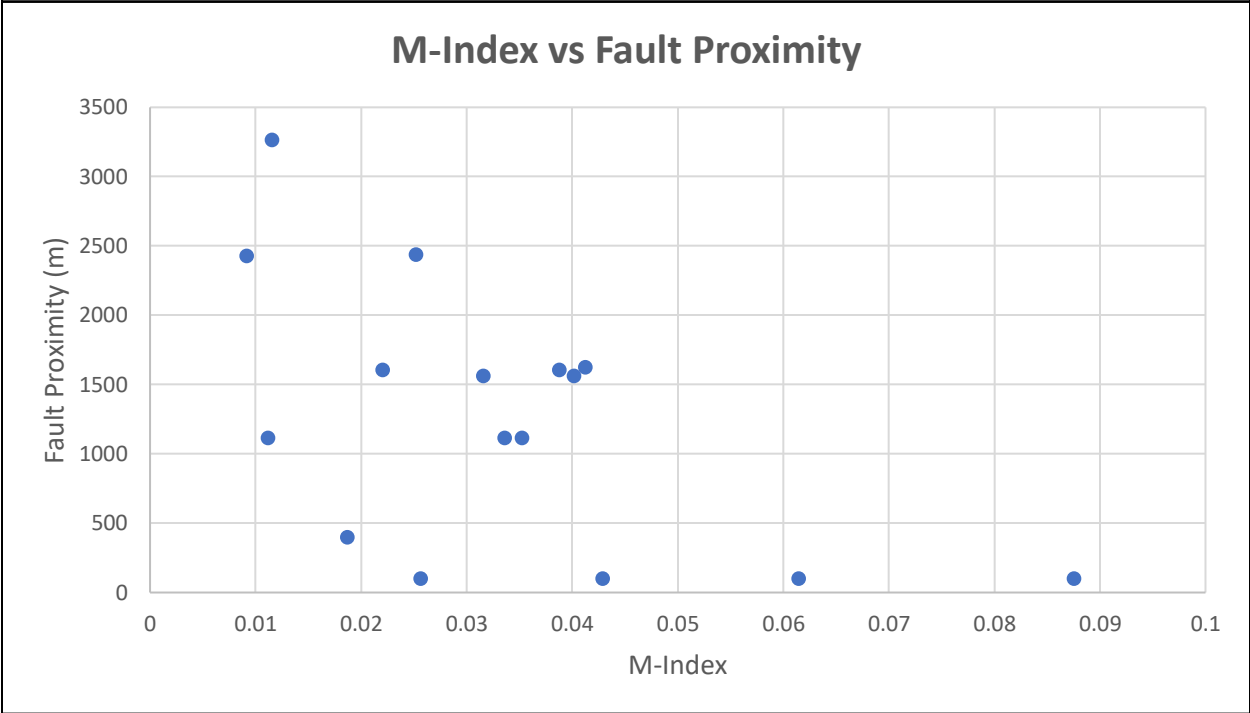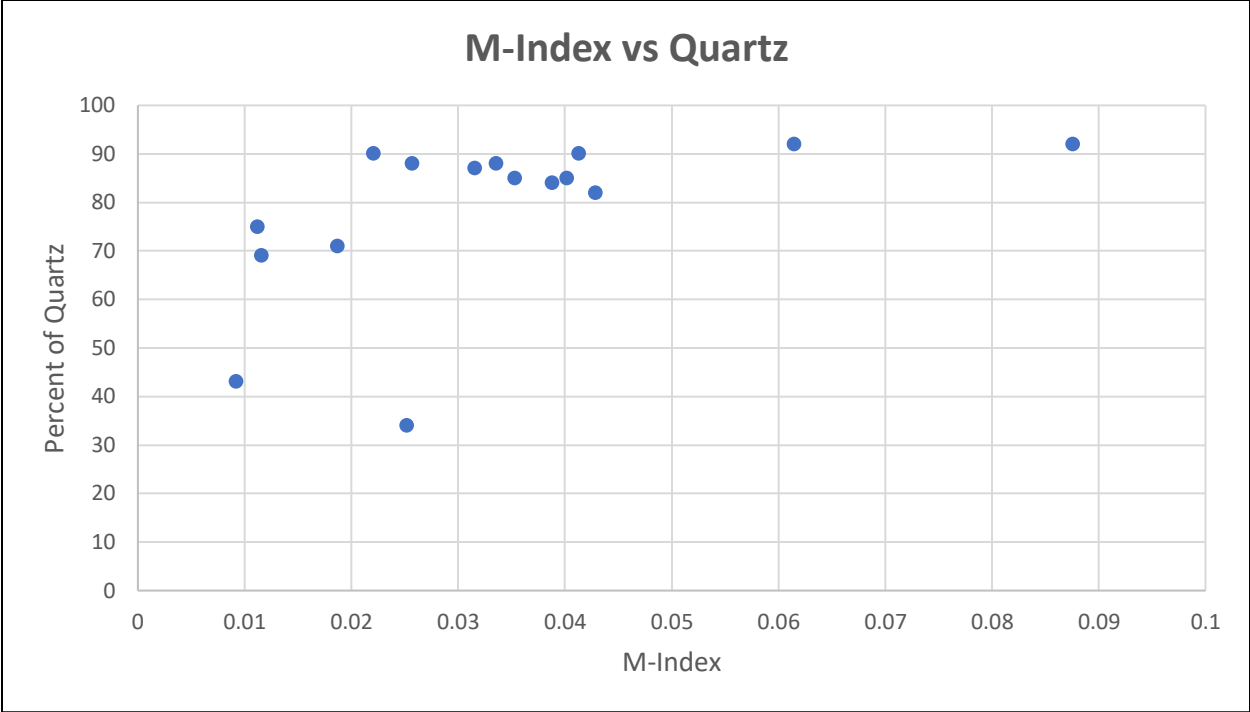
Figure 33. Graphs show the relationship between M-index values and quartz content and fault proximity.

Approximately one third of the samples show patterns indicative of prism <a> slip, with c-axis maxima subparallel to the Y strain direction. These samples are all from the footwall (Antelope Island) within both the diamictite and Tintic Quartzite samples. Approximately one third of samples have c-axis maximum subparallel to the Z strain direction, compatible with basal <a> slip. These samples include footwall Tintic quartzite and hanging wall quartzites from the Perry Canyon formation. Approximately one third of samples show <a> slip on multiple planes, represented by a c-axis girdle sub-perpendicular to the X strain direction. These samples include all lithologies, including footwall Mineral Fork diamictite and Tintic Quartzite and hanging wall Perry Canyon quartzites. Only one sample, AI1905D, displays a c-axis maxima subparallel to X, suggesting prism [c] slip (Table 8).

Temperatures associated with each slip system are also recorded in Table 8. Illite crystallinity and mineralogy in the Willard suggest maximum temperatures in the range of 300 to 500 °C, with somewhat lower maximum temperatures in the footwall (Yonkee et al., 1989). All but one sample (AI1905D) fall into this temperature range, with one third suggesting a temperature of 500 °C and two thirds suggesting temperatures less than 500 °C. However, the active slip systems indicate higher temperatures in the footwall compared to the hanging wall.

Slip System	Associated Temperature	Sample	Lithology
Prism <a>	500 °C	AI1901C	Mineral Fork diamictite, medium strain (footwall)
Prism <a>	500 °C	AI1902B	Mineral Fork diamictite, high strain (footwall)
Prism <a>	500 °C	AI1904D	Tintic quartzite, pink (footwall)
Prism <a>	500 °C	AI1907A	Tintic quartzite, pink (footwall)
Prism <a>	500 °C	AI1907B	Tintic quartzite, clast-rich (footwall)
Basal <a>	less than 500 °C	A1905B	Tintic quartzite, clast-rich (footwall)
Basal <a>	less than 500 °C	AI1907C	Tintic quartzite, green (footwall)
Basal <a>	less than 500 °C	PV1901D	Perry Canyon graywacke, massive (hanging wall)
Basal <a>	less than 500 °C	PV1901E	Perry Canyon graywacke, thinly bedded (hanging wall)
Basal <a>	less than 500 °C	PV1901H	Perry Canyon graywacke, shaly (hanging wall)
Mixed <a>	less than 500 °C	AI1903B	Mineral Fork diamictite, high strain (footwall)
Mixed <a>	less than 500 °C	AI1906A	Tintic quartzite, green (footwall)
Mixed <a>	less than 500 °C	AI1906B	Tintic quartzite (pink), footwall
Mixed <a>	less than 500 °C	PV1901B	Perry Canyon graywacke, massive (hanging wall)
Mixed <a>	less than 500 °C	PV1902A	Perry Canyon graywacke, thinly bedded (hanging wall)
Prism [c]	greater than 550 °C	AI1905D	Tintic quartzite, pink (footwall)

Table 8. Shows each sample's active slip system and associated temperature.

6.25 Deformation Mechanisms

The fact that CPO patterns are observed suggests that dislocation creep (crystal plasticity) was active, which is consistent with the observed microstructures. However, the generally weak strength of those patterns suggests that other mechanisms, such as diffusion, is also important. However, when plotting the strength of the CPO against the intensity of crystal plasticity and diffusion, a visible relationship is not observed (Fig. 34).
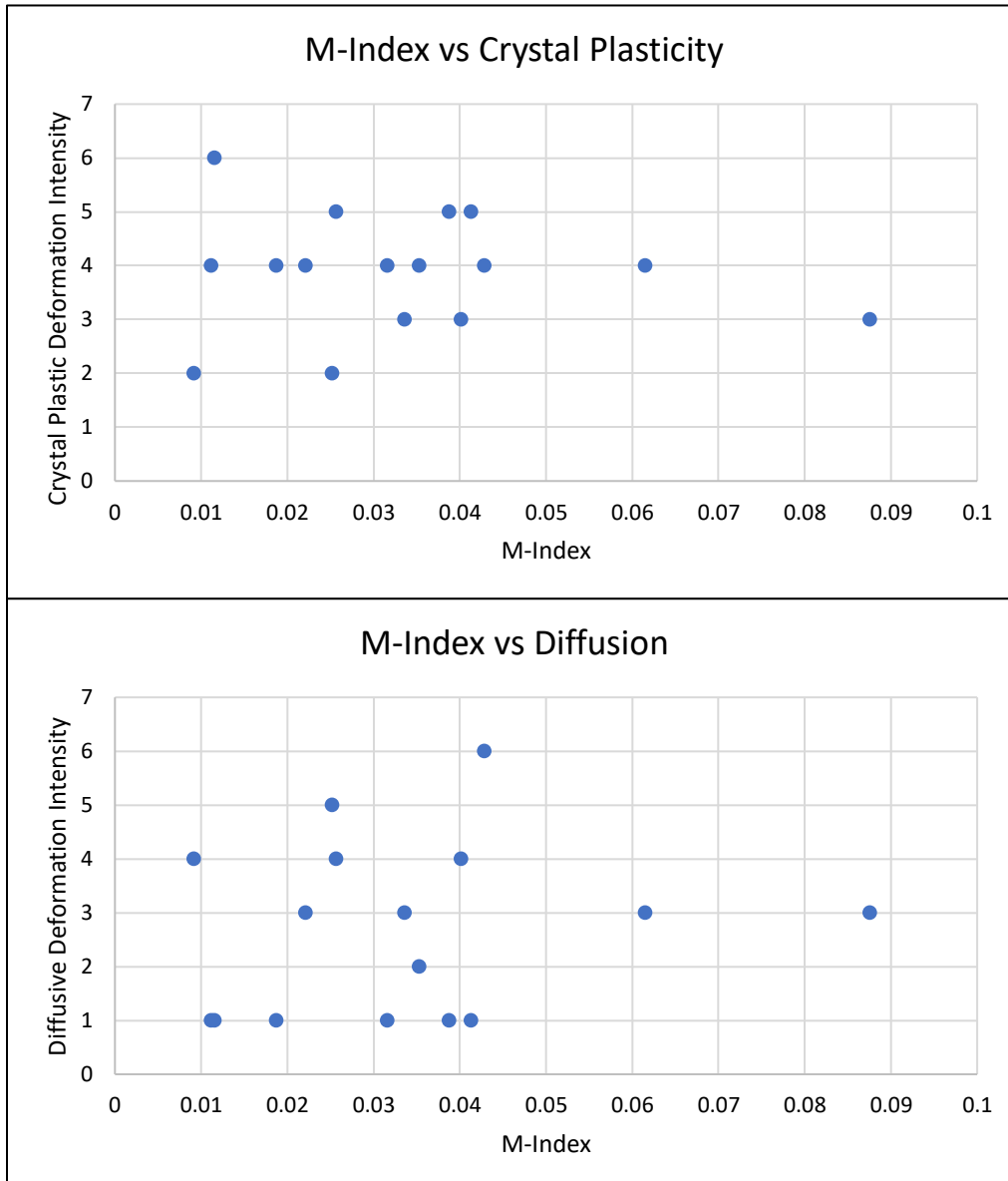
Figure 34. Graphs show the relationship between M-index values and crystal plastic and diffusive deformation.

7. Conclusion

Because of the complex nature of CPOs, many studies are conducted on experimentally deformed rocks, where factors such as mineralogy, strain, or fluid phase can be held constant (Hirth & Tullis, 1992; Heilbronner &Tullis, 2006; Cross et al., 2017). Examining naturally deformed rocks is important because of real-world applications; however, it also introduces many complexities to the interpretation of the results. This study used both petrographic and CPO analyses to better understand the relationships between the many factors present during deformation.

The petrographic analysis showed that all the samples are dominated by crystal plasticity (footwall samples of medium strained diamictite and Tintic quartzite) or a combination of crystal plasticity and diffusive deformation (footwall samples of high strained diamictite and hanging wall graywacke, which has relatively low strain). Deformation by brittle fracturing also played a minor role in the samples, with the highest degree of embrittlement in the Tintic quartzites. One of the main goals of this study was to determine whether fluid interaction had any effect on the dominant deformation mechanism. Generally, increased fluid interaction was correlated to increased contributions of both brittle and diffusive deformation. In finer-grained samples, fluids drove diffusion, and in larger-grained samples, fluids enhanced brittle deformation, likely through transient embrittlement due to increased fluid pressures.

However, fluid is not the only factor that appeared to affect the dominant deformation mechanism. Relationships were also explored between deformation mechanisms and grain size, mineralogy, and fault proximity. Contributions of brittle deformation increased with increasing quartz content and increasing distance from the fault. Crystal plasticity increased with increasing

grain size, increasing quartz content, and decreasing distance from the fault. Diffusion increased with decreasing grain size, decreasing quartz content, and decreasing distance from the fault.

The amount of evidence for fluid interaction was also compared to these three factors. There was no relationship between fluid intensity and grain size. Only a very weak relationship was observed between mineralogy and fluid interaction. Within samples of the same lithology, decreased quartz content increased fluid interaction; however, across all samples, increased quartz content increased fluid interaction. A strong relationship was observed between fault proximity and fluid interaction. As the distance from the fault decreased, the amount of fluid interaction increased.

EBSD was used to further investigate the relationship between fluid intensity and dominant deformation mechanisms, and to also explore relationships between these factors and vorticity, fabric strength, and slip system activation. Overall, the samples produced weak CPO fabrics, suggesting deformation by crystal plasticity with contributions from diffusion. This closely aligns with the petrographic observations.

Because of the weak patterns, a quantitative vorticity analysis could not be performed. However, a qualitative analysis, using the symmetry of pole figure girdles, showed that both pure and simple shear components were present during deformation. Weak patterns and limited data limited the ability to identify any potential relationship between the degree of coaxiality and location or lithology.

CPO strength was strongly related to mineralogy and fault proximity. CPO strength increased with increasing quartz content. It also increased closer to the fault, suggesting increased contributions of crystal plasticity. CPO strength also had weaker, positive correlations to fluid interaction and grain size.

Pole figure geometry and location appeared to co-vary. All hanging wall samples most closely fit a girdle geometry. Footwall samples, which were collected at various distances from the fault, show that within each rock type, single girdle geometries are more common in the samples farther away from the fault, while single point geometries are more common with samples closer to the fault. This has implications for the associated active slip systems and temperatures. The footwall samples that display single girdle geometries (farther from the fault) are associated with a combination of prism <a> and basal <a> slip, which is related to temperatures less than 500 °C. The footwall samples that display point geometries (closer to the fault) are associated with prism <a> slip, which is linked to deformation at higher temperatures, ~ 500 °C.

Overall, many different relationships were observed between deformation mechanisms, fluid interaction, CPO fabric development, grain size, mineralogy, and fault proximity. Analyzing these relationships is complex, but five main takeaways are evident [a summary diagram (Fig. 35) shows takeaways 1-4]:

1. Crystal plasticity is the primary deformation mechanism throughout all samples. When fluid enters the system, it can either increase the component of brittle deformation (in rocks with a larger grain size and increased quartz) or diffusion (in rocks with a smaller grain size and increased mica), suggesting that the response to fluid is controlled by lithology.

2. High strain at the fault is accomplished by enhanced crystal plasticity (as evidenced by the stronger CPO fabrics) and additional diffusive mass transfer, which is a response to increased fluid flow (as evidenced by microstructural analysis). It is not yet understood

whether these two mechanisms were always simultaneous. It is possible that fluid pumping caused temporal variations in dominant deformation mechanisms.

3. The increased diffusion and fluid interaction near the fault support the idea that the fault channelized fluid flow.

4. Most CPO fabrics are single girdles, indicative of basal <a> or mixed <a> slip and a temperature less than 500 °C. However, point maxima geometries, indicative of prism <a> slip and a higher temperature of 500 °C, become more prominent closer to the fault. The increase of prism <a> slip and fluid interaction near that fault may suggest fluid-induced hydrothermal heating near the fault.

5. It appears that fluid has the largest control on deformation mechanisms. Mineralogy and fault proximity have the next largest influence; however it should be noted that fault proximity is not independent of fluids. Grain size has the smallest effect on deformation mechanisms. Overall, the controls of deformation mechanisms are: fluid >> mineralogy = fault proximity > grain size.

1. Crystal Plasticity dominates throughout all samples.

Addition of fluids

Response is controlled by lithology.

Increased diffusive deformation (smaller grain size and more mica)

Increased brittle deformation (larger grain size and more quartz)

Increased diffusive deformation near fault

+

Increased fluid interaction near fault

+

Increased crystal plasticity near fault

=

2. High strain near the fault

3. Fault channelized fluids.

4. Increased prominence of prism slip near fault

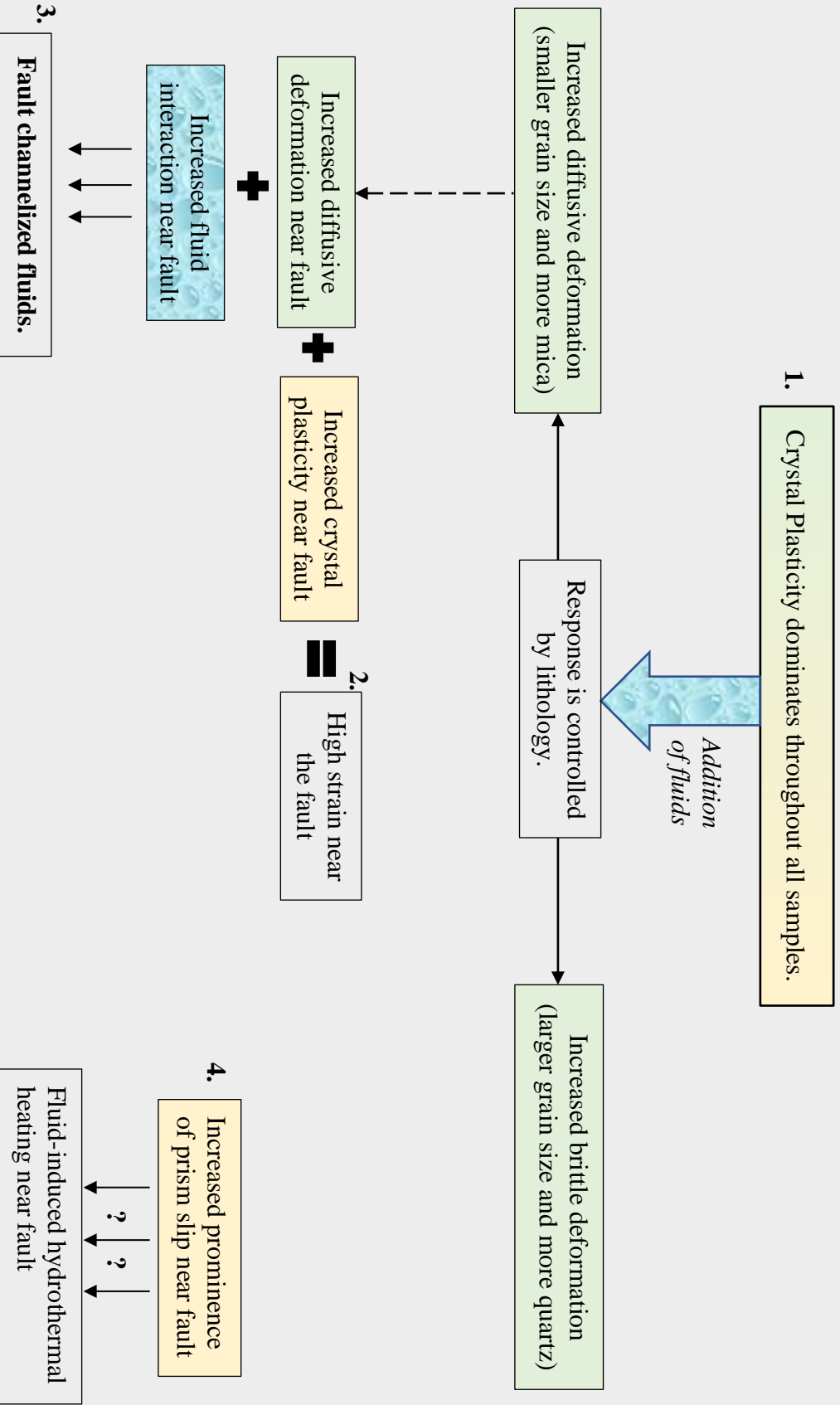Fluid-induced hydrothermal heating near fault

? ?

Figure 35. Summary diagram of the main conclusions. Text boxes shaded in green are evidenced by the petrographic analysis and text boxes shaded in yellow are evidenced by the EBSD analysis. The numbering of conclusions matches the numbering in the text above.

81

References

Akhavan, A. C., 2013. Quartz Structure. Retrieved August 19, 2020, from

    http://www.quartzpage.de/gen_struct.html

Armstrong, F. C. & Oriel, S. S., 1965. Tectonic development of the Idaho-Wyoming thrust belt.

    American Association of Petroleum Geologists Bulletin 49, 1847–1866.

Armstrong, L. R., 1968. Sevier orogenic belt in Nevada and Utah. Geological Society of

    America Bulletin 79(4), 429–458.

Baeta, R. D. & Ashbee, K. H. D., 1970. Mechanical deformation of quartz I: constant strain rate

    compression experiments. Philosophical Magazine 22, 601-624.

Balgord, E. A., Yonkee, W. A., Link, P. K., & Fanning, C. M., 2013. Stratigraphic,

    geochronologic, and geochemical record of the Cryogenian Perry Canyon Formation,

    northern Utah: Implications for Rodinia rifting and snowball Earth glaciation. Bulletin of

    the Geological Society of America 125(9–10), 1442–1467.

    https://doi.org/10.1130/B30860.1

Barszewski, C., 2012, Microstructural and cathodoluminescence (SEM-CL) analyses of clasts in

    a tectonically deformed diamictite from the Willard Thrust, UT. M.S. thesis. University

    of Wisconsin, Milwaukee.

Barth, N. C., Hacker, B. R., Seward, G. G. E., Walsh, E. O., Young, D., & Johnston, S., 2010.

    Strain within the ultrahigh-pressure Western Gneiss region of Norway recorded by quartz

    CPOs. In Law et al. (Ed.), *Continental Tectonics and Mountain Building: The Legacy of

    Peach and Horne* (335, 7-27). London: Geological Society, Special Publications.

Beach, A. & Fyfe, W. S., 1972. Fluid transport and shear zones at Scourie, Sutherland: Evidence

    for overthrusting?. Contributions to Mineralogy and Petrology 36, 175-180.

Bland, P. A., Howard, L. E., Prior, D. J., Wheeler, J., Hough, R. M., & Dyl, K. A., 2011. Earliest rock fabric formed in the Solar System preserved in a chondrule rim. Nature Geoscience 4, 244-247.

Bouchez, J. L., Lister, G. S., & Nicolas, A., 1983. Fabric asymmetry and shear sense in movement zones. Geologische Rundschau 72, 401-419.

Bunge, H. J., 1982. Texture analysis in materials science. https://doi.org/10.1016/0261-3069(83)90207-8

Burnley, P., n.d. Quartz Deformation. Retrieved August 19, 2020, from https://pamelaburnley.net/quartz-deformation/

Burtner, R. L. & Nigrini, A., 1994. Thermochronology of the Idaho-Wyoming thrust belt during the Sevier Orogeny: a new, calibrated, multiprocess thermal model. American Association of Petroleum Geologists Bulletin 78, 1586-1612.

Caine, J. S., Evans, J. P., & Forster, C. B, 1996. Fault zone architecture and permeability structure. Geology 24 (11), 1025-1028.

Carter, N. L., Kronenberg, A. K., Ross, J. V., & Wiltschko, D. V., 1990. Control of fluids on deformation of rocks. In Knipe, R. J. & Rutter, E.H. (Ed.), *Deformation Mechanisms, Rheology and Tectonics* (54, 1-14). London Geological Society, Special Publications.

Coogan, J. C., 1992. Thrust Systems and Displacement Transfer in the Wyoming-Idaho-Utah Thrust Belt. Ph.D. dissertation. University of Wyoming.

Cox, S. F., 2005. Coupling between deformation, fluid pressures, and fluid flow in ore-producing hydrothermal systems at depth in the crust. Economic Geology 100, 39-75.

Crittenden, M. D., 1972. Willard Thrust and the Cache Allochthon, Utah. Geological Society of America Bulletin 83, 2871–2880.

Cross, A. J., Hirth, G., & Prior, D. J., 2017. Effects of secondary phases on crystallographic preferred orientation in mylonites. Geological Society of America, Geology (Boulder) 45 (10), 955-958.

DeCelles, G., 1994. Late Cretaceous-Paleocene synorogenic sedimentation and kinematic history of the Sevier thrust belt, northeast Utah and southwest Wyoming. Geological Society of America Bulletin 106, 32-56.

DeCelles, P. G. & Coogan, J. C., 2006. Regional structure and kinematic history of the Sevier fold-and-thrust belt, central Utah. Geological Society of America Bulletin 118, 841-864.

DeCelles, P. G., 2004. Late Jurassic to Eocene evolution of the Cordilleran thrust belt and foreland basin system, western U.S.A. American Journal of Science 304, 105-168.

Den Brok, S. W. J. & Spiers, C. J., 1991. Experimental evidence for water weakening of quartzite by microcracking plus solution-precipitation creep. Journal of the Geological Society of London 148 (3), 541-548.

Doelling, H. H., Willis, G. C., Jensen, M. E., Hecker, S., Case, W. F., & Hand, J. S., 1990. Geologic map of Antelope Island Davis County, Utah. Utah Geological and Mineral Survey.

Dorr, J. A., Spearing, D. R., Steidtmann, J. R., 1977. Deformation and deposition between a foreland uplift and an impinging thrust belt; Hoback Basin, Wyoming. Geological Society of America Special Paper 177, 82.

Etchecopar, A., 1977. A plane kinematic model of progressive deformation in a polycrystalline aggregate. Tectonophysics 39, 121-139.

Etheridge, M. A., Wall, V. J., & Cox, S. F., 1984. High fluid pressures during regional metamorphism and deformation: Implications for mass-transport and deformation mechanisms. Journal of Geophysical Research 89, 4344–4358.

Fazio, E., Punturo, R., Cirrincione, R., Kern, H., Pezzino, A., Wenk, H., Goswami, S., & Mamtani, M. A., 2017. Quartz preferred orientation in naturally deformed mylonitic rocks (Montalto shear zone – Italy): a comparison of results by different techniques, their advantages and limitations. International Journal of Earth Sciences 106, 2259-2278.

Fischer, G. J. & Paterson, M. S., 1989. Dilatancy during rock deformation at high temperatures and pressures: Journal of Geophysical Research 94, 17607–17617.

Fossen, H., 2016. Structural Geology. Cambridge, UK: Cambridge University Press.

Griggs, D. T. & Blacic J. B., 1965. Quartz: anomalous weakness of synthetic crystals. Science 147, 292-295.

Griggs, D., 1967. Hydrolytic weakening of quartz and other silicates: Royal Astronomical Society Geophysical Journal 14, 19–31.

Heilbronner, R. & Tullis, J., 2006. Evolution of c axis pole figures and grain size during dynamic recrystallization: Results from experimentally sheared quartzite. Journal of Geophysical Research 111 (B10202).

Hielscher, R. & Schaeben, H., 2008. A novel pole figure inversion method: specification of the MTEX algorithm. Journal of Applied Crystallography 41(6), 1024-1037.

Hirth, G. & Tullis, J., 1992. Dislocation creep regimes in quartz aggregates. Journal of Structural Geology 14, 145-159.

Hobbs, B. E., 1968. Recrystallization of single crystals of quartz. Tectonophysics 6, 353-401.

Hunter, N. J. R., Weinberg, R. F., Wilson, C. J. L., & Law, R. D., 2018. A new technique for quantifying symmetry and opening angles in quartz *c*-axis pole figures: Implications for interpreting the kinematic and thermal properties of rocks. Journal of Structural Geology 112, 1-6.

Jamtveit, B., Austrheim, H., & Putnis, A., 2016. Disequilibrium metamorphism of stressed lithosphere. Earth-Science Reviews 154, 1-13.

Kilian, R., Heilbronner, R., & Stünitz, H., 2011. Quartz microstructures and crystallographic preferred orientation: Which shear sense do they indicate? Journal of Structural Geology 33, 1446-1466.

Knipe, R. J., & McCaig, A. M., 1994. Microstructural and microchemical consequences of fluid flow in deforming rocks. Geological Society London Special Publication 78, 99–111.

Kruckenberg, S. C., Michels, Z. D., & Parsons, M. M., 2019. From intracrystalline distortion to plate motion: Unifying structural, kinematic, and textural analysis in heterogeneous shear zones through crystallographic orientation-dispersion methods. Geosphere 15 (2), 1-25.

Lamarque, G., Bascou, J., Maurice, C., Cottin, J., Riel, N., & Ménot, R., 2016. Microstructures, deformation mechanisms and seismic properties of a Paleoproterozoic shear zone: The Mertz shear zone, East-Antarctica. Tectonophysics 680, 174-191.

Laubach, S. E., Lander, R., Bonnell, L., Olson, J., & Reed, R., 2004. Opening histories of fractures in sandstone. In Cosgrove, J. W & Engelder, T. (Ed.) *The initiation, propagation, and arrest of joints and other fractures* (231, 1-9). London Geological Society, Special Publications.

Law, R. D., 1986. Relationships between strain and quartz crystallographic fabrics in the Roche Maurice quartzites of Plougastel, western Brittany. Journal of Structural Geology 8, 493-515.

Law, R. D., 1987. Heterogeneous deformation and quartz crystallographic fabric transitions: natural examples from the Moine thrust zone at the Stack of Glencoul, Northern Assynt. Journal of Structural Geology 9, 819-833.

Law, R. D., Schmid, S. M., & Wheeler, J., 1990. Simple shear deformation and quartz crystallographic fabrics: a possible natural example from the Torridon area of NW Scotland. Journal of Structural Geology 12 (1), 29-45.

Law, R. D., Searle, M. P., & Simpson, R. L., 2004. Strain, deformation temperatures and vorticity of flow at the top of the Greater Himalayan Slab, Everest Massif, Tibet. Journal of the Geological Society 161, 305–320.

Lespinasse, M., 1999. Are fluid inclusion planes useful in structural geology? Journal of Structural Geology 21 (8-9), 1237-1243.

Lister, G. S. & Hobbs, B. E., 1980. The simulation of fabric development during plastic deformation and its application to quartzite: the influence of deformation history. Journal of Structural Geology 2 (3), 355-370.

Lister, G. S. & Williams, P. F., 1979. Fabric development in shear zones: theoretical controls and observed phenomena. Journal of Structural Geology 12, 29-45.

Lister, G. S., 1977. Discussion: Crossed-girdle c-axis fabrics in quartzites plastically deformed by plane strain and progressive simple shear. Tectonophysics 39(1–3), 51–54. https://doi.org/10.1016/0040-1951(77)90087-7

Lister, G. S., 1982. A vorticity equation for lattice reorientation during plastic deformation. Tectonophysics 82, 351–366.

Mainprice, D., Bachmann, F., Hielscher, R., & Schaeben, H., 2014. Descriptive tools for the analysis of texture projects with large datasets using MTEX: Strength, symmetry and components. Geological Society London Special Publications 409, 251-271.

McCaig A. M. & Knipe, R. J., 1990. Mass-transport mechanisms in deforming rocks: Recognition using microstructural and microchemical criteria. Geology 18, 824-827.

McCaig, A. M., 1988. Deep fluid circulation in fault zones. Geology 16, 867-870.

McCaig, A. M., Wayne, D. M., & Rosenbaum, J. M., 2000. Fluid expulsion and dilatancy pumping during thrusting in the Pyrenees: Pb and Sr isotope evidence. GSA Bulletin 112 (8), 1199-1208.

Means, W. D., 1994. Rotational quantities in homogenous flow. Journal of Structural Geology 16, 437-445

Means, W. D., Hobbs, B., Lister, G., & Williams, P., 1980. Vorticity and non-coaxiality in progressive deformations. Journal of Structural Geology 2, 371-378.

Mitra, G., 1997. Evolution of salient in a fold-and-thrust belt: the effects of sedimentary basin geometry, strain distribution and critical taper. In Sengupta, S. (Ed.), *Evolution of geological structures in micro- to macro-scales* (59-90). Chapman and Hall, London.

Morales, L. F. G., Lloyd, G. E., & Mainprice, D., 2014. Fabric transitions in quartz via viscoplastic self-consistent modeling part I: Axial compression and simple shear under constant strain. Tectonophysics 636, 52-69.

O'Kane, A., Onasch, C. M., & Farver, J. R., 2007. The role of fluids in low temperature, fault-related deformation of quartz arenite. Journal of Structural Geology 29, 819-836.

Okudaira, T., Takeshita, T., Hara, I., & Ando, J., 1995. A new estimate of the conditions for transition from basal to prism [c] slip in naturally deformed quartz. Tectonophysics 250 (1-3), 31-46.

Oliver, N. H. S., Rawling, T. J., Cartwright, I., & Pearson, P. J., 1994. High temperature fluid-rock interaction and scapolitisation in an extension-related hydrothermal system, Mary Kathleen, Australia. Journal of Petrology 35, 1455-1491.

Onasch C. M., 1990. Microfractures and their role in deformation of a quartz arenite from the central Appalachian foreland. Journal of Structural Geology 12 (7), 883-894.

Orlandini, O. F. & Mahan, K. H., 2020. Rheological evolution of a pseudotachylite-bearing deep crustal shear zone in the western Canadian shield. Journal of Structural Geology 141, 104188

Pagel, M., Barbin, V., Blanc, P., & Ohenstetter, D., 2000. Cathodoluminescence in Geosciences. Springer-Verlag Berlin Heidelberg.

Passchier, C. W. & Trouw, R. A. J., 1998. Microtectonics. Germany: Springer-Verlag Berlin Heidelberg.

Paterson, M., 1989. The interaction of water with quartz and its influence in dislocation flow – an overview. In Shun-ichiro Karato (Ed.), *Rheology of Solids and the Earth* (107-142). Oxford University Press.

Platt, J. P. & Behrmann, J. H., 1986. Structures and fabrics in a crustal-scale shear zone, Betic Cordillera, SE Spain. Journal of Structural Geology 8, 15-33.

Price, R. A. & Mountjoy, E. W., 1970. Geologic structure of the Canadian Rocky Mountains between Bow and Athabasca Rivers: A progress report. Structure of the southern Canadian Cordillera Geological Association of Canada Special Paper 6, 7-25.

Prior, D. J., Mariani, E., & Wheeler, J., 2009. EBSD in the Earth Sciences: Applications, common practice, and challenges. In A.J. Schwartz et al. (Ed.), *Electron Backscatter Diffraction in Materials Science* (345-360). Boston, MA: Springer.

Prior, D., Boyle, A. P., Brenker, F., Cheadle, M. C., Day, A., Lopez., G. Peruzzo, L., Potts, G. J., Reddy, S., Spiess, R., Timms, N. E., Trimby, P., Wheeler, J., & Zetterström, L., 1999. The application of electron backscatter diffraction and orientation contrast imaging in the SEM to textural problems in rocks: American Mineralogist 84, 1741-1759.

Putnis, A. & Austrheim, H., 2010. Fluid-induced processes: metasomatism and metamorphism. Geofluids 10, 254-269.

Rahl, J. M. & Skemer, P., 2016. Microstructural evolution and rheology of quartz in a mid-crustal shear zone. Tectonophysics 680, 129-139.

Rossi, M., Rolland, Y., & Vidal, O., 2007. Evidence for crystal scale fluid infiltration during the Alpine Orogeny. Geophysical Research Abstracts 9, 06620.

Rossi, M., Rolland, Y., Vidal, O., & Cox, S. F., 2005. Geochemical variations and element transfer during shear-zone development and related episyenites at middle crust depths: insights from the Mont Blanc granite (French-Italian Alps). In Bruhn D, Burlini L. (Ed.), *High-Strain Zones: Structure and Physical Properties*. Geological Society, London, Special Publications 245, 373-396.

Royse, F. C., Warner, M. A., & Reese, D. L., 1975. Thrust belt of Wyoming, Idaho, and northern Utah: Structural geometry and related stratigraphic problems. In Deep drilling frontiers of the central Rocky Mountains: Rocky Mountain Association of Geologists Guidebook. 41–54.

Royse, F. Jr., 1993. An overview of the geologic structure of the thrust belt in Wyoming, northern Utah, and eastern Idaho. In A. W. Snoke, J. R. Steidtmann, & S. M. Roberts (Ed.), *Geology of Wyoming: Geological Survey of Wyoming Memoir No. 5* (272–311). Laramie, WY: Wyoming Geological Survey.

Rutter, E. H., 1983. Pressure solution in nature, theory and experiment. Journal of the Geological Society 140 (5), 725-740.

Satsukawa, T., Ildefonse, B., Mainprice, D., Morales, L. F. G., Michibayashi, K., & Barou, F., 2013. A database of plagioclase crystal preferred orientations (CPO) and microstructures – implications for CPO origin, strength, symmetry and seismic anisotropy in gabbroic rocks. Solid Earth 4, 511-542.

Schaeben, H., 1999. The de la Vallée Poussin standard orientation density function. Textures and Microstructures 33, 365-373.

Schmid, S. M. & Casey, M., 1986. Complete fabric analysis of some commonly observed quartz c-axis patterns. In Hobbs, B. E. & Heard, H. C. (Ed.), Mineral and rock deformation: laboratory studies – the Paterson volume. American Geophysical Union, 246-261.

Sibson, R. H., 1975. Seismic pumping – a hydrothermal fluid transport mechanism. Journal of the Geological Society 131 (6), 653-659.

Sibson, R. H., 1981. Controls on low-stress hydro-fracture dilatancy in thrust, wrench and normal fault terrains. Nature 289, 665-667.

Sibson, R. H., 1983. Continental fault structure and the shallow earthquake source. Journal of the Geological Society 140 (5), 741-767.

Sibson, R. H., 1984. Roughness at the base of the seismogenic zone: Contributing factors. Journal of Geophysical Research Solid Earth 89 (B7), 5791-5799.

Singleton, J. S., Rahl, J. M., & Befus, K. S., 2020. Rheology of a coaxial shear zone in the Virginia Blue Ridge: Wet quartzite dislocation creep at ~250-280 °C. Journal of Structural Geology 140, 104109

Skemer, P., Kayatama, I., Jian, Z., & Karato, S., 2005. The misorientation index: development of a new method for calculating the strength of lattice-preferred orientation. Tectonophysics 411(1), 157-167.

Solum, J. G. & van der Pluijm, B. A., 2007. Reconstructing the Snake River-Hoback River Canyon section of the Wyoming thrust belt through direct dating of clay-rich fault rocks. In Sears, J. W., Harms, T. A., Evenchick, C. A. (Ed.), Whence the mountains? Inquiries into the evolution of orogenic systems, a volume in honor of Raymond A. Price. Geological Society of America Special Paper 443, 183-196.

Starnes, J. K., Long, S. P., Gordon, S. M., Zhang, J., & Soignard, E., 2020. Using quartz fabric intensity parameters to delineate strain patterns across the Himalayan Main Central thrust. Journal of Structural Geology 131, 103941

Steward, M., Holdsworth, R. E., & Strachan, R. A., 2000. Deformation processes and weakening mechanisms within the frictional-viscous transition zone of major crustal-scale faults: insights from the Great Glen Fault Zone, Scotland. Journal of Structural Geology 22 (5), 543-560.

Stipp, M., Stünitz, H., Heilbronner, R., & Schmid, S., 2002. The Eastern Tonale Fault Zone: A 'natural laboratory' for crystal plastic deformation of quartz over a temperature range from 250 to 700°C. Journal of Structural Geology 24 (12), 1861-1884.

Takeshita, T., 1996. Estimate of physical conditions for deformation based on c-axis transitions in naturally deformed quartzite. Journal of the Geological Society of Japan 102 (3), 211-222.

Taylor, G. I., 1938. Plastic strain in metals. Journal Institute of Metals 62, 307–324.

Toy, V., Prior, D., & Norris, R., 2008. Quartz fabrics in the Alpine Fault mylonites: Influence of pre-existing preferred orientations on fabric development during progressive uplift. Journal of Structural Geology 30, 602-621.

Tullis, J. A., Christie, J. M., & Griggs, D. T., 1973. Microstructures and preferred orientations of experimentally deformed quartzites. Geological Society of America Bulletin 84, 297-314.

Van der Pluijm, B. A. & Marshak, S, 2004. Earth Structure. New York, NY: W. W. Norton & Company, Inc.

Wallis, S., 1992. Vorticity analysis in a metachert from the Sanbagawa Belt, SW Japan. Journal of Structural Geology 14(3), 271–280. https://doi.org/10.1016/0191-8141(92)90085-B

Wallis, S., 1995. Vorticity analysis and recognition of ductile extension in the Sanbagawa belt, SW Japan. Journal of Structural Geology 17(8), 1077–1093. https://doi.org/10.1016/0191-8141(95)00005-X

Watanuki, S., Hisada, T., Onoda, J., Hisasue, S., Kanai, T., & Takagi, H., 2020. Deformation conditions and kinematics of fault rocks in the Hatagawa Fault Zone and the Shajigami Shear Zone, Northeast Japan: Insights from calcite and quartz microstructures. Journal of Structural Geology 137, 104046

Wawrzyniec, T., Selverstone, J., & Axen, G., 1999. Correlations between fluid composition and deep-seated structural style in the footwall of the Simplon low-angle normal fault, Switzerland. Geology 8, 715-718.

Wenk, H. R. & Christie, J. M., 1991. Comments on the interpretation of deformation textures in rocks. Journal of Structural Geology 13, 1091-1110.

Wiltschko, D. V. & Dorr, J. A., 1983. Timing of deformation in overthrust belt and foreland of Idaho, Wyoming, and Utah. American Association of Petroleum Geologists Bulletin 67, 1304–1322.

Xypolias, P., 2009. Some new aspects of kinematic vorticity analysis in naturally deformed quartzites. Journal of Structural Geology 31(1), 3–10. https://doi.org/10.1016/j.jsg.2008.09.009

Yonkee W. A., Parry, W. T., & Bruhn, R. L., 2003. Relations between progressive deformation and fluid-rock interaction during shear-zone growth in a basement-cored thrust sheet, Sevier Orogenic Belt, Utah. American Journal of Science 303, 1-59.

Yonkee, A. & Weil, A. B., 2015. Tectonic evolution of the Sevier and Laramide belts within the North American Cordillera orogenic system. Earth-Science Review 150, 531-593.

Yonkee, A., 2005. Strain patterns within part of the Willard thrust sheet, Idaho-Utah-Wyoming thrust belt. Journal of Structural Geology 27(7), 1315–1343. https://doi.org/10.1016/j.jsg.2004.06.014

Yonkee, A., Czeck, D., Nachbor, A., Barszewski, C., Pantone, S., Balgord, E., & Johnson, K., 2013. Strain accumulation and fluid-rock interaction in a naturally deformed diamictite, Willard thrust system, Utah (USA): Implications for crustal rheology and strain softening. Journal of Structural Geology 50, 91-118.

Yonkee, W. A., 1990. Geometry and mechanics of basement and cover deformation, Farmington Canyon Complex, Sevier orogenic belt, Utah. Ph.D. dissertation. University of Utah.

Yonkee, W. A., 1992. Basement-cover relations, Sevier orogenic belt, northern Utah. Geological Society of America Bulletin 104, 280–302.

Yonkee, W. A., 1997. Kinematics and mechanics of the Willard thrust sheet, central part of the Sevier orogenic wedge, north-central Utah. Brigham Young University Studies, 42, 341-354.

Yonkee, W. A., 2005. Strain patterns within part of the Willard thrust sheet, Idaho-Utah-Wyoming thrust belt. Journal of Structural Geology 27, 1315-1343.

Yonkee, W. A., Eleogram, B., Wells, M. L., Stockli, D. F., Kelley, S., & Barber, D. E., 2019. Fault Slip and Exhumation History of the Willard Thrust Sheet, Sevier Fold-Thrust Belt, Utah: Relations to Wedge Propagation, Hinterland Uplift, and Foreland Basin Sedimentation. Tectonics 38(8), 2850–2893. https://doi.org/10.1029/2018tc005444

Yonkee, W. A., Parry, W. T., & Bruhn, R. L., 2003. Relations between progressive deformation and fluid-rock interaction during shear-zone growth in a basement-cored thrust sheet, Sevier orogenic belt, Utah. American Journal of Science 303(1), 1–59. https://doi.org/10.2475/ajs.303.1.1

Yonkee, W. A., Parry, W. T., Bruhn, R. L., & Cashman, P. H., 1989. Thermal models of thrust faulting: constraints from fluid-inclusion observations, Willard thrust sheet, Idaho-Utah-Wyoming thrust belt. Geological Society of America Bulletin 101(2), 304–313. https://doi.org/10.1130/0016-7606(1989)101<0304:TMOTFC>2.3.CO;2

Yonkee, W. A., Willis, G. C., & Doelling, H. H., 2000. Proterozoic and Cambrian sedimentary and low-grade metasedimentary rocks on Antelope Island. The Geology of Antelope Island, Davis County, Utah 37–47.